Addis Ababa University
Department of Earth Sciences
School of Graduate Studies

Remote Sensing Based Actual Evapotranspiration Assessment in the Lake Abaya-Chamo Basin

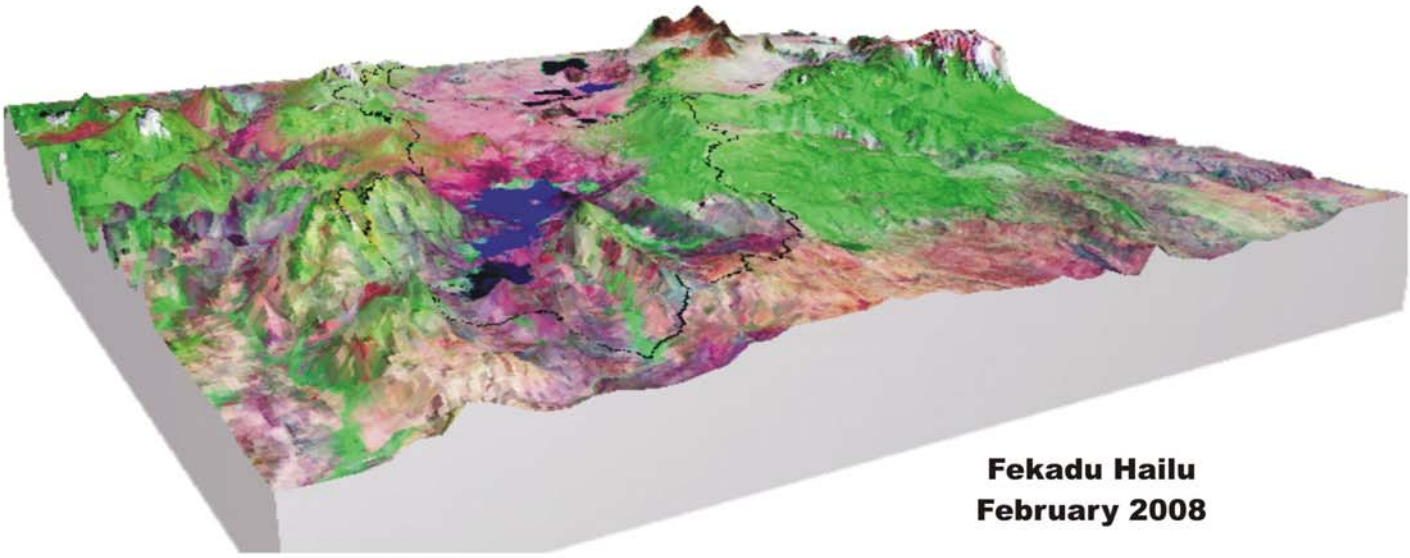

Fekadu Hailu
February 2008

Addis Ababa

REMOTE SENSING BASED ACTUAL EVAPOTRANSPIRATION ASSESSMENT IN THE LAKE ABAYA-CHAMO BASIN

A THESIS SUBMITTED TO THE SCHOOL OF GRADUTE STUDIES ADDIS ABABA UNIVERSITY IN PARTIAL FULFILMENT OF THE REQUIRMENTS FOR THE MASTERS OF SCIENCE DEGREE IN REMOTE SENSING AND GIS

BY

FEKADU HAILU

FEBRUARY 2008

Abstract

The focus of this study is to estimate the daily actual evapotranspiration and assess its spatio-temporal variability in Abaya-Chamo basin, southern section of the Main Ethiopian rift valley using remote sensing techniques. The basin covers an area of 18,600 sq.km and comprises Abaya and Chamo lakes, and number of rivers and streams entering and leaving the lakes. The daily actual evapotranspiration of the basin was estimated and thematically mapped on a pixel-by-pixel basis by applying Surface Energy Balance Algorithm for Land (SEBAL) model on MODIS/Terra images acquired in six days between January and December 2006. SEBAL is an image processing model that uses spatially distributed spectral remote sensing data (visible, near infrared and thermal infrared) to derive radiation, heat and evaporation fluxes. Wind speed and sunshine hour from standard metrological stations were used in modeling. The Evaporative fraction in the land surface exhibited similar regional distribution patterns to the evaporation rate in the basin. In dry seasons, the average evaporative fraction did not exceed 0.4, highlighting the dominance of sensible heat flux across the basin, and the corresponding rise in observed surface temperatures, whereas in wet seasons the EF reached a maximum value of 0.78. The result of this study generally demonstrates that SEBAL could be used to provide information on evaporative loss and moisture condition of the water shade/catchment/basin during modeling processes because image record parameters integrated over a large area. The spatial distribution pattern of actual evapotranspiration is significantly affected by soil moisture content and land use/cover pattern in the basin. In the rift, escarpment and highland, maximum daily evapotranspiration from land surface was recorded in the wet autumn days followed by spring and summer days. In winter days, the rift floor is usually dry and higher evapotranspiration values are limited to swamps/marshy areas. Unlike the rift, relatively high mean daily ETa values in the warm winter days are noted on the highlands. Comparative assessments of the result of this study with the results obtained from river discharge measurements are in good agreement, the difference being less than 10%. But Thornthwaite type soil water balances over estimate ETa by 17% to 37% from mean SEBAL results. This may be due to fracture systems that facilitate water loss in the area in which they do not have well representation in the model. The spatially distributed SEBAL ETa can be used to set water budgets for hydrological modeling, to support water planning, to estimate aquifer depletion and to support ground water modeling. These can be most promising study area in the basin in the future. The integration of remote sensing techniques and distributed hydrological modeling can produce better results.

Key words: actual evapotranspiration, lake Abaya-Chamo, MODIS/Terra, SEBAL

Acknowledgement

First of all, I would like to express my sincere gratitude to the Geological Surveys of Ethiopia for the sponsorship and support I obtained.

I am greatly indebted to my advisor Dr. Dagnachew Legesse for his guidance and valuable advice throughout my study period and during this research work. I highly appreciate his constructive criticism, kindness to allow me to use his personal research materials which contribute much to accomplish this work. My sincere thanks also goes to Dr. Balemwal Atenafu for his unreserved cooperation to carry out the study.

I am very thankful for Mawari project and the France Ministry of foreign affaires for allowing and financing me to take course on geospatial data processing, interpretation and modeling applied to integrated water resource management in eastern Africa, held in Kenya, Nairobi. I have benefited from the course.

I am grateful to all members of the Department of Regional Geology and Geochemistry as well as Department of Geoinformation for their support and assistance. I would like to thank Dr. Bedru Hussen for his encouragement, advice and comments throughout this study. My thanks goes to Ato Solomon Gera and Dr. Hailemeskel Aweke for allowing me to use computer and related facilities.

Thanks are due to Solomme Mekonnen for her support and kindness in downloading and bringing me satellite imageries.

Special thanks are due to Seifu Fessehasion for his valuable suggestion and comments.

I would like to express my thanks to My friends: Aweke Negusse, Assaye Woldu, Daniel Chekol, Daniel Haile, Daniel seifu, Endasshaw Hailu, Fekremariam Taddesse, Harun Ressied, Henoke Tekola, Girma Addisu, Gutema Megerssa, Sisaye Lebasse, Tewodross, and Tesfaye Hadigu for their encouragement and concern throughout my study. They have provided me with invaluable support.

Finally, I would like to express my sincere appreciation for my mother Aberash Yeheis and father Masseresh Tekeleyohannes for their devoted encouragement, help and love during the course of my study and this research. My appreciation also goes to my sisters: Mulu, Yeshi, Amakel and Alem, and brother Melaku. Consistence love and support from them contributed significantly to complete my work.

Table of Content

LIST OF FIGURES

LIST OF TABLES

LIST OF APPENDIX

1 Introduction

1.1 Back ground

The Ethiopian Rift system is the most impressive tectonic feature in East Africa. Its central part, commonly known as the Main Ethiopian Rift (MER), constitutes chains of lakes with complex hydrological and hydro-geological setting (Ayenew T., 1998, Dagnachew et al., 2003). These lakes are of extensive socio-economic and ecological importance.

The Abaya-chamo basin is a major graben in southern part of the Main Ethiopian Rift. It consists of Lake Abaya and Lake Chamo separated by approximately 1km wide forestland, with rivers and streams system flowing to the lakes.

The lakes and feeder rivers are being used for different purposes including agricultural, industrial and recreational. Their catchment characteristics are influenced by human and natural processes both at local and regional scale. Changes in catchment characteristics are mainly induced by urbanization, deforestation, intensive farming, and overgrazing. Moreover, the demand of water continually increases due to faster rate of population growth, along with changes in land use/cover pattern and improper water resource utilization in the region. Planning of proper and efficient long term watershed management in the region requires understanding and knowledge based modeling of hydrological processes. Water resource management requires basic understanding of the spatial and temporal variability of hydrological parameters and quantification of hydrologic cycle components. This includes knowledge of runoff, infiltration into the ground, evaporation and transpiration to the atmosphere etc, and related processes regulating both local and regional hydrologic cycle and climate.

Evapotranspiration is a key process in hydrologic cycle and is important in water resource studies. It is a major component of earth's atmospheric system that affects the yield of river basins, capacity of natural and artificial reservoirs, and yield of ground water. Its significance becomes immense in arid and semi arid regions where precipitation to evaporation ratio is low. Owing to this, understanding and quantifying the spatial and temporal properties evapotranspiration is crucial to formulate and implement feasible water resource management and watershed conservation practices.

There are three different approaches for quantifying evapotranspiration; viz up-scaling from metrological stations, hydrological modeling and remote sensing studies. The application of remote sensing to evapotranspiration estimation is not something new and is an expanding research field to understand the role of evapotranspiration in environmental processes (Example, Jensen et al., 1990, Beljaars and Viterbo, 1994, Wang et al., 1995, Kustas and Norman, 1996, Jiang and Islam, 2001; Tian et al., 2004; Batra et al., 2006; Jin and Liang, 2006). The successful developments of high spatial and spectral resolution sensors provide new opportunities for remote observation of evaporative loss from the ground.

This study presents remote sensing approach for estimating evapotranspiration in the Lake Abaya-Chamo basin. It attempts to give new insight into the assessment of spatio-temporal variability in relation to catchment characteristics. The result is believed to be important for water balance studies and water resource management that is of great value for sustainable water use in the area.

1.2 Objective

The main objectives of this study is to evaluate the spatial pattern of the actual evapotranspiration in the lake Abaya-Chamo basin through a combination of remote sensing information and metrological observation, as described below.

1. Estimation of actual evapotranspiration through the application of the surface energy balance algorithm for land (SEBAL) method on MODIS images.
2. Assess the spatial distribution pattern and temporal variability of actual evapotranspiration in the study area.

1.3 Geography of the Study Area

1.3.1 Location

The lake Abaya-Chamo basin is located in south central Ethiopia covering parts of Oromia and Southern Nations, Nationalities and Peoples Regional States. The area has irregular boundary inscribed by latitudes 5º19’ and 8º8’ North and longitudes 37º16’ and 38º19’ East (fig.1.1). It covers an area of 18,600 sq.km in the southern part of the rift valley lake basin system, south of Awassa lake and north of Segen river basin.

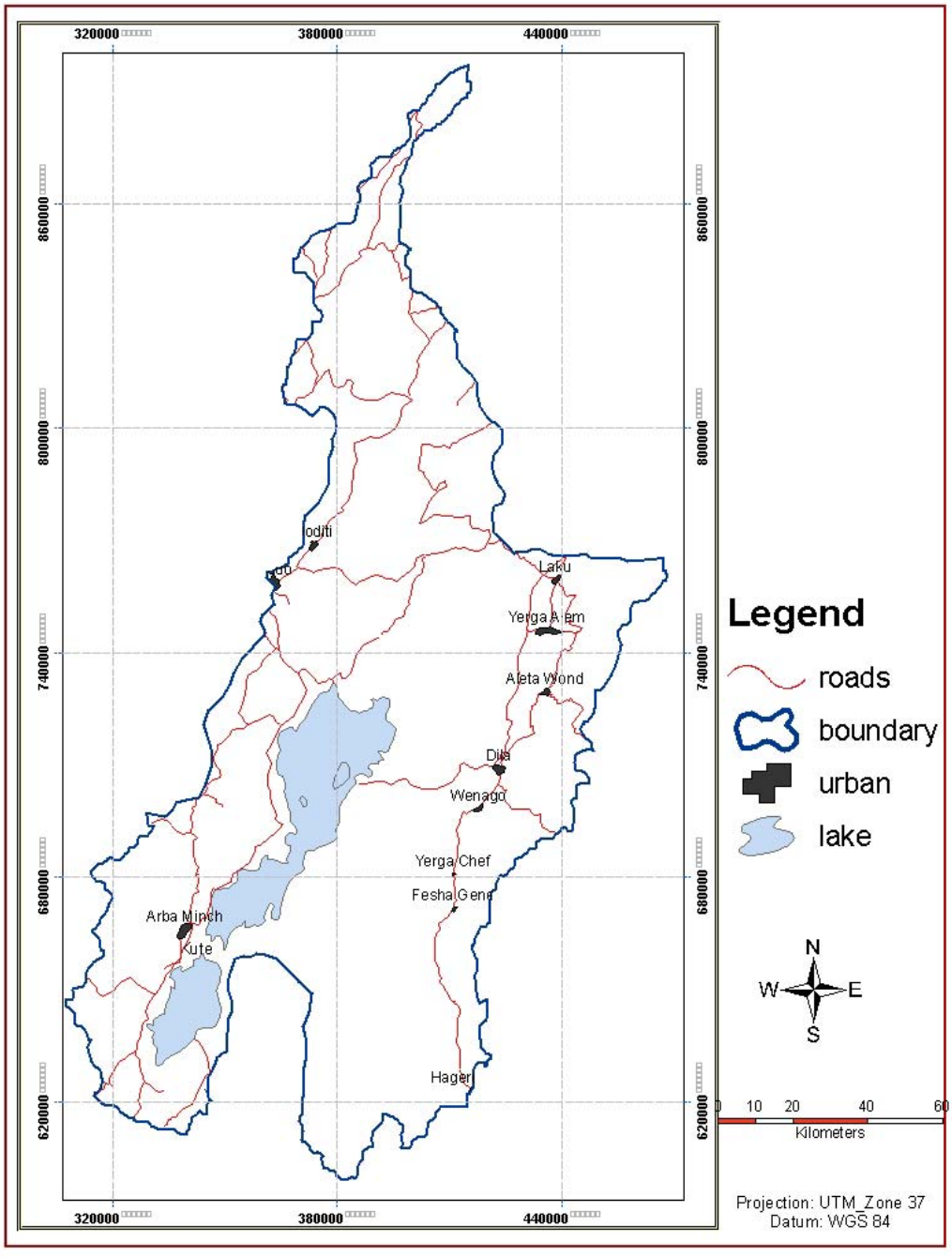

Figure 1.1. Location map of the study area.

Arba Mench, Dila, Yerga Chefe, Welyta and Sodo are among the main cities found in the study area. Arba Mench, located in the western side of Lake Abya, is accessible by the 600 km long road from Addis Ababa.

1.3.2 Physiography

Generally the morphology of the area is typical of continental rifted zones where low lands are surrounded by steep rift scarp and elevated plateaus. The elevation varies from 1087 m.a.s.l in the floor of the rift to 3505 m.a.s.l at the top of plateau (fig.1.2).

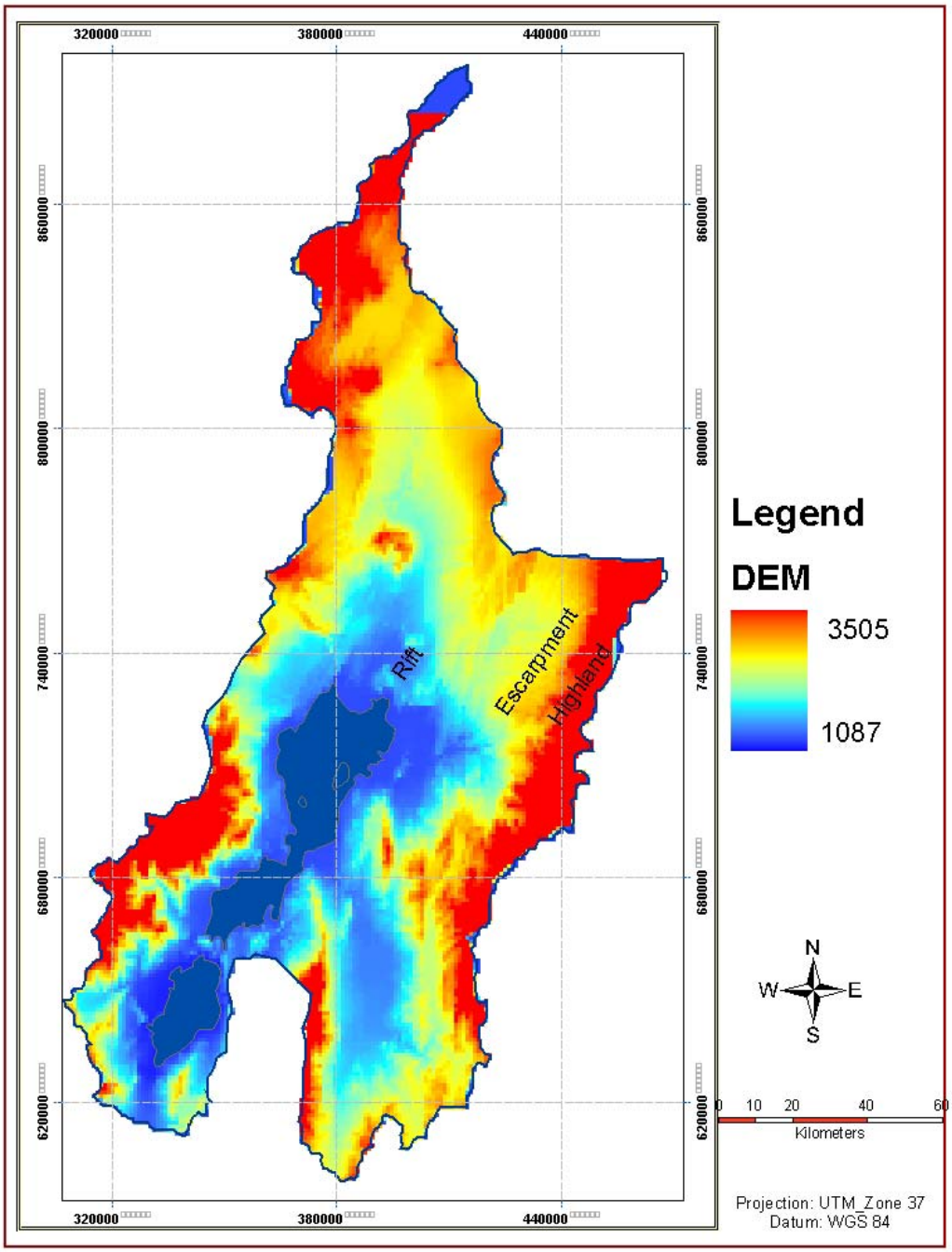

Figure 1.2. DEM and physiographic division of the study area.

There is a marked contrast in topography as one goes from east to west or vice versa in the area. Based on elevation difference the area is divided into three physiographic regions; viz, the rift floor, the escarpment and the plateau (fig 1.2).

The rift floor forms about 70% of the basin and occupies the low-lying part of study area at an altitude between 1087 m.a.s.l and 2800 m.a.s.l. It comprises the two lakes (Abaya and Chamo), which are the center of this basin system and is decorated by volcanic hills and ridges. This prominent lowland passes into steep scarps in the east and west.

The escarpments are found on both sides of the rift floor and constitute about 25% of the study basin. This physiographic feature comprises series of steeply sloping ridges and valley that mark fault scarp or trace, running north west-south east. They are generally rocky and gullied. Altitude varies from 1300 m.a.s.l to about 3000 m.a.s.l.

The plateau is found on both sides of the rift floor occupying the high altitude (2300-3400m). It forms relatively flat topography made of volcanic rocks.

1.3.3 Drainage

The basin comprises mainly Lake Abaya and Lake Chamo covering a total area of 1500 sq. km (EMA, 1984) and total volume of $18.6*10^9$ cb.meter fresh water (Selishi, 2001). Altogether, the lake Abaya-Chamo drainage system covers a watershed of approximately 18, 600 sq.km. There are many tributary drainage networks carrying runoff to and overflow away from these lakes (fig.1.3). The rivers start from the highlands, flow south, southeast, west and southwest and cross the escarpment into alluvial plain and seasonally flooded areas (swamp). Finally, the rivers cross a flat delta, terminating at the lakes. Lake Abaya is drained mainly by Bilate, Gelana, Gidabo, Hara and Bose rivers originating from the surrounding plateaus. Occasional surface out flow from Abaya is often carried by Kulfo river feeding the southern Lake Chamo. Lake Chamo also receives surface water from Sile, Argoba, Wezeh and Sego rivers originating from the western and northern part of the basin. Morphometric characteristics of the lakes and drainage description of the tributary rivers are given in table 1.1.

Table 1.1. Morphometric characteristics of lakes. (Source: Seleshi 2001)

Parameter	Lake	
	Abaya	Chamo
Altitude (m^2)	1169	1110
Basin Area (km^2)	16342	18575
Maximum shore to shore length (km)	79.2	33.5
Mean depth (m)	8.61	10.2
Maximum depth (m)	24.5	14.2
Volume (m^2)	9.82×10^9	3.24×10^9
Lake area (km^2)	1140	317

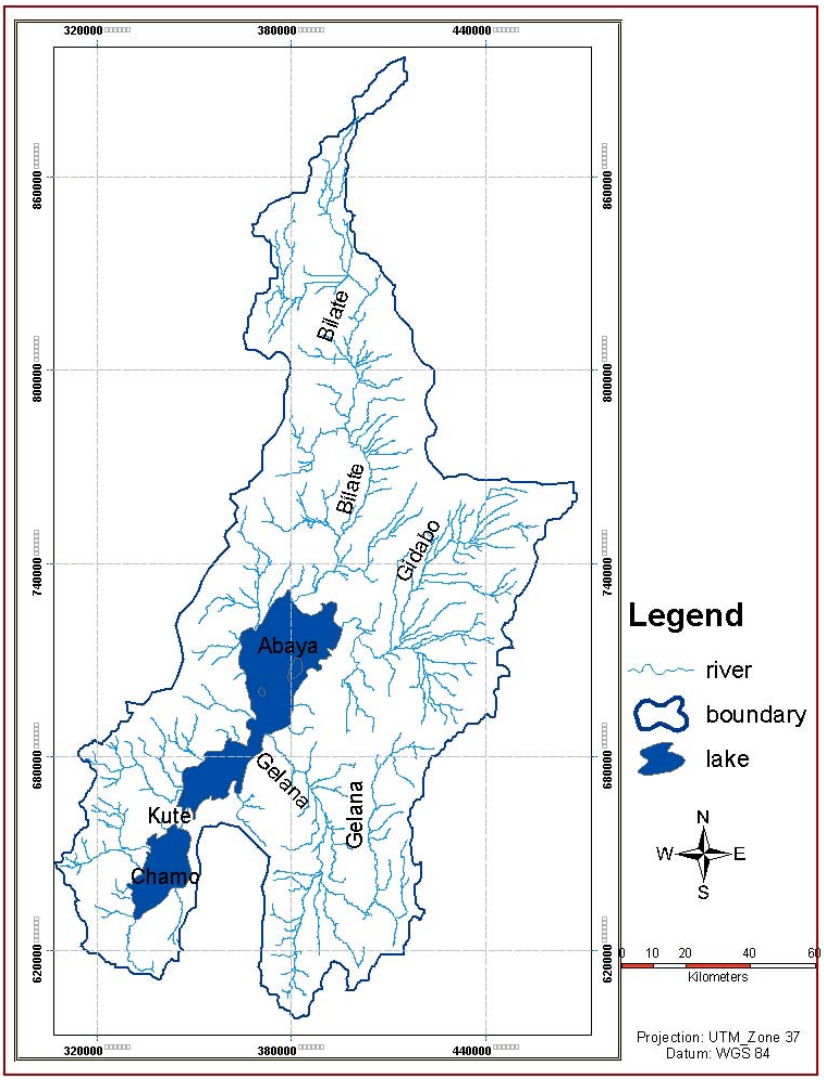

Figure 1.3. Drainage map of the study area.

1.3.4 Climate

Due to contrasts in elevation a semi arid to arid and humid to semi humid climate prevails in the area. The climate in the region is controlled by the convergence of dry northeasterly winds and humid southeasterly or southwesterly winds giving rise to movement of equatorial pressure (Admassu, 1998). Attributed to this the area shows two distinct climatic and rainfall patterns approximately north and south of 6º30' latitude. Marked contrast in altitude (from 3505m to 1087m.a.s.l) and the orographic influence also affects the climatic condition and rainfall pattern of the basin (Selehi, 2001).

From October to February, the prevailing north east wind produces the dry sunny season with low relative humidity. From March to October, south east wind from Indian Ocean brings humidity to the region, which increases south of 6º30' north latitude. The area receives rain in two seasons i.e. from March to June and between September and October (fig. 1.4). A relatively dry season from July to August separate the rainy season in the region. But the proper dry season occurs between November and February. The climatic and rainfall pattern north of 6º30'latitude slightly differs from the above. In the northern part of the area, rain fall occurs in two seasons, i.e from July to September, and March to May. From October to February the area is dry. The mean annual rainfall varies from 550mm, around the lake (elevation 1087m.a.s.l) on the center of the rift floor, to around 1400 mm on the highlands at elevation above 2500 m.a.s.l.

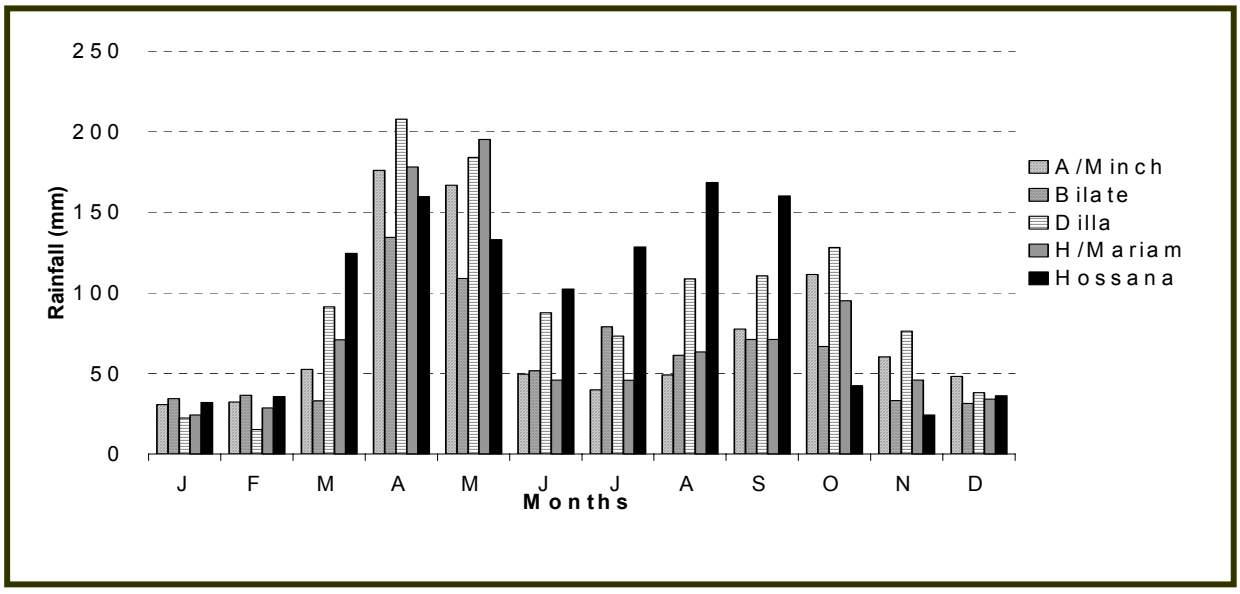

Figure 1.4 Rainfall pattern of the area.

The mean annual temperature varies between 15ºC and 25ºC, attaining a maximum shading temperature of 35 ºC during the hottest months between January and March (fig 1.5a). The minimum absolute temperature does not drop below 15ºC throughout the year. Altitude is the major factor influencing temperature (fig 1.5b). Temperature ranges from 21ºC-23ºC around lakes at an altitude in the range of 1200-1300 m, 16ºC-18ºC at 2000 m elevation and 13ºC-15ºC at about 2500 m altitude above sea level. The drop in temperature is about 0.7 ºC per 100 meter difference in altitude. The mean monthly minimum temperature is low from October to January and high from February to April (fig 1.5a). The daily temperature variation is high, ranging from 14 ºC in June to about 18 ºC in December at Arba Minch.

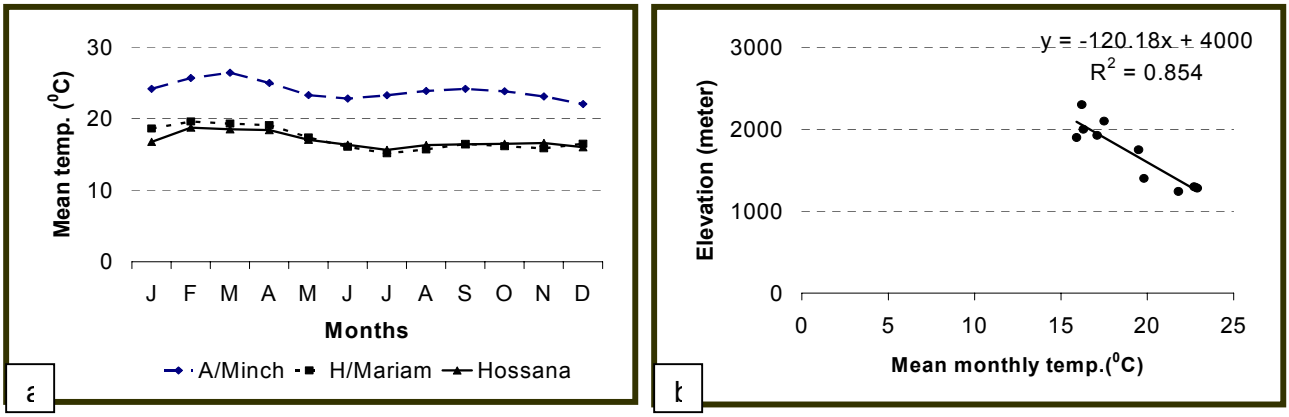

Figure 1.5 a) Mean monthly temperature b) correlation between temperature and altitude.

In the low-lying area, monthly total pan evaporation increases from about 111 mm in October to as much as 372 mm in March (fig 1.6a), whereas stations in highland areas record total monthly pan evaporation ranging from 59.1 mm in Augest to 183 mm in February. Relative humidity in the rift ranges from 70% in July to 48% in February, while in the highlands it ranges from 79% in September to about 58% in February (fig 1.6b).

Mean monthly sunshine hour ranges from 4.3 in July to 9.8 in March (fig 1.7a). There is considerable variation in wind speed between the rift and the highlands. Wind speed ranges from 0.5 m/s in November to about 0.9 m/s in March and August in the rift, while it ranges from 0.5 m/s in October to more than 1.4 in February (fig 1.7b).

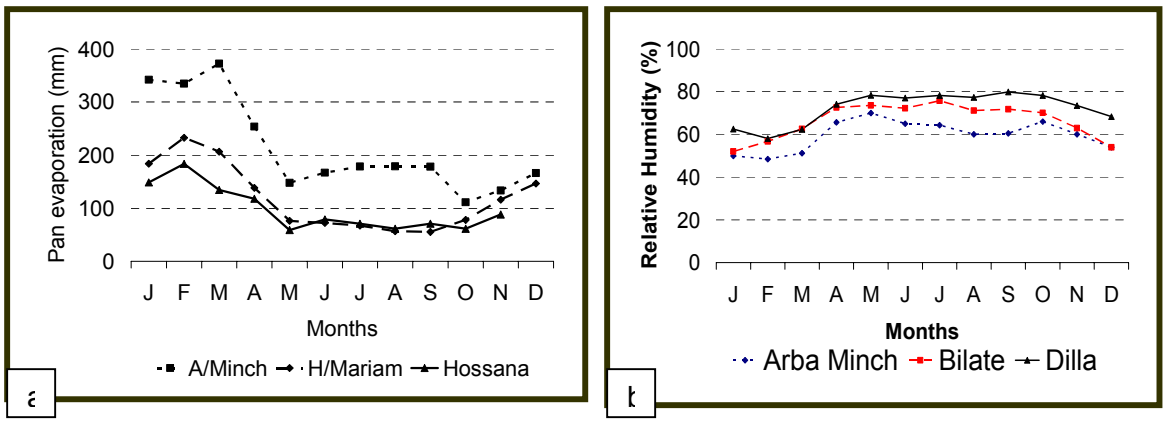

Figure 1.6 a) pan evaporation b) relative humidity in the study area.

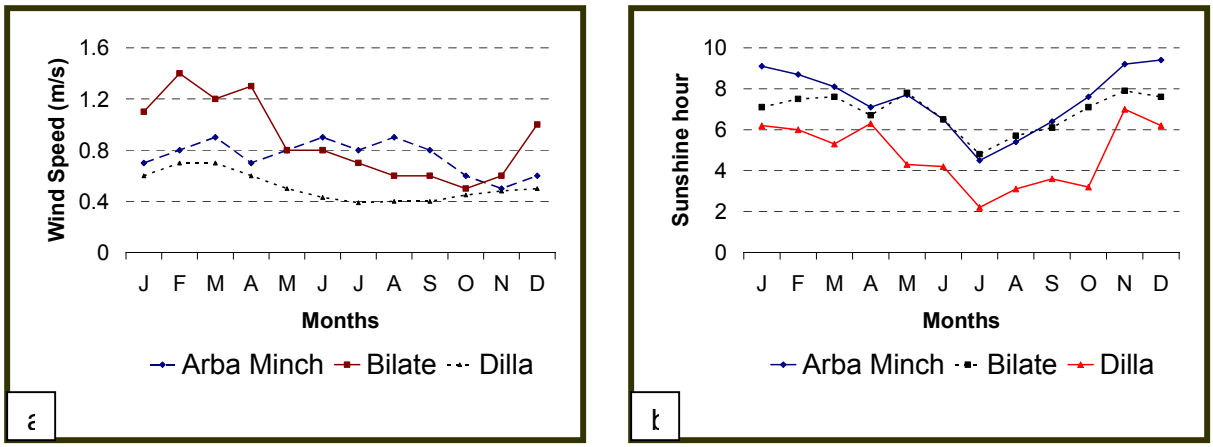

Figure 1.7 a) wind speed b) sunshine hour in the study area.

1.3.5 Land Use and Cover

Land use/cover affects water circulation and is an important factor for analyzing evapotranspiration in a certain area. Due to population growth and urbanization, land cover type continually changes. Since land use/cover is sensitive to interference, it is difficult to obtain accurate land use/cover grid. The digital Soil map of East Africa (SEA) prepared by FAO (1996) provides a detailed database of land use/cover types in the region, from which some reference was made. Besides the land use/cover produced by Ministry of water resource (HALCROW, 1992) has been another source of data for delineating different land use/cover pertained in this study.

Based on the previous available data and interpretation of MODIS image acquired in 2006, seven major land use/cover classes were identified in this study (fig. 1.8). These are: agriculture, bush land, grass land, agriculture with forest, mixed agriculture-grass-wood land, bush and agriculture land and water body, and their extent is given in Table 1.2.

Table 1.2 Land use/cover classes derived from MODIS

Land use/cover class	Area sq.km	Area %
Agr, grass &wood	5213	28.2
Bush, shrub land	1827	9.90
Agr. With forest	3121	16.9
Bush &grass land	2213	11.8
Grassland	1300	7.00
Agriculture	2140	11.6
Bush & agri	1188	6.40
Water body	1498	8.00

The natural vegetation in the study area consists of thorny shrubs, wooded savanna, bush, bush grassland, grasses and mountain forest. Their distribution and variability is a function of ecological zonation and altitude. Thorn Shrubs and bushes such as *Acacia* are commonly found in arid and semi arid climatic zone around the rift floor. Forest grows distinctly in the semi humid and humid environment.

1.3.6 Soil

According to soil database of FAO, 1997 (The digital Soil And Database of East Africa) and based on FAO/UNESCO system of soil classification, there are six soil types in the study area (App .1.1): Luvisols, Vertisols, cambisols, fluvisols, nitisols, leptosols,.

The dominant soil types in the study area are described as follows:

Andosols are easy to cultivate and have good rootability and water storage properties.
Luvisols are soils that have a higher clay content in the subsoil than in the topsoil as a result of processes leading to an argic subsoil horizon. Luvisols have high-activity clays throughout the argic horizon and a high base saturation at certain depths.

Vertisols are heavy clay soils with a high proportion of swelling clays. These soils form deep wide cracks from the surface downward when they dry out, which happens in most of the years. The heavy soil texture and domination of expanding clay minerals result in a narrow soil moisture range between moisture stress and water excess. Excess water in the rainy season stored on Vertisols with very slow infiltration rates.

1.3.7 Culture

A number of ethnic groups inhibit the area, namely Wolyta, Gamo, Gidole, Konso, Gedeo and Gudje. Their mode of life is variable, ranging from semi-nomadic to peasants producing cash crop. Each of these ethnic groups speaks their own language. Besides these, there are considerable numbers of people recently settled in the area under a resettlement program. The main food crops grown are enset (false banana), cereals (maize, sorghum, barley and teff), tubers (potato, sweet potato, yams, cocoya), pulses (haricot beans, hoarse beans, lentils, peas), vegetables (cabbage, onion) and sugar cane. Coffee is often grown in association with enset. As discussed in HALCROW (1992) both state and peasant owned farming are practiced. The basic means of subsistence of the semi nomadic Gudje Oromo tribes is the stock they raise which includes; cattle, goat, sheep and camel.

Figure 1.8 Different land use/cover type in the study area.

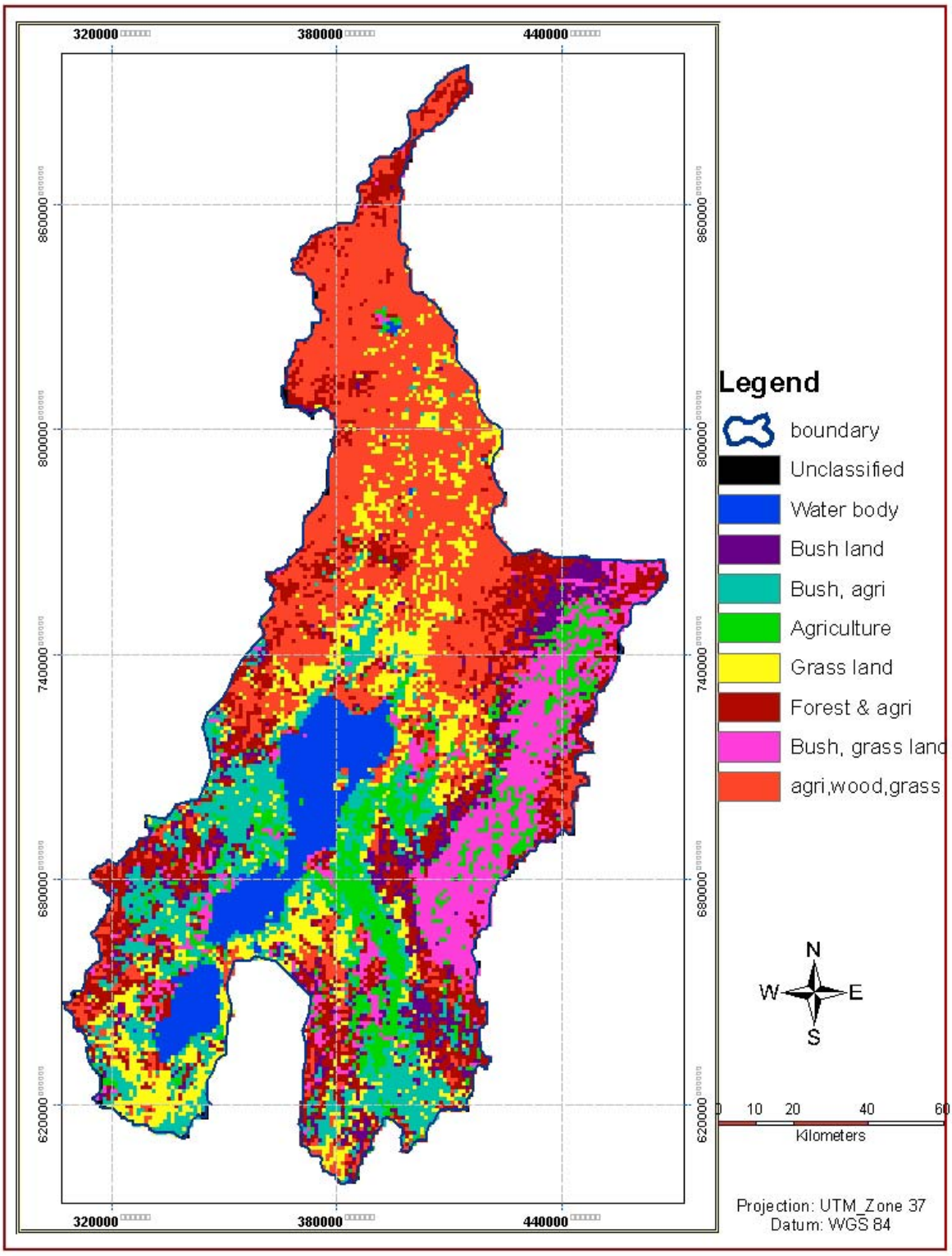

Figure 1.9 Land use/cover map of the study area.

1.4 Previous Study

Much of Ethiopia's territory is not hydrologically and hydro-geologically well studied. Previous and on going water resource studies focus on trans-boarder rivers aimed at the understanding of water resource, and its potential assessment to design water development projects.

Among 11 big drainage basins in Ethiopia the rift valley basin has been studied since1970's (Makin et al., 1975, Gibb, A., 1987, Halcrow., 1992, Ayenew T., 1998, Dagnachew et al., 2003). The rift valley lake basin system contains about 12 chains of lakes found within spectacular NE-SW, running approximately 20 (min) to 120 km wide extensional rift (fault) zone. Lake Abaya and Chamo, which are located in the southern sector of the rift system, are among these.

Study in the lake Abaya-Chamo basin started in the early forties. Morandini (cited in Seleshi, 2001) sketched earlier approximate depth contour of lake Abaya in 1941. More detailed and integrated hydrological, hydro-geological and metrological studies have also been conducted by various workers for different purposes. The contribution made by Gibb, A (1987), HALCROW (1992), EVDS-UNDP (1992), Elizabet K. et al (1994), Geremew (1994), Hailey Tsige (1995), Dibs-Laban, J (1998), Admassu (1998), Seleshi (2001) and Schueet and Wenclawiak (2004) provide useful insights to understand the complex hydrological and hydrogrological system of the region.

Schueet and Wenclawiak (2004) have studied siltation and contamination of lake Abaya. They indicate climatic variability, dramatic population growth, changes in land ownership, clearing of forest and bush land as well as change in cultivation manner which caused dramatical increase in sediment yield of the Lake Abaya tributaries, thus, influencing Lake bathemetry.

2 Literature Review

2.1 Theoretical background

Water molecules continually exchange between liquid and vapor phases by a process known as evaporation. In this process liquid water is converted into water vapor and removed from evaporating surface (Shaw 1994, Chow 1998). Water can be evaporated from a variety of surface such as water body (lakes), bare soil or soil covered with vegetation, agricultural field, forest and impervious surface. From water bodies (lakes and rivers) evaporation takes place continually and hence there is continual loss of water. Evaporation is a function of climate factors. When water evaporates from vegetation through leaves, it is called transpiration. This process also includes evaporation of rain water intercepted by vegetation. Vegetations continually pump water from the ground into the atmosphere and the rate varies depending on the type of vegetation. Transpiration is related to draws of water stored in soil pores at depth and is a function of land cover and vegetation. Practically, it is hard to differentiate between evaporation and transpiration when the ground is covered by dense vegetation because these processes occur simultaneously. Because of this, these two processes are collectively termed as evapotranspiration.

The change of state of the molecules of water from liquid to vapor requires energy input, called latent heat of vaporization. Solar radiation and the ambient temperature of the air provide this energy. The difference between vapor pressure at the evaporative surface and surrounding atmosphere is the main cause of vapor removal from evaporative surface. When water passes from liquid to vapor state, it absorbs about 590 calories of heat per gram of water from evaporative surface. Some factors affecting evapotranspiration are as follows (Maidment, 2002, 1993):

1) Solar radiation: the energy input responsible for conversion of water into vapor.
2) Wind: important factor controlling evapotranspiration which governs ability to transport vapor away from the surface.
3) Relative humidity (vapor pressure gradient): determines the ability of the air to absorb water. As humidity rises, its ability to absorb water decreases and rate of evaporation slows.
4) Temperature: evaporation proceeds if the ambient air and ground temperature is high.
5) Soil water content and its ability to conduct water;
6) Cultivation practice and extent of vegetation;

7) Environmental aspect and management;

Evapotranspiration can be actual or potential. Potential evapotranspiration refers to the rate at which evaporation occurs from an area completely and uniformly covered with short green crops containing surplus water. It depends on several surface characteristics: surface albedo which determines the net radiation, maximum leaf conductance, atmospheric conductance and presence of intercepted water as defined by Penman (Shaw 1994). Actual evapotranspiration is the loss of water dependent upon available soil moisture or water.

2.2 Estimating evapotranspiration

Evapotranspiration is an important parameter in water resource studies. Its accurate estimation is vital, because the difference between precipitation and evaporation determines aquifer recharge and water use. It is difficult, however, to accurately quantify evapotranspiration directly. There are multiple methods for estimating evapotranspiration for a drainage basin. The most widely used methods can be grouped into three categories viz, field in-situ measurement, modeling approach and remote sensing technique (Bastiaanssen et al., 2005, Alley.W.M., 1984). The methodological approaches are briefly discussed below.

In-situ measurement: most field measurements of evapotranspiration are indirect involving measuring of other water and energy balance components mostly using Lysimeter, Bowen ratio and eddy correlation methods. However, these techniques are subjected to series of errors such as measurement error, when the process is not fully understood or when too many simplifications and approximations are made and errors related to spatial and temporal variability over a landscape (Twine et al. 2000, Allen et al. 1991 as cited in Basitiaanssen 2005). For example, performance of lysimeter strongly depends on the precision of instrument installation and on the representation of the surrounding vegetation and soil moisture content. Most direct measurements of water and energy balance components often provide only point/localized phenomena and do not integrate spatial and temporal variability.

.

Modeling approach: Hydrological models are simplification and abstraction of known or assumed functions expressing the various components of a hydrologic cycle. They are a powerful tool for water resources studies. Spatially distributed hydrological models such as SWAT (Arnold et al., 1998) have been used to simulate hydrological parameters including runoff, interception, evapotranspiration, infiltration and climate change, over a drainage basin (Neilson,

1995; Najjar, 1999 as described in Mendoza et al., 2002). Therefore, evapotranspiration can be estimated and its relation can be assessed with respect to other relevant variables such as precipitation, infiltration and soil moisture.

Remote sensing technique: Remote sensing is, as defined and discussed by Sabins (1987), and Lillesand and Kiefer (1994), " the science and art of obtaining information about an object, area or phenomena through the analysis of data acquired by sensor that is not in direct contact with the target of investigation". Remote sensing is used for monitoring hydrological state variables and as a basis for parameter estimation in hydrological models (e.g., Schultz and Engman, 2000). Its main advantage lies on its ability to provide spatial and temporal data instead of point data. Besides, remote sensing has the following three levels of use in water resource studies (Salomonson, 1983 cited in Mendoza et al., 2002):

1. Identifying area of interest such as water body, alluvial fun,
2. Retrieving land cover data, geological and geo-morphological features through interpretation and classification.
3. Direct estimation of precipitation, evaporation and other hydrological parameters.

2.3 Remote sensing application for evapotranspiration estimation

Remote sensing techniques of evapotranspiration estimation are based on atmospheric and land surface information that can be obtained through spectral analysis of top-of-atmosphere measured radiance. These methodologies vary from statistical or semi-empirical, to physically based estimation and numerical modeling.

Empirical methods involve statistically relating evapotranspiration calculated from metrological stations and spatially distributed NDVI, surface temperature and surface reflectance (Meneti, 1984, Gurney and Hall, 1983). Several researchers have developed empirical linear relationship between evapotranspiration, surface temperature and spectral indices (for example Carlson et al. 1995, Nemani and Running 1989, Friedle and Davis 1994). Numerical modeling is also used to simulate heat and water flow through soil, atmosphere and vegetation (Kustas and Norman, 1995; Basitiannssen et. al., 1998).

3 Material used and Methods applied

3.1 Remote sensing data

The main remote sensing information used in this study is a Moderate-resolution Imaging Spectroradiometer images (MODIS) provided by USGS Earth Observation System (EOS) Data Gateway. Earth Observing System (EOS) Data Gateway website (http://edcimswww.cr.usgs.gov/pub/imswelcome) is an excellent source of free downloadable MODIS data or products. MODIS is a multi-spectral imaging instrument aboard NASA's Terra (EOS AM) and Aqua (EOS PM) satellites. Terra's orbit around the Earth is timed so that it passes from north to south across the equator in the morning, while Aqua passes south to north over the equator in the afternoon. The MODIS instrument operating on both the Terra and Aqua satellites has a swath width of 2,330 km and views the entire surface of the Earth every one to two days. They acquire moderate resolution images in 36 spectral wavelength ranges between 0.405 and 14.385 μm at 250m, 500m, and 1,000m. MODIS spectral and spatial characteristics in visible and thermal bands are shown in App. 3.1.

Six relatively cloud free MODIS data or products (surface reflectance and temperature) in the period between January 2006 and December 2006 were acquired through EOS Data Gateway (App. 3.2). The data downloaded from USGS EOS Data Gateway are 4G level, and fall on MODIS tile coverage defined by 21V vertical and 08H horizontal coordinate (fig. 3.1).

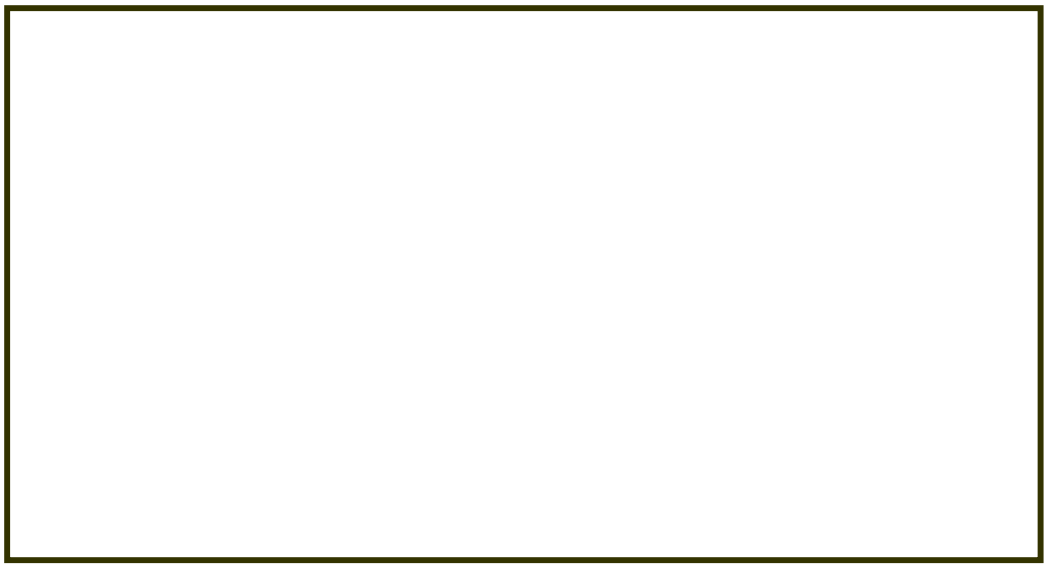

Figure 3.1 MODIS sinusoidal grid

In this projection, the globe is divided into fixed tiles of approximately 10^0 by 10^0 in size. Each tile is assigned a horizontal (H) and vertical (V) coordinate ranging from 0 to 35 and 0 to 17, respectively. The following sections describe the type of MODIS data used.

3.1.1 MODIS product

MODIS data acquired through sensors on board the Terra and Aqua satellites, are transferred to different ground stations and sent to the EOS Data and Operations System (EDOS). After Level 0 processing at EDOS, the Goddard Space Flight Center Earth Sciences Distributed Active Archive Center (GES DAAC) produces the Level 1A, Level 1B, geolocation and cloud mask products. Higher-level MODIS land products are produced by the MODIS Adaptive Processing System (MODAPS).

There are many standard MODIS data products that can be used to study global change. In remote sensing based evapotranspiration estimation, satellite images are used to derive input parameters for energy balance computation such as albedo, surface reflectance, emissivity and vegetation index. These parameters can all be obtained from MODIS standard products of visible and thermal bands i.e surface reflectance and surface temperature/emissivity products. (See App. 3.3 for the standard MODIS land products available.)

Currently available V004 and V005 MODIS Land data products represent provisional and validated data set whose uncertainties are generally well defined over the range of surface condition. In this study surface reflectance and Land Surface Temperature/Emissivity were obtained from EOS data gateway were used.

3.1.2 Surface reflectance products

Among several MODIS surface reflectance products MODIS/Terra Surface Reflectance Daily L2G Global 250m SIN Grid V004 (MOD09A) were utilized to derive surface energy fluxes and evapotranspiration. The MODIS Surface-Reflectance Product (MOD 09A) is derived from the MODIS Level 1B land bands 1-7 (centered at 648 nm, 858 nm, 470 nm, 555 nm, 1240 nm, 1640 nm, and 2130 nm, respectively). Table 3.1 provides characteristics of MOD09. The product is an estimate of the surface spectral reflectance for each band as it would have been measured at the ground if there were no atmospheric effect (absorption and scattering). It goes through corrections for the effects of atmospheric gasses and aerosols.

Table 3.1 Description of MODIS/Terra Surface Reflectance Daily L2G Global 500m SIN Grid V004

SDS	Units	Fill Values	Valid Range	Scale Factor
Band 1- band 7	Reflectance	-28672	-100-16000	10000
Orbit and Coverage	-	15	0-255	-
Number of Observation	-	-1	0-127	-

3.1.3 Land Surface Temperature/Emissivity products

MODIS/Terra Land Surface Temperature/Emissivity Daily L3 Global 1km SIN Grid V004 (MOD11) is one of the products which provide temperature and emissivity values for each pixel. The generalized split-window LST algorithm was applied to retrieve LST for MODIS pixels with known emissivities in bands 31 and 32. View angle information was also included in each LST/E products. The LST/E algorithm uses MODIS data as input such as geo-location, radiance, cloud masking, atmospheric temperature, water vapor, snow and land cover. Full description of MOD11A is shown in Table 3.2.

Table 3.2 Description of MODIS/Terra Land Surface Temperature/Emissivity.

SDS	Units	Fill Values	Valid Range	Scale Factor
Daily daytime 1 km grid-land surface temperature	K	0	7500-65535	0.0200
Quality control for daytime LST and Emissivity	-	0	0-255	-
Time of day time Land-surface temp. observation	Hrs	0	0-240	0.1000
View zenith angle of daytime land-surface temp.	D	255	0-130	1.000
Band 31 emissivity	-	0	1-255	0.0020
Band 32 emissivity	-	0	1-255	0.0020

3.2 Meteorological data

Metrological factors such as temperature, relative humidity, wind speed and solar radiation has a considerable effect on the rate of evaporation. Important meteorological observations required for SEBAL model includes wind speed at 2 m height and sunshine hour data.

Ethiopian Meteorological Agency operates about 14 meteorological stations in lake Abaya-Chamo basin (app.3.4). The stations are randomly distributed and most are only capable of recording temperature and rainfall amounts. The metrological data for this study was mainly from the archives of five principal stations equipped to record sunshine hour, wind speed and humidity. Rainfall and temperature data were also found from second and third class stations. There is no single station with records of radiation in the study area.

Since there is significant elevation difference between the rift and highland sunshine hour and wind speed recorded at Dilla and Hossana stations are used for the elevated upland, where as for the rift these parameters are obtained from the average values recorded in Bilate, Arba Minch and Merab Abaya stations.

In the following section, metrological records important for estimation of evapotranspiration are presented and their significance discussed.

3.2.1 Sunshine hours

Sunshine hour is an important parameter in SEBAL model if data on atmospheric transmissivity and incoming solar radiation measurements are not available. It is also one factor for potential evapotranspiration estimation. The mean daily sunshine hour recorded at five stations during MODIS image acquisition dates are given in table 3.3. Mean monthly sunshine hour are also presented in app. 3.5.

3.2.2 Wind speed

The station at Arba Minch, Bilate, Merab Abaya and Dilla has been measuring wind speed with Anemometer at 2m above the ground. The mean daily wind speed used as input for SEBAL is shown in table 3.3. and mean monthly values are presented in app. 3.6.

3.2.3 Temperature

Air temperature is one of the most important climatological variables that affect rate of evaporation. Mean daily air temperatures over the study area at satellite pass time recorded at 14 meteorological stations are shown in app. 3.7. These data were used to adjust water surface temperature for elevation. Mean monthly air temperatures from these stations were interpolated and used to compute potential evapotranspiration and are given in app. 3.8.

Table 3.3 Mean daily sunshine hour and wind speed during satellite pass time of year 2006.

	Rift		Esp & Highland	
Image aq. date	Sunshine hour	Wind speed	Sunshine hour	Wind speed
Jan. 01	8.4	0.9	8.0	1.1
Feb. 02	9.3	1.1	8.9	1.5
May 01	7.5	0.8	7.6	1.0
Jun. 18	6.5	0.9	6.1	1.2
Oct. 31	7.4	0.5	8.8	1.1
Nov. 30	8.5	0.6	9.5	1.3

Source: Ethiopian Metrological Agency. Sunshine hour in hour and wind speed in m/s.

3.2.4 Relative humidity (RH)

Relative humidity (RH) is one of the most important hydrologic variable that control evaporation and transpiration. Relative humidity was measured three times a day at four stations. The mean values of these measurements were used and the values at different station are given in app. 3.9.

3.2.5 Rainfall

Rainfall data were used for water balance computation. Mean monthly rainfall values obtained from 14 metrological stations were interpolated and are shown in app. 3.10.

3.3 Digital Elevation Model (DEM)

Topography is the most important factor that influences the distribution and flux of water within the basin. The digital representation of topography is called a digital elevation model (DEM). The DEM data used is that freely distributed by USGS which was produced few years ago by Shutter Radar Topographic Mission project (SRTM). The study area represented by Six 1^0 tile DEM data, i.e N05ºE037º, N06ºE37º, N07º037º, N05ºE038º, N06ºE038º and N07ºE038º. The data have been geo-referenced to WGS84 UTM Zone37 and have cell size of 90 meter (3 Arc second resolutions). These six grids were mosaiked to obtain one DEM grid that are used to generate basin boundary and drainage network and subsequent analysis.

3.4 Softwares used

The main software packages used were ERDAS IMAGINE 8.6 and ArcGIS 9.0. All remote sensing processing: image rectification, sub-setting, classification and Modeling were done with ERDAS IMAGINE spatial modular tool which enable to create and run models for image processing and GIS analysis. It is a highly flexible tool which uses Model Maker and the Spatial Modeler Language. The Spatial Modeler Language is a modeling language that is used internally by Model Maker to execute the operations specified in the graphical models that were created. ESRI ArcGIS 9.0: ArcMap with spatial extension, ArcCatalog, ArcMap and ArcToolbox were used for GIS analysis.

Other softwares used were:

- ILWIS 3.3 academic: DEM hydro-processing Module for extracting drainage network and basin delineation.
- Microsoft Office 2003: Ms Word and Ms Excel - for word processing and creating graphs.
- RSI ENVI 4.2 and Global Mapper 6 were also used for some remote sensing processing.
- Corel Graphics suite: Corel Draw 11 and Corel Photo Paint 11 for figure preparation and image editing.

3.5 Method applied

The aim of this investigation is to estimate and analyses the spatial and temporal variation of actual evapotranspiration of the study area using remotely sensed data and corresponding model- Surface Energy Balance Algorithm for Land Surface (SEBAL). The SEBAL model involves long procedures and associated techniques that are indicated in the following section. GIS function allowed integration of the results of SEBAL model, DEM and metrological data and assess spatial variability of actual evapotranspiration in relation to topography and land use /cover. A schematic flow diagram of the methods and material used are shown in Figure 3.2.

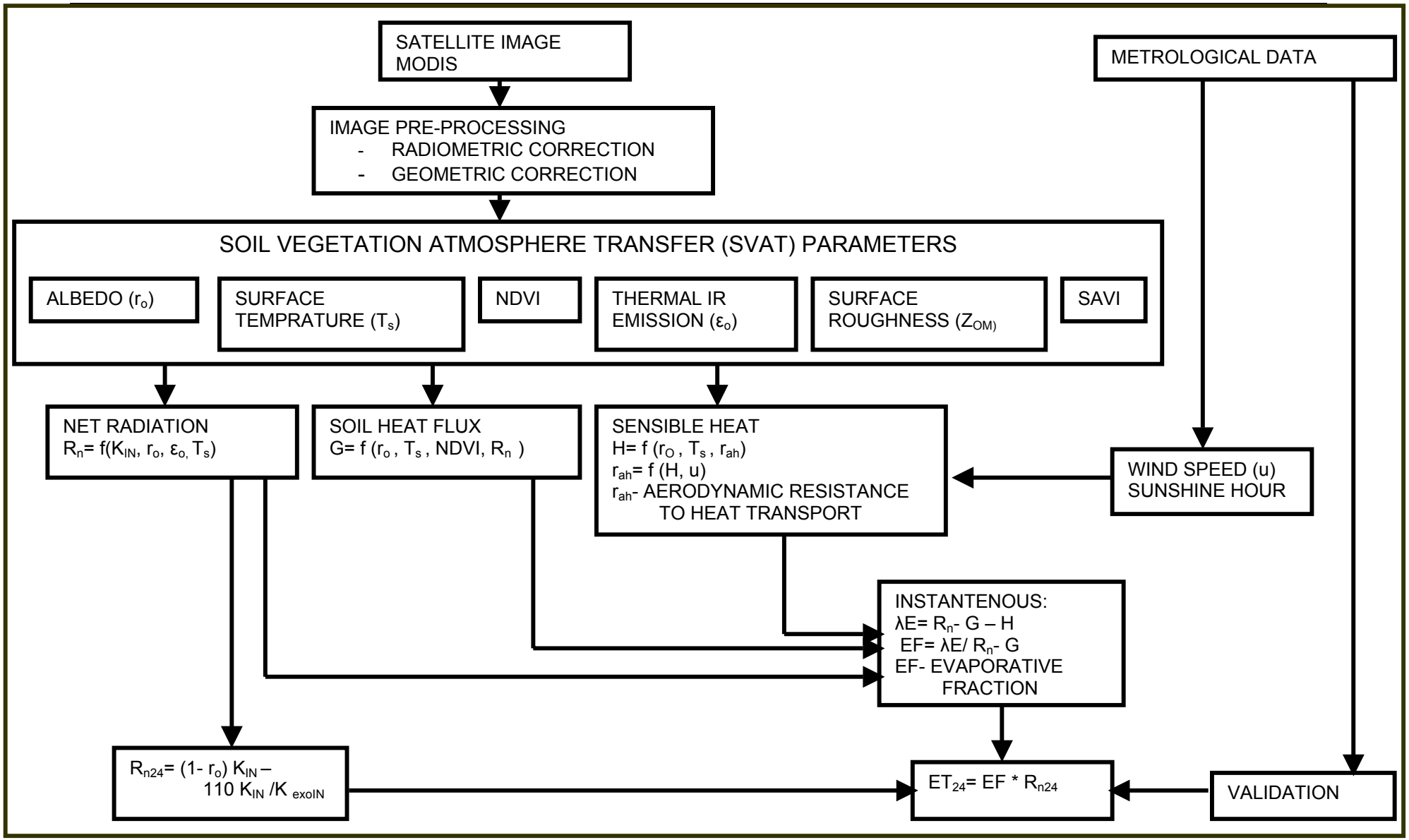

Figure 3.2 Schematic flow diagram of the method and material used.

3.5.1 Model description

SEBAL is a physically based multi-step model which has been designed to calculate the energy partitioning at regional scale with minimum ground data (Bastiaanssen et.al., 1998). It is a relatively new parameterization of surface heat fluxes based on spectral satellite measurements which has been formulated and developed by Bastiaanssen (1995). SEBAL uses surface temperature T_0, hemispherical surface reflectance, r_0 and Normalized Difference Vegetation Index (NDVI), as well as their interrelationships to infer surface fluxes on a pixel-by-pixel basis for a wide spectrum of land types. A conceptual scheme of SEBAL is presented in Fig. 3.3. SEBAL requires spatially distributed, visible, near-infrared and thermal infrared data, which can be taken from satellite imageries.

Major model components describe conversion of remotely sensed emitted and reflected radiances into surface energy balance and wetness indicator. The SEBAL parameterization is an iterative and feedback-based numerical procedure that deduces the radiation, heat and evaporation fluxes. The principle behind SEBAL model is conservation of energy.

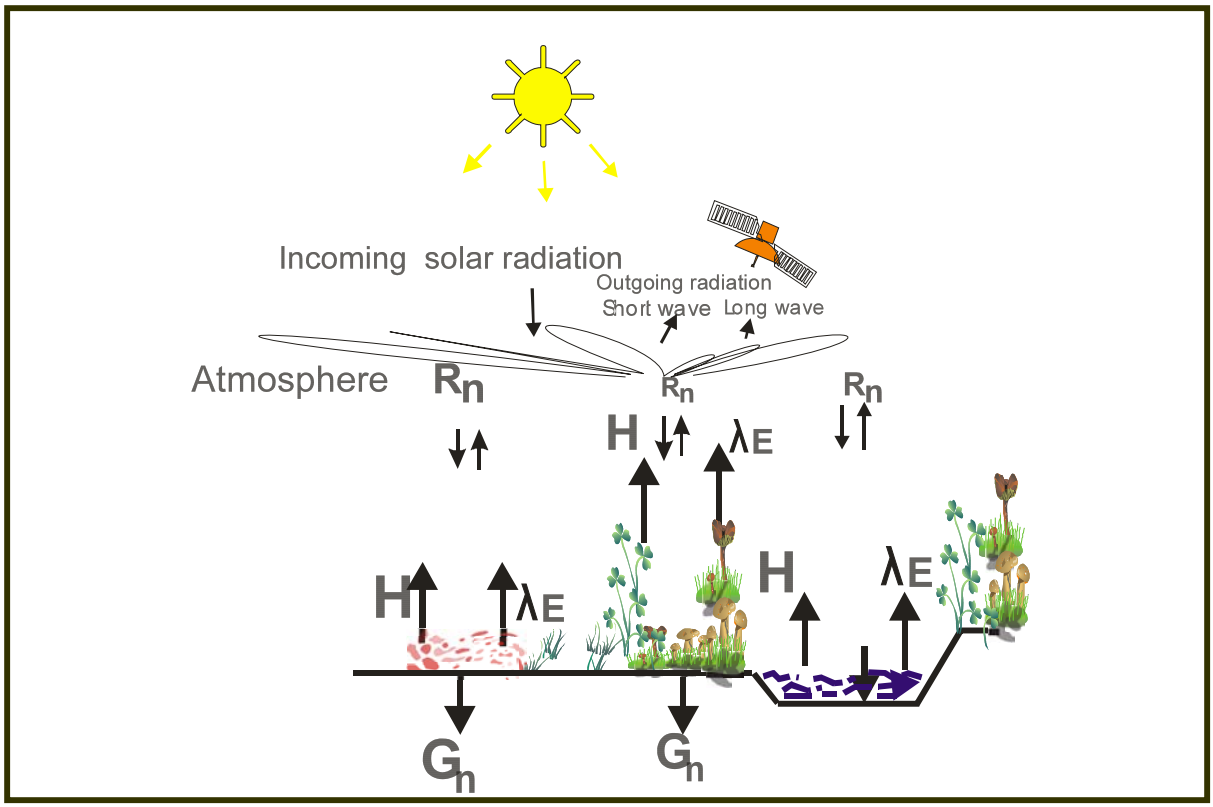

Figure 3.3 Principal components of the SEBAL which converts remotely sensed radiance into the surface energy balance and moisture indicators.

Evaporation process requires relatively large amount of energy, either in the form of sensible heat or radiant energy, and is a consequence of change in energy fluxes between land surface and atmosphere. This is expressed as the energy balance equation:

$$Rn + G + H + \lambda E = 0 \quad (3.1)$$

Where R_n (Wm^{-2}) is net radiation, G (Wm^{-2}) soil heat flux, H (Wm^{-2}) and λE latent heat flux i.e the amount of energy λ ($J\ kg^{-1}$) required in the liquid to vapor transition of E ($kg\ m^{-2}\ s^{-1}$). All fluxes are defined positive when directed downward. Evapotranspiration estimation is based on calculation of λE as a residual term of eq. 3.1. and defined by the equation below.

$$\lambda E = f\{r_0(x,y), K\downarrow(x,y), \acute{\varepsilon}_2, \varepsilon_0(x,y), T_0(x,y), G(x,y), Z_{om}(x,y), kB^{-1}, u_*(x,y), L(x,y), \delta T_a(x,y)\} \quad (3.2)$$

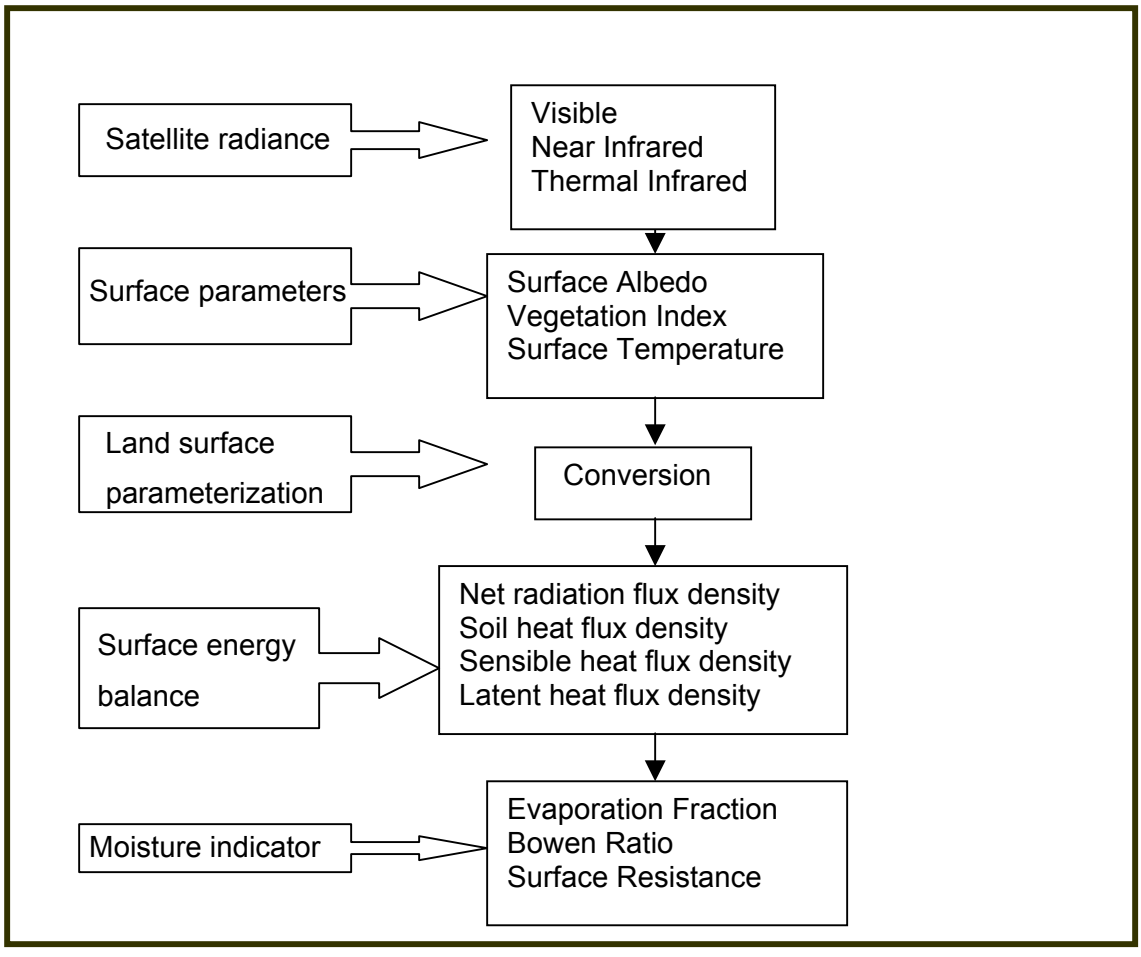

Figure 3.4 Steps of SEBAL model (after Bastiaanssen et.al., 1998)

SEBAL procedures comprises number of steps that can be categorized into four groups (fig 3.4). These are:

1. Pre- processing of satellite image. This group of steps comprises radiometric correction, geometric correction and cloud removal. Spectral radiance at the top of the atmosphere (TOA radiance) signaled by a sensor on board platform is usually a combination of emitted radiance from the earth surface, upwelling radiance from the atmosphere and downwelling radiance from the sky (Weng et al., 2004). Therefore atmospheric effect, including absorption, upward emission and downward irradiance, must be corrected before surface parameters are derived. First TOA radiances are converted in to brightness temperature and surface reflectance. The brightness temperature was corrected with spectral emissivity value before being incorporated in energy flux computation. The planetary albedo obtained from the Visible channel was radiometrically corrected to calculate surface albedo (r_0). Single band reflectance to broad band conversation was then carried out. In this study MODIS surface reflectance and land surface temperature products were used.

2. Surface parameter derivation: surface parameters collectively known as soil-vegetation-atmosphere parameters (SAVT), include Normalized Vegetation Index (NDVI), surface emissivity (ε), surface temperature (T_0) and surface roughness height for momentum transport (Z_{0m}). NDVI is derived from red and near infrared reflectance (Tucker, 1979) and the value is then used to calculate surface emissivity (Van de Griend and Owe, 1992). Z_{0m} is also scaled by NDVI (Moran and Jackson, 1991).

3. Computation of surface energy fluxes: SEBAL computes surface energy fluxes such as net radiation, soil heat flux, sensible heat and latent heat by scaling them with SAVT parameters and corrected surface reflectance. Net short wave radiation and net thermal long wave radiation are scaled by the surface albedo (r_0) and surface temperature (T_0). Soil heat flux is computed as a function of net radiation (Rn), surface temperature (T_0), surface albedo (r_0) and Normalized Vegetation Index (NDVI). SEBAL also computes sensible heat flux by self-calibration and iterative procedure. This requires manual selection of extreme dry and wet pixels ('anchor pixels) in the image. Then sensible heat (H) is computed for extreme dry pixel where $\lambda E=0$, which implies H=Rn-G and for wet pixel where H=0. This relationship bound the temperature difference between land surface temperature and the air temperature which is null at wet pixel and maximum on the dry pixel. From this temperature difference (δT_a) is scaled over the image by

linear relation with T_0. In addition to surface temperature, H is a function of aerodynamic resistance (r_{ah}). Similarly, r_{ah} is a function of H. Therefore the value for H and r_{ah} is solved iteratively using Monine-Obukhove similarity theory to account for buoyancy effect. Wind speed at reference height from metrological station/ground measurement is used to estimate wind speed at blending height and thus friction velocity (u_*) and r_{ah}. Finally latent heat flux is estimated as residual term of energy balance equation.

4. Computation of moisture indicator parameters and evapotranspiration: SEBAL generate instantaneous evaporative fraction (Λ) as a ratio of λE to Rn - G or λE + H, which is important to express energy partitioning. Then this value is used to estimate instantaneous actual evapotranspiration. Self-preservation in the diurnal evolution of energy budget is used to convert instantaneous value to daily value i.e evaporative fraction is relatively constant during the day (Mohamed et al, 2004).

The SEBAL model has been tested and validated by many in different parts of the world, for example, Egypt (Bastiaanssen and Menenti 1990), China (Wang et al 1995), Morocco (Van den Kroonenberg, A 2003), The Netherlands (Bastiaanssen and Roozekrans, 2003), Botswana (Timmermans et al., 2003), Kenya (Farah 2001) , US (Morse et al, 2000) and Turkey (Kite and Droogers 2000) as cited in Bastiaanssen et al (2005), at field scale using different measurement techniques. These works have shown capability of SEBAL to estimate surface energy fluxes and actual evapotranspiration reasonably and satisfactorily.

4 Image analysis for SEBAL parameter extraction

4.1 Introduction

Satellite based measurements provide information on atmosphere and land surface condition useful for evaporation rate estimation. The aim of this study is to estimate actual evapotranspiration with remote sensing data/images and limited ancillary weather station data using energy balance equations, also known as SEBAL model.

For this study, the SEBAL model was employed following procedures described by Bastiaanssen (1995). The method involves image rectification processes and multi-spectral image analysis to derive surface variables and energy balance components. The procedures and details of step-by-step manipulation will be discussed in subsequent sections.

4.2 Image rectification

MODIS data or products downloaded from Data Gateway were level 4G, meaning that the data had been radiometrically and geometrically corrected. The images acquired were all in hdf format and can be readily imported into a remote sensing computer software such as ERDAS IMAGINE 8.6 that performs digital image analysis. After importing, the images were re-projected from source Integerized Sinusoidal (ISIN) map projection to a standard WGS 84 UTM Zone 37 projection and re-sampled by nearest neighborhood to pixel size of 1000 by 1000 m.

4.3 Multi-spectral analysis

Estimation of surface energy flux and evapotranspiration using SEBAL model (Bastiaansen, 1995) relies on the accurate quantitative retrieval of surface parameters, such as surface reflectance (albedo), surface temperature and Normalized Difference Vegetation Index, and determination of the various components of energy balance equation. The geometrically and atmospherically rectified MODIS images were processed with multi-spectral analysis to obtain initial thematic maps displaying surface variables and radiative/conductive/convective energy fluxes. The analyses made are discussed in the following section.

4.3.1 Surface Albedo (r_0)

Surface reflectance (Albedo) is one of the most important variables in SEBAL model and is used to compute energy balance components such as net radiation and soil heat flux. MODIS Tera measures reflected radiance with in seven discrete spectral intervals over wave length range from 0.3 mm to 3 mm. Therefore conversion of reflectance computed in the range of single spectral bands is required. The broad band albedo, r_0, has been computed as a linear combination of the surface reflectance obtained in the single spectral band. The following conversion coefficients were used for the narrow to broad band conversion (Liang, 2002)

$$r_0 = 0.160r_1 + 0.291r_2 + 0.243r_3 + 0.116r_4 + 0.112r_5 + 0.081r_7 - 0.0015 \quad (4.1)$$

Where, r_0 is broad band surface albedo

$r_{1, 2,..7}$ is single band surface albedo of individual band

Using eq. 4.1 broad band albedo maps of the study area were produced form MODIS surface reflectance products. The broad band albedo derived from MODIS products acquired on individual dates of January 2006 to December 2006 is shown in app (4.1).

4.3.2 Normalized difference Vegetation Index (NDVI)

Another important physical parameter required for the SEBAL model physical application is NDVI. It is a widely known vegetation index that indicates the presence/abundance of vegetation in multi-spectral imagery. NDVI is obtained by dividing the differences in reflectance value of the near-infrared (NIR) and red (R) bands to their sum (Gorte, 2000; Tucker, 1979), and expressed as:

$$NDVI = \frac{NIR(r_2) - R(r_1)}{NIR(r_2) + R(r_1)} \quad (4.2)$$

Where, NIR (r_2) and R (r_2) are reflectance measured in MODIS channel 2 (0.841-0.876 μm) and channel 1(0.620-0.670 μm), respectively. App 4.2 shows NDVI images of study area.

4.3.3 Surface Temperature

Surface temperature is a key parameter in SEBAL model. It is related to the energy balance between soil, vegetation and atmosphere, and is controlled by the relative magnitude of heat flux densities at the land- atmosphere interface (Menenti, 2000).

MODIS thermal band 31(10.780-12.280μm) and band 32(11.770-12.270) with spatial resolution of 1000m allows retrieval of surface temperature. The generalized split-window LST algorithm was applied to retrieve LST of MODIS pixels with known emissivities in bands 31 and 32. The LST/E algorithm uses MODIS data as input such as geo-location, radiance, cloud masking, atmospheric temperature, water vapor, snow and land cover. The MODIS LST products MOD11 have been validated by in situ measurements conducted in 28 clear-sky cases including 19 cases over land sites between temperature ranges of 263-322K under column water vapor range of 0.4-4cm. In this study this products were utilized to obtain the land surface temperatures in the study area shown on app. 4.3.

4.3.4 Surface Roughness for Momentum transport (Z_{0m})

Surface roughness for momentum transport (Z_{0m}) is an important parameter in energy balance models, which influence the turbulent characteristics near the surface where the heat fluxes originate. There are different methods for determining $\mathbf{Z_{0m}}$.: wind profile method, vegetation height, look-up table etc. In this study, its value was retrieved from the following empirical relation that involves computation of soil adjusted vegetation index developed by Moran and Jackson (1991).

$$Z_{0m} = \exp(-5.809 + 5.62SAVI) \tag{4.3}$$

Where, Z_{0m} is surface roughness for momentum transport and SAVI is soil adjusted vegetation index which is given by the relation shown below (Huelten, 1985):

$$SAVI = \frac{(1+L)(r_0(NIR) - r_0(R))}{L + r_o(NIR) + r_0(R)} \tag{4.4}$$

4.3.5 Surface Roughness Length for Heat Transport (Z_{0h})

Surface roughness length for heat transport (Z_{0h}) is a parameter that corresponds to heat and water vapor transfer. It is derived from Z_{0m} by an empirical relationship adopted by (Bastiaanssen et al, 1998):

$$Z_{0h} = \frac{Z_{0m}}{\exp(kB^{-1})} \tag{4.5}$$

Where, $kB^{-1}$is santon number (heat transfer coefficient), excess resistance to heat transfer which is a factor used to compare these two parameters. Commonly a value 2.3 is applied to show the difference between Z_{0m} and Z_{0h} satisfactorily for watershede (Bastiaanssen et al., 1998).

4.4 Estimation of the fluxes in the Surface Energy Balance equation

Energy balance equation which is formulated based on the principle of conservation of energy, states that all energy evolved in the soil-vegetation-atmosphere interface comes from solar radiation, and is expressed by the equation below,

$$R_n = G + H + \lambda E \tag{4.6}$$

Where, R_n is net radiation

G is soil heat flux

H is sensible heat into the atmosphere

λE is latent heat flux which is energy used for evapotranspiration.

Equation 5.6 assumes negligible energy for photosynthesis and heat stored in vegetation.

4.4.1 Net Radiation

The net radiation is the resultant of shortwave and longwave radiation reaching and leaving the earth's surface, given by the following relation:

$$R_n = K\downarrow - K\uparrow + L\downarrow - L\uparrow \tag{4.7}$$

$$R_n = (1 - r_0)K\downarrow + \varepsilon_a \sigma T_a^4 - \varepsilon_0 \sigma T_0^4 - (1 - \varepsilon_0)\varepsilon_a \sigma T_a^4 \quad (4.8)$$

Where K↓ is incoming shortwave radiation (W/m^2)

K↑ is outgoing shortwave radiation (W/m^2)

L↓ is incoming longwave radiation (W/m^2)

L↑ is outgoing longwave radiation (W/m^2)

The outgoing shortwave radiation, K↑, which is portion of the incoming shortwave radiation that is reflected back by earth surface and atmosphere, can be expressed in terms of K↓ and surface albedo as:

$$K\uparrow = r_0 K\downarrow \quad (4.9)$$

Where, r_0 is surface albedo derived from MODIS band1,2,3,4,5, and 7 using equation 5.1.

The incoming short wave radiation (K↓) can be estimated by the following equation (Allen et al, 1998):

$$K\downarrow = (a + b\frac{n}{N})K\downarrow_{exo} \quad (4.10)$$

Where, K↓ is incoming solar (short wave) radiation

n is the hour of actual sunshine measured in the field

N is theoretical maximum hour of sunshine

a and b are coefficients in which the standard value equals 0.25 and 0.5, respectively.

The equation assumes homogenous atmospheric condition over the target area. In this study, exo-atmospheric shortwave radiation was used to derive incoming shortwave radiation using the following formula.

$$K_{exo}^{\downarrow} = G_{sc} \cdot E_0 \cos(\theta) \quad (4.11)$$

Where, $K_{exo}^{\downarrow}$ is exo-atmospheric incoming shortwave radiation.

E_0 is eccentricity correction factor

θ is solar zenith angle in radiance

G_{sc} is the solar constant (1367W/m^2)

E_0 is correction factor for variability of Earth-Sun distance as earth revolves around the earth and is given by:

$$E_0 = 1 + 0.033\cos\left(\frac{2\pi J}{365}\right) \quad (4.12)$$

Where, J (Julian day)-day number of the year ranging from 1 to 365.

The formula for estimating solar zenith angle is:

$$\cos(\theta) = \sin(\phi)\sin(\delta) + \cos(\phi)\cos(\delta)\cos(\omega) \quad (4.13)$$

Where, ø is the latitude of target area

ð is solar declination

ω is solar hour angle

The hour angle is calculated as a function of local time using the relation:

$$\omega = 15(t - 12)\frac{\pi}{180} \quad (4.14)$$

δ is the angle between the earth's equatorial plane and elliptical plane and is given by:

$$\delta = 0.409\sin(0.0172J - 1.39) \quad (4.15)$$

Solar condition during satellite overpass time are shown in table 4.1.

Table 4.1 Solar condition during satellite overpasses time

	unit	Jan. 01	Feb. 01	May. 31	Jun. 18	Oct. 31	Nov. 30
J	-	01	33	121	169	304	334
δ	rad	-0.401	-0.299	0.260	0.408	-0.268	-0.369
E_0	-	1.033	1.0278	0.9838	0.9679	1.0169	1.02686
ω	rad	-0.523	-0.523	-0.523	-0.523	-0.523	-0.523

The incoming long wave radiation has been calculated using the following equation:

$$L\downarrow = \sigma\varepsilon_a T_a^4 \quad (4.16)$$

Where, ε_a is atmospheric emissivity

T_a is temperature of the air

σ is Stefen-Boltzmann constant (5.6697 x 10^{-8} W/m^2K^4)

Average atmospheric emissivity relates to atmospheric transmittance by empirical relationship:

$$\varepsilon_{aavg} = 1.08(-\ln \tau_{sw}^{avg})^{0.265} \quad (4.17)$$

Where, τ_{sw} is average atmospheric short wave transmittance.

Computed average atmospheric short wave transmittance, average and atmospheric emissivity for the time of satellite over pass are given in table 4.2.

Table 4.2 Atmospheric transmittance and emissivity during satellite overpasses time.

	Jan. 01	Feb. 02	May. 31	Jun. 18	Oct. 31	Nov. 30
n	8.4	9.3	7.5	6.5	7.4	8.5
N	11.7	11.86	12.4	12.6	11.9	11.8
T_{sw}^{avg}	0.61	0.64	0.55	0.51	0.56	0.61
ε_a^{avg}	0.89	0.87	0.94	0.97	0.93	0.89

The air temperature at satellite overpasses time used in this study was assumed to be similar to average surface temperature of water body (the lakes). This assumption is based on the fact that water body maintains uniform surface temperature during the day time due to convection currents. This temperature is corrected for elevation using equation obtained by correlation analysis of mean water surface temperature and elevation (fig. 4.1).

Outgoing longwave radiation is a mixture of thermal radiation emitted by the surface and portion of atmospheric thermal radiation reflected from the surface. It has been computed using the following equation:

$$L\uparrow = \sigma\varepsilon_0 T_0^4 \quad (4.18)$$

σ is Stefan-Boltzmann constant (5.667 x 10^{-8} W/m^2K^4)

ε_0 and T_0 are surface emissivity and temperature obtained from MODIS products, respectively.

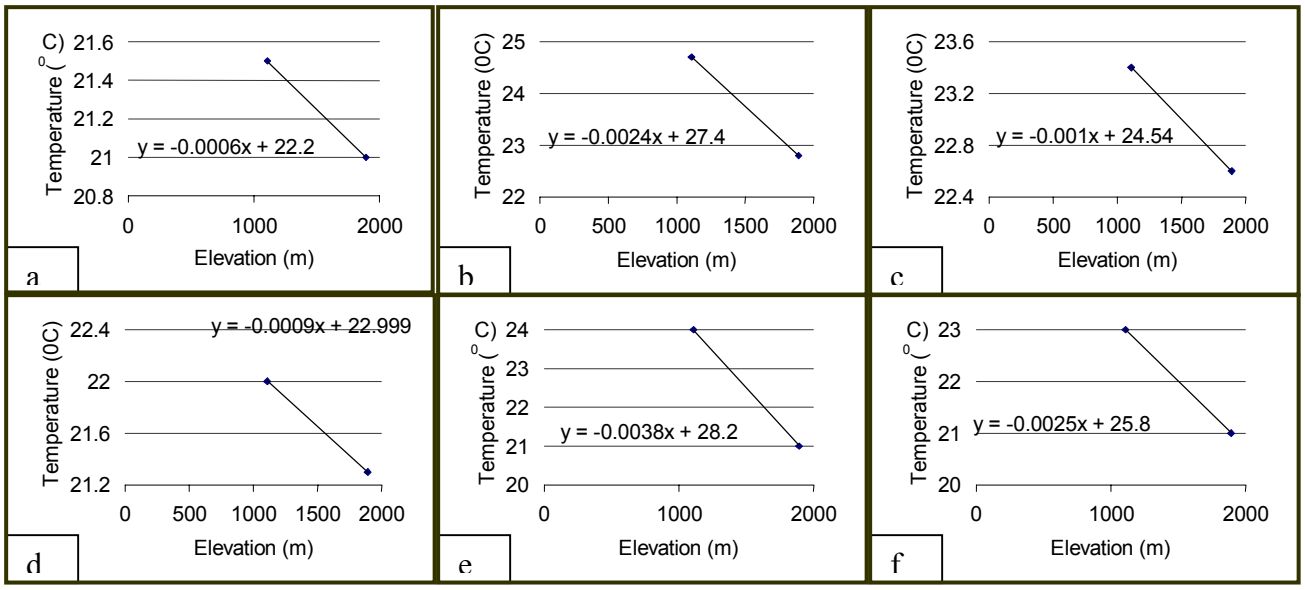

Figure 4.1 Plot of mean daily temperature Vs elevation in a) Jan. 01 b) Feb. 01 c) May 01 d) Jun. 18 e) Oct 31 and f) Nov. 30.

4.4.2 Soil Heat Flux

Soil heat flux is the transfer of heat between soil and surface through diffusion process. It depends on temperature gradient between the surface and soil and on thermal conductivity of the soil. Most soil heat flux estimation techniques rely on the empirical relationships given by Bastiaanssen (1998) as follow:

$$\frac{G}{R_n} = \frac{T_0}{r_0}\left(0.0038r_0 + 0.0074r_0^2\right)\left(1 - NDVI^4\right) \tag{4.19}$$

Where, T_0 surface temperature in ºC.

4.4.3 Sensible Heat Flux

Surface fluxes of sensible heat and momentum is calculated from Monin-Obukhov similarity theory applied to the surface layers. This theory refers to proper scaling of all the variables that affect specific phenomena in order to establish universal relationship among them. The following equation is the basis for computing sensible heat flux between the surface and the reference height:

$$H = \frac{\rho_a c_p}{r_{ah}} dT_a \quad (4.20)$$

Where, H is the sensible heat (W/m^2)

dT_a is the vertical difference in air temperature between layers z_1 and z_2 (ºK).

ρ_a is the moist air density (Kg/m^3)

c_p is air specific heat at constant pressure (J/kg ºK)

r_{ah} is aerodynamic resistance for heat transport (s/m)

Since, the sensible heat and aerodynamic resistance depend on each other; an iterative method is used, utilizing Monin-Obukhov similarity theory to correct for buoyancy effects.

i. Vertical difference in air temperature between layers (dT_a)

SEBAL model utilize two 'anchor' pixels to fix boundary condition for the energy balance. Sensible heat first computed for extreme dry and wet pixels manually identified on the images. The difference between surface (T_s) and air temperature (T_a) is given by

$$dT_a = T_s - T_a = aT_s + b \quad (4.21)$$

The spatial distribution of dT_a is calibrated inverting the sensible heat flux over both wet and dry pixels where:

1. $H \cong 0$ that implies $dT_a \cong 0$ at wet pixel and
2. $\lambda E \cong 0$ thus $H = R_n - G$ and $dT_a \neq 0$

These areas are selected considering the minimum and maximum temperature over wet and dry pixels. Area with high temperature and covered by hard rock is used to locate dry pixel where as water body is chosen to locate wet pixel.

Spatial interpolation of dT_a between its two extreme values for images can be done using surface temperature image (Basitiaanssen et al., 2002). Fitting of the minimum and maximum dT_a with minimum and maximum T_0 provide linear equations as shown in table 4.3.

Table 4.3 Linear relatationshipe between surface and air temperature.

Image	Equation
January 01	dT_a = -20 + 1.03 Ts (^{0}C)
February 02	dT_a = -27 + 1.16 Ts (^{0}C)
May 30	dT_a = -26 + 1.13 Ts(^{0}C)
June 18	dT_a = -26.4 + 1.24 Ts (^{0}C)
October 31	dT_a = -29 + 1.32 Ts (^{0}C)
November 30	dT_a = -25 + 1.18 Ts (^{0}C)

ii. Aerodynamic Resistance for Heat Transport (r_{ah})

Aerodynamic resistance for heat transport can be expressed as a function of friction velocity u_* as follow

$$r_{ah} = \frac{1}{ku_*}\ln\left[\frac{z_{ref}}{z_{oh}} - \psi_h\right] \quad (4.22)$$

Where, k is the von Karman constant (0.4)

u_* is friction velocity (m/s)

z_{ref} is upper limite for the eddy diffusivity for heat transport (m)

z_{oh} is surface roughness length for heat transport (m)

ψ_h is stability correction factor for heat transport

The friction velocity can be estimated from the wind speed at blending height and estimated surface roughness length for momentum transport:

$$\frac{1}{u_*} = \frac{1}{ku_{200}}\ln\left[\frac{z_{200}}{z_{0m}} - \psi_m\right] \quad (4.23)$$

Where, u_{200} is wind speed at 200m elevation (m/s)

Z_{0m} is surface roughness length for momentum transport (m)

ψ_m is the stability correction for buoyancy effect on momentum transport.

Z_{0m} and z_{oh} has been computed using equation 4.3 and 4.5 respectively.

The wind speed at the blending height can be derived from the logarithmic velocity profile using wind speed measurement at metrological station over grass field. The wind velocity u is given as a function of elevation by:

$$\frac{u}{u_*} = \frac{1}{k}\ln\left[\frac{z}{z_0}\right] \tag{4.24}$$

Where, u is wind speed measurement at metrological station at height of z m above the ground and $z=z_{oh}$ of grass i.e 0.001m taken from literature.

The stability correction for buoyancy effect on the momentum and heat flux can be estimated using the following formulas

$$\psi_m = 2\ln\left(\frac{1+x}{2}\right) + \ln\left(\frac{1+x^2}{2}\right) - 2\tan^{-1}x + \frac{\pi}{2} \tag{4.25}$$

$$\psi_h = 2\ln\left(\frac{1+x^2}{2}\right) \tag{4.26}$$

Where, x is given by:

$$x = \left(1 - 16\frac{z_{ref}}{L}\right)^{1/4} \tag{4.27}$$

Where, L is Monin-Obukhov length expressed as:

$$L = -\frac{\rho c_p T_0 u_*^3}{kgH} \tag{4.28}$$

In addition to wind speed at blending height, frictional velocity is also a function of Monin-Obukhove length. Solving of this function demand an iteration process as follows. The first step is to solve eq.4.23 for u_* assuming negligible buoyancy effect on momentum flux (i.e ψ_m =0). Then this value is used to compute aerodynamic roughness for heat transport under neutral condition using eq.4.22. Thus r_{ah} obtained is used to calculate sensible heat by eq. 4.20, and

allows first estimate of L by eq.4.28. This value is then used to compute the stability correction for buoyancy effect on momentum and heat flux using equations 4.25, 4.26 and 4.27. Based on the stability correction estimated above, friction velocity is again recalculated with eq 4-8, which is a second and improved estimation. This procedure is continued until convergence is reached, i.e, when the change between successive iteration is less than 1%.

4.4.4 Latent Heat Flux

Evaporation process needs conversion of water into water vapor. This requires energy input known as latent heat of vaporization. In SEBAL mode latent heat flux λE is computed as residual variables of the energy balance equation:

$$\lambda E = R_n - G - H \tag{4.29}$$

4.5 Computation of Evaporative Fraction (Λ)

Evaporative fraction is a parameter in SEBAL model to express energy partitioning. It is a parameter that indicates moisture content in a given area. It is given by:

$$\Lambda = \frac{\lambda E}{R_n - G} = \frac{\lambda E}{\lambda E + H} \tag{4.30}$$

Where, Λ is evaporative fraction.

App. 4.8 presents spatial evaporative fraction distribution of the study area at the time of satellite over pass.

The daily actual evapotranspiration have been computed from instantaneous SEBAL result based on the assumption that instantaneous evaporative fraction is equal to its daily value integrated over 24 hour period of time. Based on this assumption daily actual evapotranspiration can be computed as follows (Basitiaanssan et al., 2002):

$$ET_{a24} = \frac{86400 \times 10^3}{\lambda \rho_w} \Lambda R_{n24} \tag{4.31}$$

Where, ET_{a24} is daily actual evapotranspiration (mm/d), R_{n24} is daily net radiation (W/m^2), λ is latent heat of vaporization (J/kg) and ρ_w is density of water (kg/m^3).

Daily net radiation can be computed from daily incoming solar radiation by De Bruin (1987) equation:

$$R_{n24} = (1 - r_0)K_{24}^{\downarrow} - 110\tau_{sw24} \quad (4.32)$$

Where, $K_{24}^{\downarrow}$ is daily incoming solar radiation, can be calculated using:

$$K_{24}^{\downarrow} = 11.5741\left[\left(0.25 + 0.5\frac{n}{N}\right)K_{exo}^{\downarrow}\right] \quad (4.33)$$

Where, $K_{exo}^{\downarrow} = \frac{24}{\pi} G_{sc} \cdot E_0 \cdot \sin(\phi)\sin(\delta) \cdot (\omega_s - \tan\omega_s)$ (4.34)

Where, $G_{sc} = 1367 \times 0.0036(MJ/m^2h)$, ω_s = sunrise hour angle

$$\cos(\omega_s) = -\tan(\phi) \cdot \tan(\delta) \quad (4.35)$$

5 Results and Discussion

5.1 Spatial patterns of temporal changes in land surface temperature

The mean and standard deviation of land surface temperature in the basin derived from the images are given in Table 5.1. The regions towards the south-central part of the basin (shown by pixels concentrated near the lakes) exhibit greater surface temperatures than surrounding areas in all images. Some of these pixels correspond to the relatively limited hot-springs and thermal areas located within the basin. The hydrothermal activity effects can be compared with the relatively lower temperature responses at the south eastern part of the study area, where the surface is dominated by more established vegetation covers. The highlands on the eastern and western flanks of the study area are generally colder due to the influence of relatively high vegetation cover. The influence of variations in the moisture status of the basin can also be observed. The images from the predominantly hotter and drier winter period contrast well with the generally cooler and wetter conditions prevalent during summer. The degree of spatial variation in the surface temperature differences on any one day is revealing, especially when spatial variability in moisture status is higher. Clearly, there is inverse correlation between the surface temperature and the underlying surface condition/vegetation (fig 5.1a &b).

Table 5.1 Mean temperature and NDVI of selected days in 2006.

	JAN	FEB	MAY	JUN	OCT	NOV
LST	303	308	302	299	296	299
NDVI	0.361	0.326	0.466	0.540	0.511	0.502

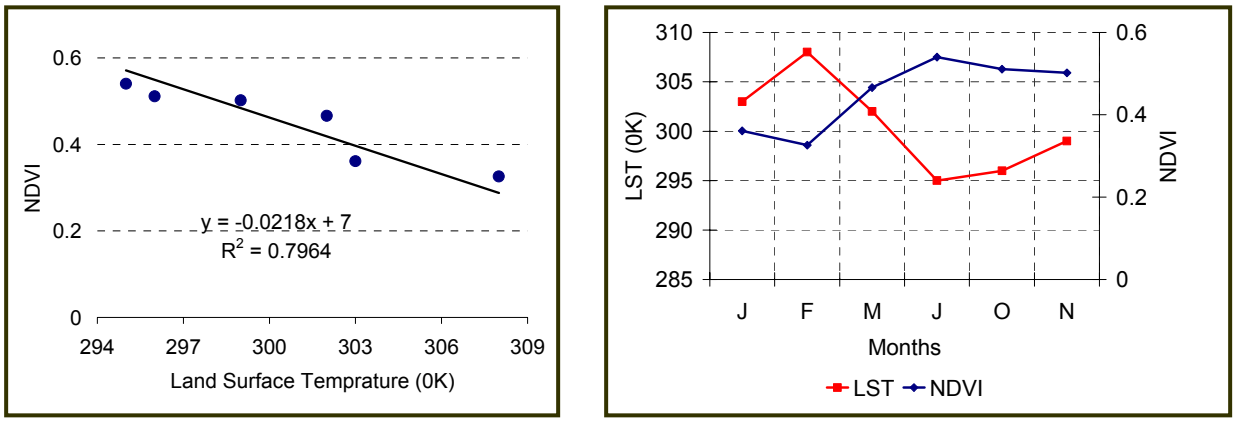

Figure 5.1 Relationship between land surface temperature and NDVI in the study area.

5.2 Spatial and temporal Variability of land surface evapotranspiration

The spatial and temporal variability of actual evapotranspiration and energy flux in the study area are discussed in the following sub-sections. The discussion focuses on the results obtained from three types of land use/cover classes; natural vegetation (bush, grass, forest and woodlands), agricultural land and water bodies in three physiographic regions, besides temporal variability will be assessed.

The elevation difference between the highland (upstream end) and the rift floor (downstream end) of the watersheds is greater than 2000m. Owing to wide variability in altitude, mean monthly and annual climatic parameters vary considerably within the basin. The highland is characterized by humid climate whereas arid climate prevails towards rift center. In view of this the spatial distribution of ETa is described with respect to three major independent physiographic regions: Highland, Escarpment and Rift center (see figure 1.2 in section 2.2).

5.2.1 Spatial distribution of ETa in Winter

For land surface, ETa in January ranges from nearly 0 $mm.day^{-1}$ for bare land and river bed in the rift to 4.04 mm. d^{-1} in the highlands. The mean ETa value is about 1 mm. d^{-1} and standard deviation of 0.46. In February ETa from land surface ranges from nearly 0 to 4.06 mm. d^{-1} with mean and standard deviation of 1.52 and 0.39 mm. d^{-1}, respectively. Figure 5.2 and 5.3 show the histogram of evaporative fraction and daily actual evapotranspiration in January and February, 2006. The spatial distribution pattern of the daily ETa in February appears similar to that in January. The highest values for land surface in both cases are observed on the eastern highland and southern part of the study area where there are marshy/swamp areas (fig 5.17 & 5.18), whereas the northern part of the basin exhibits generally lower ETa values. However, there is an increment in daily evaporative loss between January and February by approximately 0.52 $mm.d^{-1}$. The spatial variability of ETa is relatively higher in January as compared to ETa in February, and is marked by higher standard deviation. Evaporative fraction also follows the same pattern as daily evapotranspiration. Its value ranges from nearly zero for bare land and river bed in the rift floor, to about a maximum of 0.5 in the highlands covered by grass (fig 5.2a). This indicates the dominance of sensible heat in the basin during winter season. Higher evaporative fractions, greater than 0.8, are obtained for water bodies (lakes and swamp area).

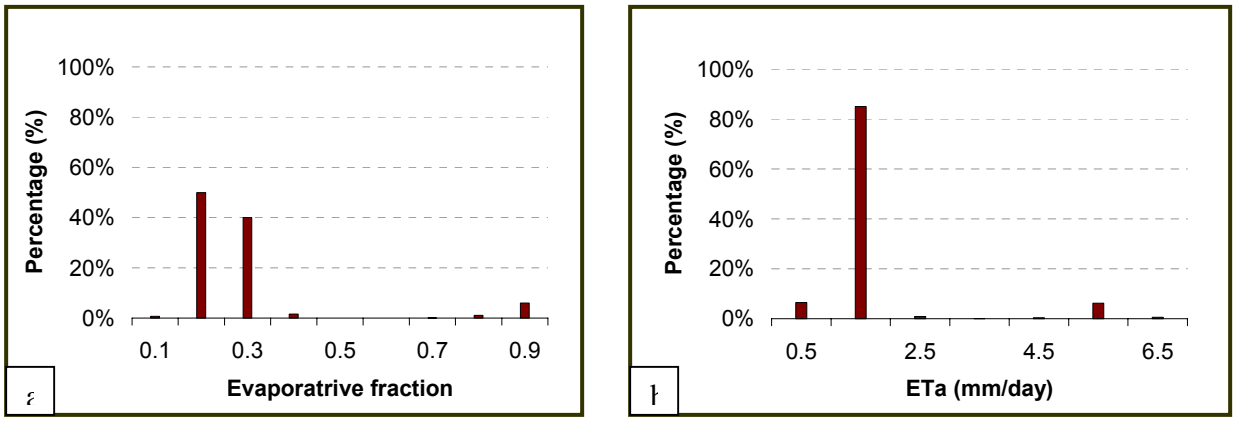

Figure 5.2 Histogram of a) evaporative fraction and b) daily actual evapotranspiration in Jan. 2006.

Statistics for SEBAL land surface ETa over each land cover type derived from January and February 2006 MODIS images were determined and are presented in Table 5.2 and 5.3 for the rift, escarpment and highland.

In January 2006 it is observed in the ET_a map (fig. 5.17) and plot of ETa against land cover (fig 5.4) that grass land loss relatively higher amount of water by evapotranspiration in the rift, escarpment and highland with mean ETa of 1.43, 1.54 and 1.76 mm day^{-1} , respectively. In part of the highlands covered with bushes and shrubs the estimated ETa reaches up to 4.16 while grassland in escarpments received highest estimated ETa record as much as 4.12 mm day^{-1} (Table 5.2). The highest mean ETa value from farm land in the rift is resulted from mid-season stage crop developed through irrigation and in swamp of the plain. In contrast to rainfall deficit, soil moisture condition is higher over some farm lands of rift valley suggesting irrigation practice. This also indicated by higher NDVI (App. 4.4 a & b). But vast farm land with wood and grassland that depends on rain has relatively low ETa, in the order of 0.02 to 1.97 with mean and standard deviation of 0.63 mm day^{-1} and 0.26 mm day^{-1}, respectively. Comparison of ETa over different land cover type in January and February is shown in figure 5.4 and 5.5.

In February 2006 the general trend of estimated evapotranspiration over each land use/cover type also appears similar to that of January. But in February the ETa over all land cover type increases due to higher incoming solar radiation and prior rainfall incidence. Incoming solar radiation increased by 5.6% from previous month that is from 231 watt $meter^{-2}$ day^{-1} in January to 244 watt $meter^{-2}$ day^{-1} . Mean surface temperature and wind speed also increased by 5% and 7%, respectively. Farm land with wood and grassland in the rift and escarpment had

relatively minimum mean ETa of 1.10 and 1.28 mm day^{-1} , respectively (Table 5.3). The plot of mean ETa in February over individual land use/cover type in the three major physiographic regions is presented in Figure 5.5.

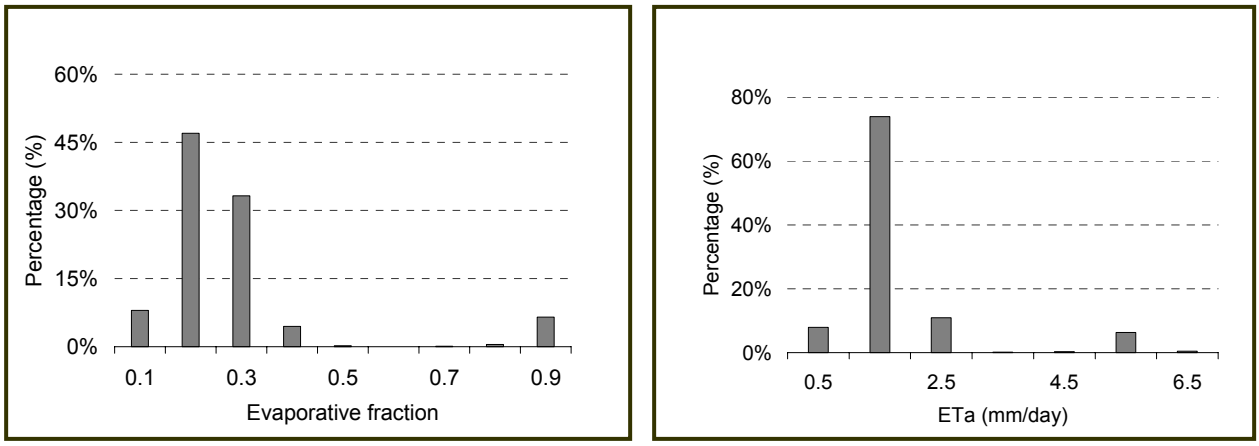

Figure 5.3 Histogram of a) evaporative fraction and b) actual evapotranspiration in February 2006.

Spatial variability of ETa in each land use/cover classes were assessed in relation to standard deviation. Comparative assessment of standard deviation of ETa over each land use/cover indicates agricultural land exhibited high spatial variability followed by bush and grass land. This was due to soil moisture variability and presence of other land use/cover classes that belonged to other classes.

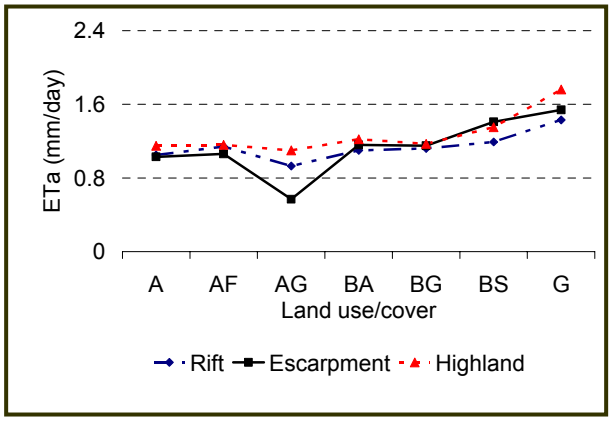

Figure 5.4 Plot of ETa against each land use/ cover type in January.

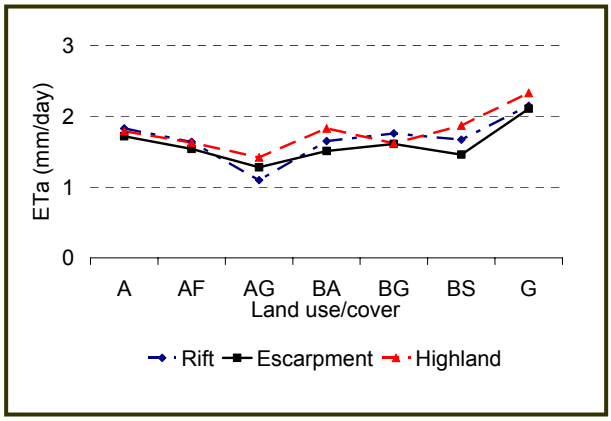

Figure 5.5 Plot of ETa against each land use/cover type in February.

The winter season evaporative loss (January and February, 2006) was more than the season precipitation (P) in the basin and varied with land use and climatic zone delaminated by altitude (Fig.1.6 & 1.7). The highland show high daily ETa values compared to other region due to

available soil moisture condition in the root zone. The lowland (rift) in the north had the lowest ETa for all the land use classes in the basin. This was because of soils moisture deficit.

5.2.2 Spatial distribution of ETa in autumn

There is distinct difference in ETa values between the northern and southern part of the area. Figure 5.19 and App. 4.4c presents estimated ETa and evaporation fraction on May 01, 2006. Relatively low ETa values ranging from 0.5 to 0.90 mm d^{-1} are mainly located in the northern part of the basin in the low lands (rift). High ETa values, from 3.5 mm d^{-1} up to 4.11mm d^{-1}, that correspond to high evaporation fraction are typical of the eastern and western highlands as well as in the southern part of the study area. Highest ETa values are also found in the north part of the rift close to swamps and irrigation sites. As shown in the histogram of (Figure 5.6a) evaporative fraction values range between 0.2 to 0.5 mostly. Higher values between 0.8 and 1are also noted for water body (lakes).

The statistics and plot of ETa for each land use/cover type are shown in Table 5.4 and Figure 5.8. For land surface, in the rift, mean actual evapotranspiration varied from 2.94mm d^{-1} for agricultural area with grass and wood land to 3.04 mm d^{-1} for grass land. In the escarpment the highest mean ETa was scored by agricultural and forest area with mean value of 2.96. Mean ETa from the highland ranges from 2.90 mm d^{-1} in agricultural and bush area to 2.98 mm d^{-1} in agriculture with forest land.

Bush with grass land exhibited relatively high ETa spatial variability in the escarpment followed by agricultural area with grass and wood land in the rift and escarpment too. Spatial ETa variability was low in the highland. Higher variability in ETa in the rift resulted from variability in soil moisture content due to difference in rainfall pattern north and south of 6^0 30' latitude.

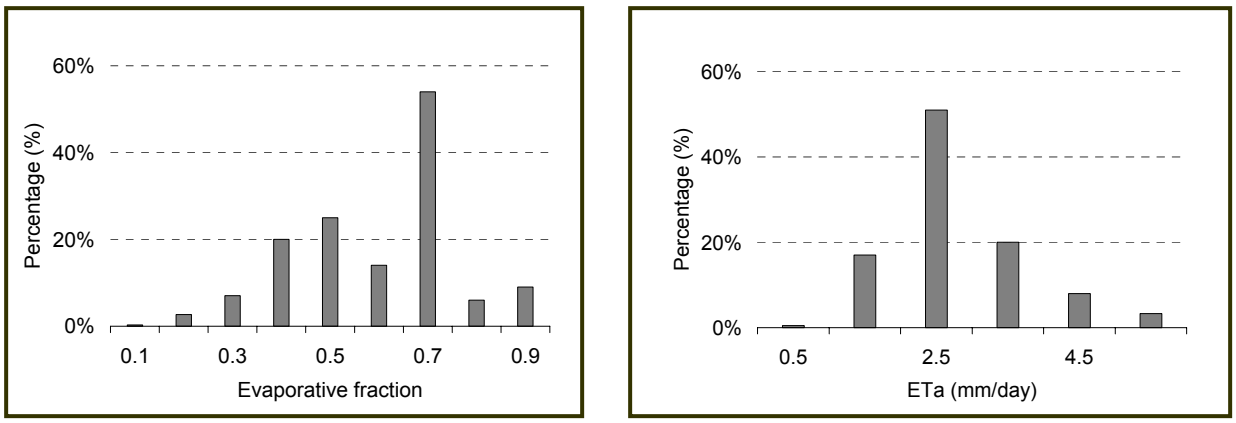

Figure 5.6 Histogram of a) evaporative fraction and b) daily actual evapotranspiration in May, 2006.

5.2.3 Spatial distribution of ETa in summer

The spatial variation of actual daily evapotranspiration and evaporative fraction derived from MODIS data acquired on June 18, 2006 are presented in figure 5.20 and App.4.4. Figure 5.7 presents the histogram of evaporative fraction and ETa. Land surface ETa ranges from 2.23 mm d^{-1} for bush land in the highland to about 2.57 $mm.d^{-1}$ for agriculture area and grass land in the rift.

Daily evapotranspiration has a similar spatial distribution pattern with evaporative fraction. For land surface, it ranges from 0.5 to 0.68 that indicate the dominance of latent heat as compared to dry season's dates.

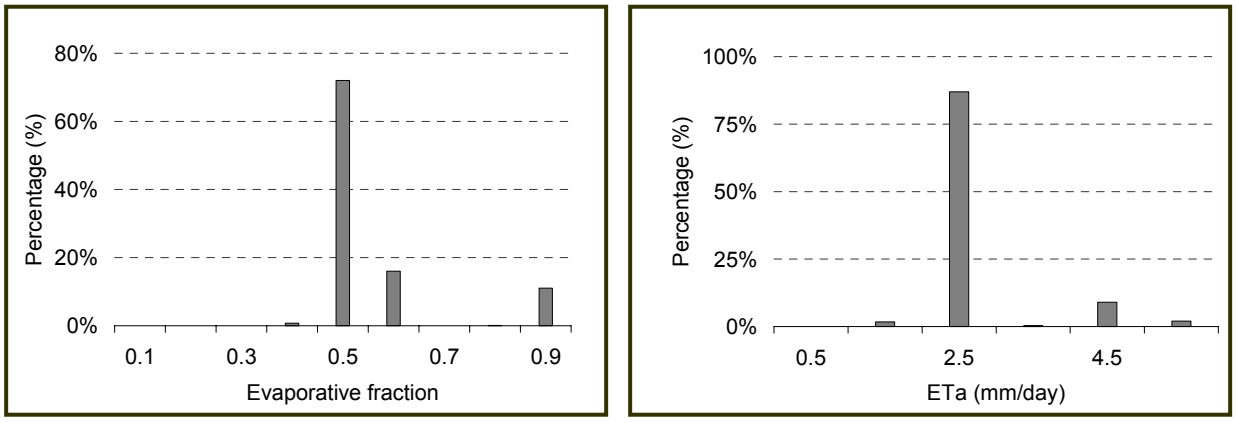

Figure 5.7 Histogram of a) evaporative fraction and b) daily actual evapotranspiration in June 2006.

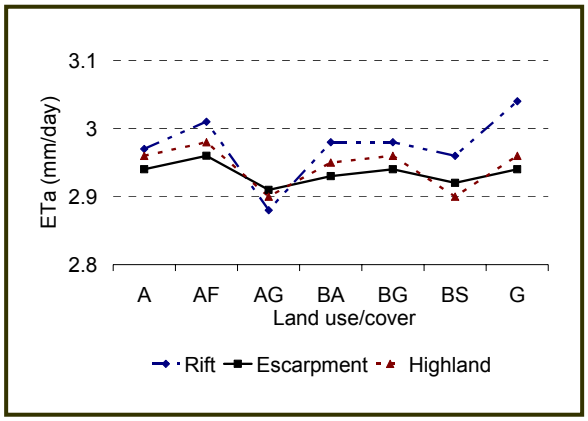

Figure 5.8 Plot of ETa over individual land use/ cover in May, 2006.

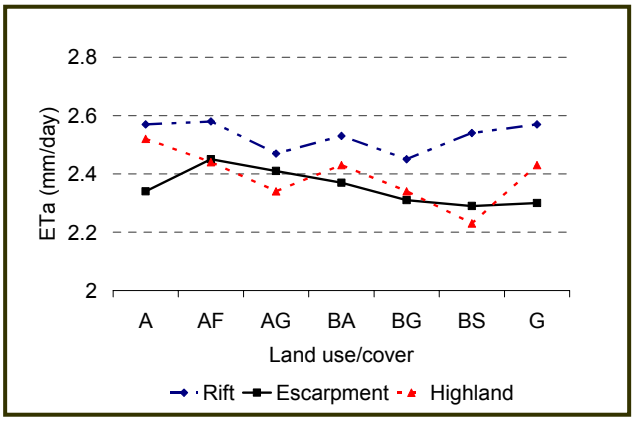

Figure 5.9 Plot of ETa over individual land use/ cover in June, 2006.

Table 5.5 shows the minimum, maximum and mean evapotranspiration for eight land use/cover type in the rift, escarpment and highland. Figure 5.9 represents the distribution of ETa in terms of different land use/cover types. It is clear from Figure 5.9 that in the rift the highest values are found in agriculture with forest land followed by agricultural land, grass land, bush-shrub land and bush land with farming plot. In the escarpment and plateau areas forest with farming plot has the highest ETa followed by bush land and agricultural land. Bush land scored the lowest ETa in the escarpment and plateau.

The degree of variation of ETa within each land use/cover type in the rift, escarpment and plateau is demonstrated with reference to standard deviations. Agricultural land mixed with grass and wood land, and bush land with grass exhibits relatively higher ETa variability in the rift, escarpment and highland with standard deviation 0.20, 0.18 and 0.16 mm d^{-1}. In general, spatial variability during this period is relatively low, which is a characteristic of wet basin.

5.2.4 Spatial distribution of ETa in spring

The spatial distribution of ETa in spring over Lake Abaya-Chamo basin is presented and discussed based on results obtained from two images; October 31 and November 30.

The spatially distributed pattern of actual evapotranspiration and evaporative fraction in October are presented in Figure 5.21 and app. 4.4. The estimated evapotranspiration varies over a wide range from 0.4 mm d^{-1} to 6.05 mm d^{-1} in the rift for dry river beds and open water body (lakes), respectively. The histogram of ETa and evaporative fraction are shown in Figure 5.10. For land

surface the highest values of 3.32 mm d^{-1} ETa be found in the rift mostly in the southern part of the study area. The lowest values from land surface area are mostly distributed on the rain fed agricultural land in the northern part of the area. The spatial distribution evaporative fraction have similar pattern as actual daily evapotranspiration.

The distribution patterns in daily ETa statistics and plot of ETa against land use/cover type (Table 5.7 and Figure 5.12) demonstrate that in the rift grass lands have highest mean ETa values of 2.85. Agricultural land make up about 52% of the rift and have mean ETa values that ranges from 2.51 mm d^{-1} when it is mixed with grass and wood land to 2.77 mm d^{-1} when it becomes pure agricultural area. Bush land in the rift exhibit nearly homogenous ETa values in rang of 2.56 to 2.85 mm d^{-1}. In the escarpment and highland ETa distribution pattern over each land use/cover type seems similar to the rift. But mean values in the highland are considerably higher than the escarpment for all land use/cover types.

ETa values in the rift are higher than the escarpment and highland (fig 5.12). This is due to high temperature and moisture availability due to rainfall event in the area.

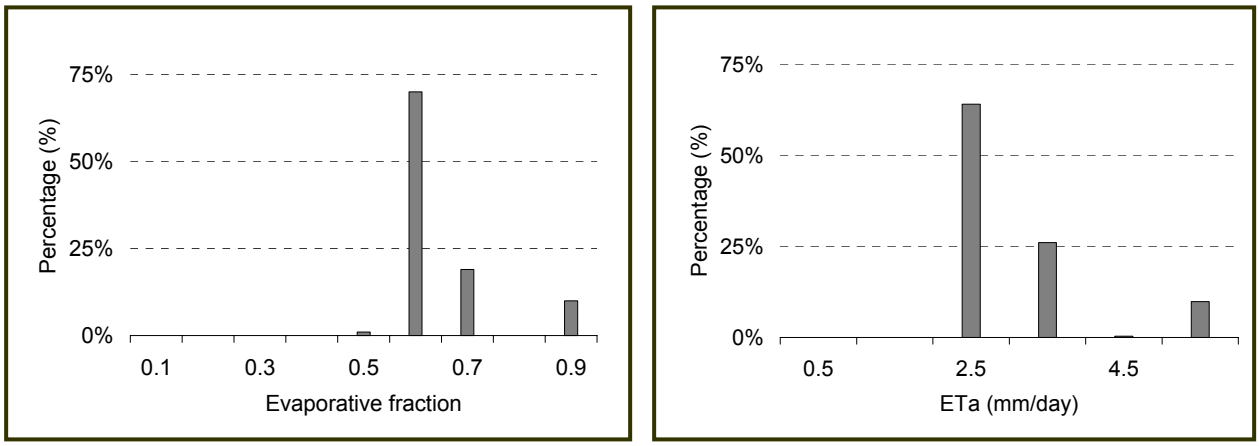

Figure 5.10 Histogram of a) evaporative fraction and b) daily actual evapotranspiration in Oct. 2006.

In November the spatial distribution of ETa was similar to that of October though the later showed slightly lower ETa. The spatial distribution of daily actual evapotranspiration, evaporative fraction and their histograms are shown in Figure 5.22, app. 4.4 and Figure 5.11, respectively. For land surface, higher values are noted in the east and west highlands as well as on the southern rift close to the lakes and swamp area. The ETa spatial distribution is relatively higher

in low land areas in the north central part of the basin than that of elevated areas in east and west. The lower values from previous month may be due to depletion of soil moisture.

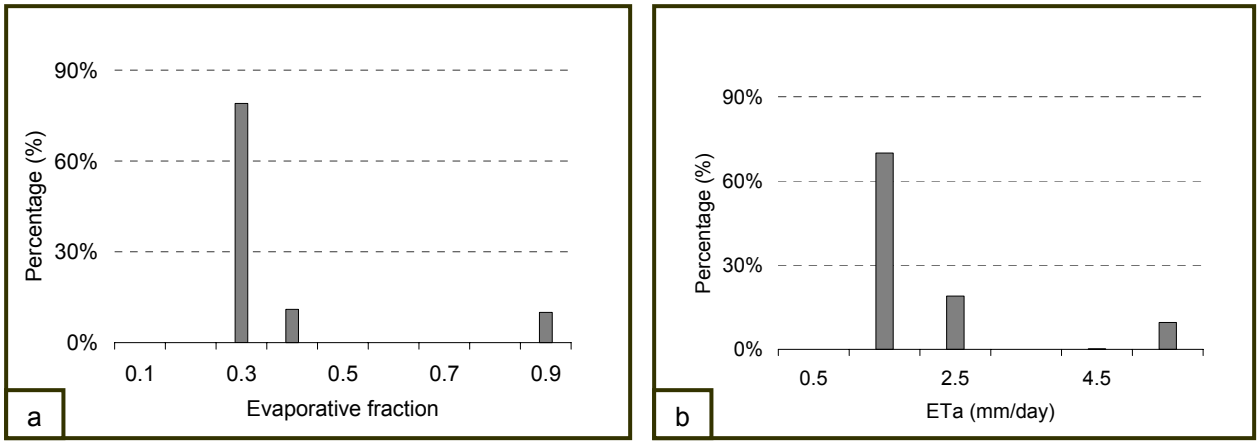

Figure 5.11 Histogram of a) evaporative fraction and b) daily actual evapotranspiration in Nov 2006.

Table 5.7 shows the basic statistics of ETa in different land use/cover types. Figure 5.13 represent the distribution of mean ETa in terms of different land use/cover types for three major physiographic regions: rift, escarpment and plateau.

As shown in Figure 5.13 agricultural land with grass and wood (AG) land have lowest ETa in the rift, escarpment and highland with mean value of 1.88, 1.81 and 1.96 mm d^{-1}, respectively. The highest ETa from land surface in the rift was found in the grass (2.13 mm d^{-1}) and bush lands (2.14 mm d^{-1}). Agricultural lands in the highland have higher ETa values than in the rift. Where as evaporation from bush and grass land is higher in the rift. In the escarpment ETa values are low for all land use/cover types.

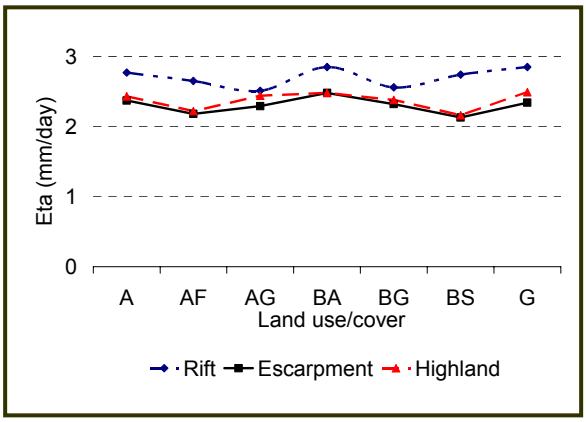

Figure 5.12 Plot of ETa over individual land use/ cover in October 2006.

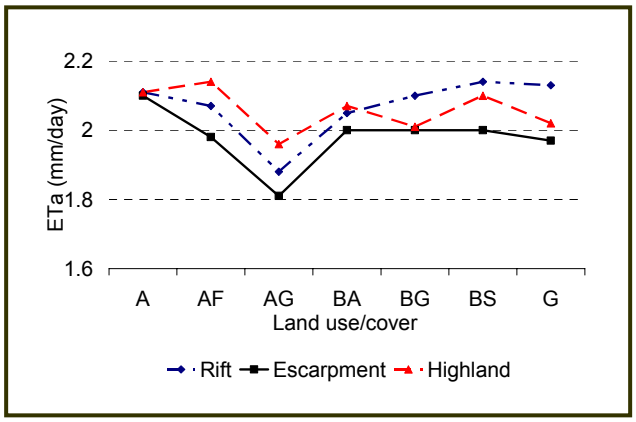

Figure 5.13 Plot of ETa over individual land use/ cover in November 2006.

In both months the highest ETa variability occurs in the rift followed by escarpment while the highland scored the lowest variability in the corresponding land use/cover type. Agricultural area scored the highest standard deviation in the rift as well as in the escarpment. Grass land in all physiographic region exhibits the lowest variability with standard deviation of 0.24 mm d^{-1} or less. The spatial variability of ETa over each land use/cover in the highland is generally small.

5.3 Lake evaporation

SEBAL evaporation results showed difference in rate of evaporation between lake Abaya and lake Chamo, (see in table 5.8 and figure 5.14). This is associated with differences in the composition of lake water which causes variation in lake albedo and lake surface temperature. Surface temperature is higher in lake Chamo, where as albedo varies inversely such that Abaya has relatively higher reflectance than Chamo. Previous studies indicate high content of silt in lake Abaya (Schuett et al 2004). Moreover, SEBAL ETa shows spatial variability over the water body depending on lake surface temperature and albedo.

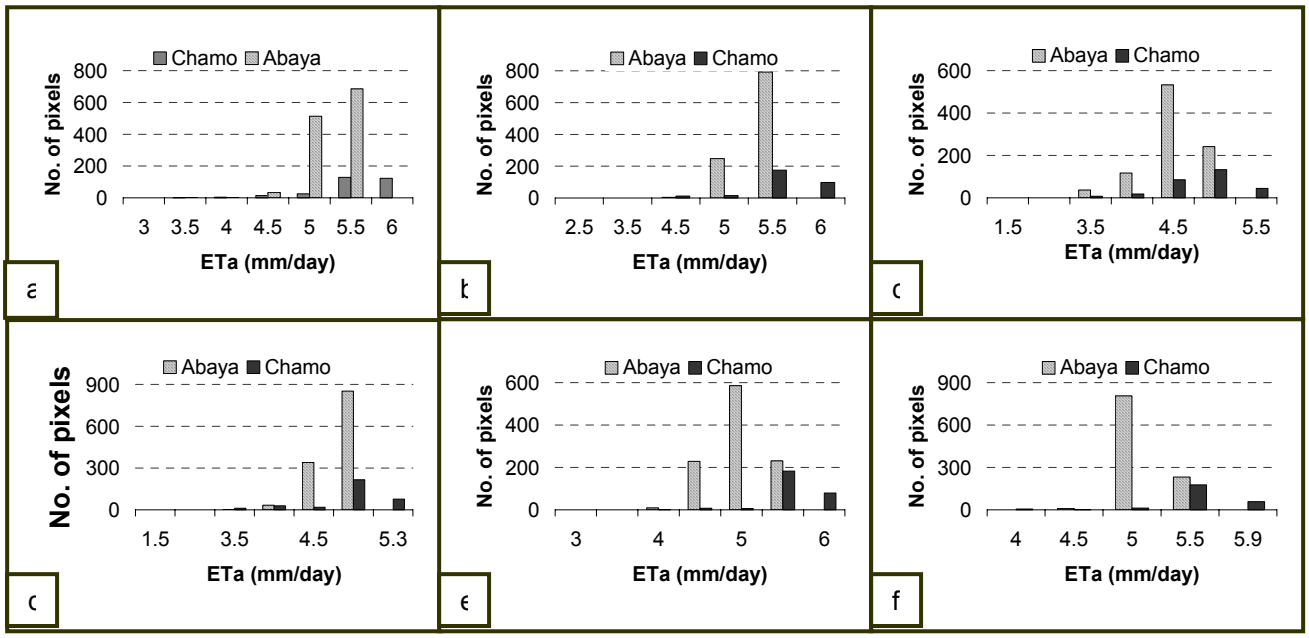

Figure 5.14. Histogram of lake evaporation a) Jan. b) Feb. c) May d) Jun. e) Oct. f) Nov. of 2006.

Table 5.2 Statistics of daily actual evapotranspiration over each land use/cover type in January 2006.

	Rift				Escarpment				Highland			
	Min.	Max.	Mean	St.de	Min.	Max.	Mean	St. de	Min.	Max.	Mean	St. de
Agr, grass &wood	0.02	1.97	0.63	1.21	0.42	2.08	0.87	0.94	0.68	1.87	1.10	0.16
Bush, shrub land	0.34	2.20	1.19	0.78	0.59	2.25	1.41	0.39	0.76	2.10	1.35	0.27
Agr. With forest	0.31	2.15	1.14	0.56	0.48	2.12	1.06	0.72	0.61	1.94	1.16	0.16
Bush &grass land	0.45	3.08	1.12	1.16	0.50	4.02	1.15	0.98	0.64	1.22	1.17	0.19
Grassland	0.47	4.18	1.43	0.54	0.66	4.12	1.54	0.61	0.88	4.23	1.76	0.73
Agriculture	0.41	3.19	1.25	0.95	0.51	1.84	1.03	0.58	0.77	1.63	1.15	0.32
Bush & agri	0.53	2.84	1.10	1.14	0.97	4.10	1.16	0.54	0.72	4.16	1.22	0.78

Table 5.3 Statistics of daily actual evapotranspiration over each land use/cover type in February 2006.

	Rift				Escarpment				Highland			
	Min.	Max.	Mean	St.de	Min.	Max.	Mean	St. de	Min.	Max.	Mean	St. de
Agr, grass &wood	0.005	1.71	1.11	1.15	0.69	2.50	1.28	0.74	1.02	2.80	1.42	0.64
Bush, shrub land	0.27	3.30	1.67	0.82	1.06	2.49	1.86	0.60	1.19	2.31	1.87	0.58
Agr. With forest	0.71	2.83	1.34	0.74	1.15	2.83	1.54	0.56	1.29	2.90	1.63	0.27
Bush &grass land	0.82	3.69	1.46	0.62	1.28	2.25	1.61	0.33	1.39	2.17	1.62	0.43
Grassland	1.13	4.19	2.15	0.41	1.57	3.34	2.19	0.31	0.80	3.13	2.33	0.71
Agriculture	0.03	2.96	1.83	0.95	0.46	1.38	1.72	0.39	0.47	2.19	1.79	0.24
Bush & agri	1.22	2.94	1.65	0.53	1.27	2.75	1.81	0.54	1.43	2.24	1.83	0.30

Table 5.4 Statistics of daily actual evapotranspiration over each land use/cover type in May 2006.

	Rift				Escarpment				Highland			
	Min.	Max.	Mean	St.de	Min.	Max.	Mean	St. de	Min.	Max.	Mean	St. de
Agr, grass &wood	0.43	4.10	2.88	2.97	0.96	1.40	4.04	2.94	0.64	1.23	2.86	2.96	0.18
Bush, shrub land	1.03	4.06	2.96	3.01	0.53	1.20	3.75	2.96	0.39	1.60	2.83	2.98	0.17
Agr. With forest	0.85	4.10	3.01	2.88	0.89	1.51	3.66	2.91	0.42	1.78	2.87	2.90	0.13
Bush &grass land	1.20	4.07	2.98	2.98	0.63	1.12	3.68	2.93	0.48	-	-	2.95	-
Grassland	1.30	4.05	3.04	2.98	0.67	1.52	4.05	2.94	0.51	-	-	2.96	-
Agriculture	1.51	4.11	2.97	2.96	0.55	1.26	3.68	2.92	0.60	-	-	2.90	-
Bush & agri	1.22	4.10	2.98	3.04	0.64	1.97	3.81	2.94	0.54	-	-	2.96	-

Table 5.5 Statistics of daily actual evapotranspiration over each land use/cover type in June 2006.

	Rift				Escarpment				Highland			
	Min.	Max.	Mean	St.de	Min.	Max.	Mean	St. de	Min.	Max.	Mean	St. de
Agr, grass &wood	1.31	3.05	2.47	0.20	1.59	2.96	2.41	0.18	1.53	2.82	2.34	0.14
Bush, shrub land	1.88	3.16	2.54	0.16	1.38	2.86	2.29	0.23	1.66	2.51	2.23	0.12
Agr. With forest	1.43	3.03	2.58	0.17	1.42	3.07	2.45	0.22	1.88	3.01	2.44	0.17
Bush &grass land	1.24	3.10	2.45	0.18	1.26	2.94	2.31	0.29	1.57	2.65	2.34	0.14
Grassland	2.05	3.32	2.57	0.15	1.51	2.96	2.30	0.22	-	-	-	-
Agriculture	1.61	3.18	2.58	0.17	1.46	3.12	2.34	0.23	1.42	2.85	2.52	0.14
Bush & agri	2.11	3.12	2.53	0.15	2.11	2.96	2.37	0.14	1.25	2.79	2.46	0.16

Table 5.6 Statistics of ETa in the three physiographic regions over each land use/cover in October 2006.

	Rift				Escarpment				Highland			
	Min.	Max.	Mean	St.de	Min.	Max.	Mean	St. de	Min.	Max.	Mean	St. de
Agr, grass &wood	0.36	3.34	2.51	1.19	2.10	3.17	2.49	0.13	1.54	3.09	2.44	0.10
Bush, shrub land	2.53	3.58	2.74	0.10	2.13	3.51	2.33	0.15	1.55	3.21	2.16	0.28
Agr. With forest	2.50	3.82	2.67	0.12	2.07	3.47	2.28	0.10	1.50	3.15	2.22	0.49
Bush &grass land	2.39	3.32	2.56	0.13	1.63	3.19	2.32	0.44	1.79	3.08	2.48	0.46
Grassland	2.33	3.62	2.85	0.10	2.17	3.54	2.34	0.10	1.77	3.54	2.49	0.76
Agriculture	2.13	3.40	2.77	0.11	0.81	3.28	2.37	0.60	1.70	3.17	2.38	0.37
Bush & agri	0.14	3.63	2.84	0.67	2.22	3.17	2.48	0.11	1.75	3.11	2.44	0.67

Table 5.7 Statistics of ETa in the three physiographic regions over each land use/cover in November 2006.

	Rift				Escarpment				Highland			
	Min.	Max.	Mean	St.de	Min.	Max.	Mean	St. de	Min.	Max.	Mean	St. de
Agr, grass &wood	0.0	2.30	1.88	1.19	1.65	2.37	1.81	0.11	1.75	2.15	1.96	0.10
Bush, shrub land	1.80	2.47	2.14	0.17	1.27	2.24	2.00	0.11	1.87	2.11	2.10	0.07
Agr. With forest	0.97	2.44	2.07	0.13	1.19	2.41	1.98	0.10	1.78	2.18	2.14	0.06
Bush &grass land	0.83	2.32	2.10	0.25	1.72	2.20	2.00	0.14	1.96	2.12	2.01	0.05
Grassland	1.70	2.49	2.13	0.10	1.67	2.29	1.97	0.13	2.04	2.19	2.02	0.03
Agriculture	0.74	2.37	2.11	0.91	1.26	2.43	2.10	0.12	1.98	2.25	2.11	0.06
Bush & agri	1.69	2.52	2.05	0.12	0.72	2.22	2.00	0.14	1.95	2.15	2.07	0.08

Table 5.8 Mean ETa from Lakes in the study area, 2006.

	LakeAbaya Evporation.				Lake Chamo Evporation			
	Min	Max.	Mean	St.dev.	Min	Max.	Mean	St.dev
Jan.	3.92	5.95	5.57	0.27	3.87	6.21	5.84	0.4
Feb.	4.96	5.95	5.79	0.25	4.70	6.08	5.88	0.3
May	3.45	5.37	4.73	0.30	3.50	5.63	4.99	0.3
Jun.	3.39	4.89	4.57	0.23	3.28	5.17	4.84	0.4
Oct.	4.67	5.71	5.53	0.12	4.80	6.11	5.90	0.2
Nov.	4.80	5.64	5.45	0.12	4.04	6.00	5.78	0.3

5.4 Temporal variability of ETa

In this study daily ETa analysis was made on seasonal basis and is represented as follows: 1) Winter represented by January and February 2) Autumn represented only by May 3) Summer represented only by June and 4) Spring represented by October and November. Since evapotranspiration varies according to weather types and is therefore dependent on seasons, there are variations in the pattern of actual evapotranspiration during a year. Figure 5.15 represents time series daily evapotranspiration over Lake Abaya-Chamo basin for six months in 2006.

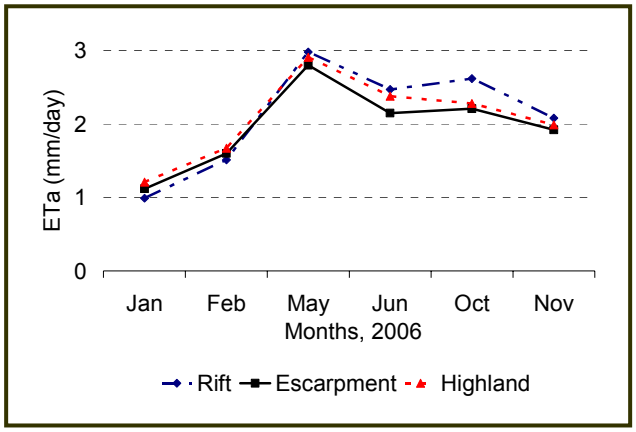

Figure 5.15 Time series plot of ETa from land surface in year 2006.

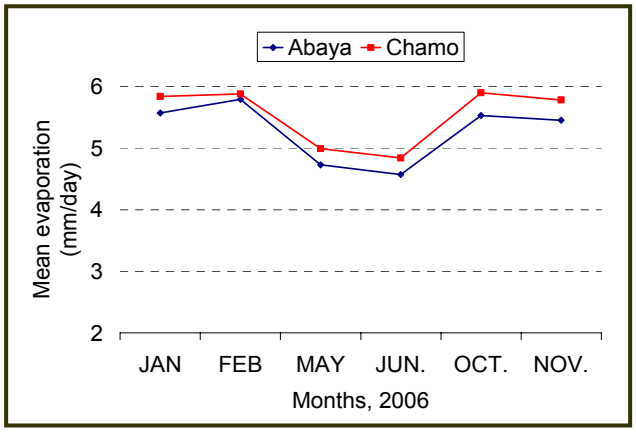

Figure 5.16 Time series plot of lake evaporation in year 2006.

Despite relatively higher solar radiation, wind speed and lower relative humidity, hot and dry winter and spring days exhibit relatively low ETa (fig. 5.15), excluding the lakes. This period is

characterized by an average evaporative fraction not exceeding 0.4. This indicates soil moisture depletion and dominance of sensible heat flux across the catchment, and the corresponding rise in surface temperatures. In winter and spring seasons, the rift floor is usually dry and higher evapotranspiration values are limited to swamps/marshy areas of Bilate, Gidabo and Gelana Rivers.

In contrast to an increase in relative humidity, reduction in solar radiation and wind speed, the season of autumn and summer record relatively higher and uniform evapotranspiration rate over a wide area mainly related to varying intensity rainfall events and an associated increase in soil moisture content throughout the catchment (fig. 5.15 & 5.19). The spatial patterns evaporation in autumn and spring days significantly denotes the wetting dynamics of the basin, such that an increase in moisture content is followed by higher rate of evapotranspiration rate. The EF from the land surface reached a maximum value of 0.78 in autumn and summer. The reduction of evaporation rate in summer season is associated with an increase in humidity and decrease in solar radiation.

Unlike the wet seasons (autumn and summer), high mean ETa values is noted in the warm winter season on the highlands and is may be due to availability of water in the root zone. The escarpment is characterized by lower mean ETa values in all seasons compared to the rift.

The degree of variation with time is demonstrated in reference to the standard deviations. The standard deviations are linked with soil moisture condition in certain period of time. Dry periods exhibit greater variability than wetter periods. This is indicated by an increased in standard deviation between 0.87 and 1.2 mm/day during dry season, in contrast to other periods maintaining standard deviations less than 0.5mm/day.

As far as temporal variability in lake water evaporation is concerned, warm winter days exhibit higher evaporation rate followed by spring, and autumn dates while summer days have lowest evaporation. Figure 5.16 provide time series daily plots of evaporation rate for the two lakes. Evaporation rate in lake Chamo is higher than that of lake Abaya in all days of the season under consideration (Table 5.8).

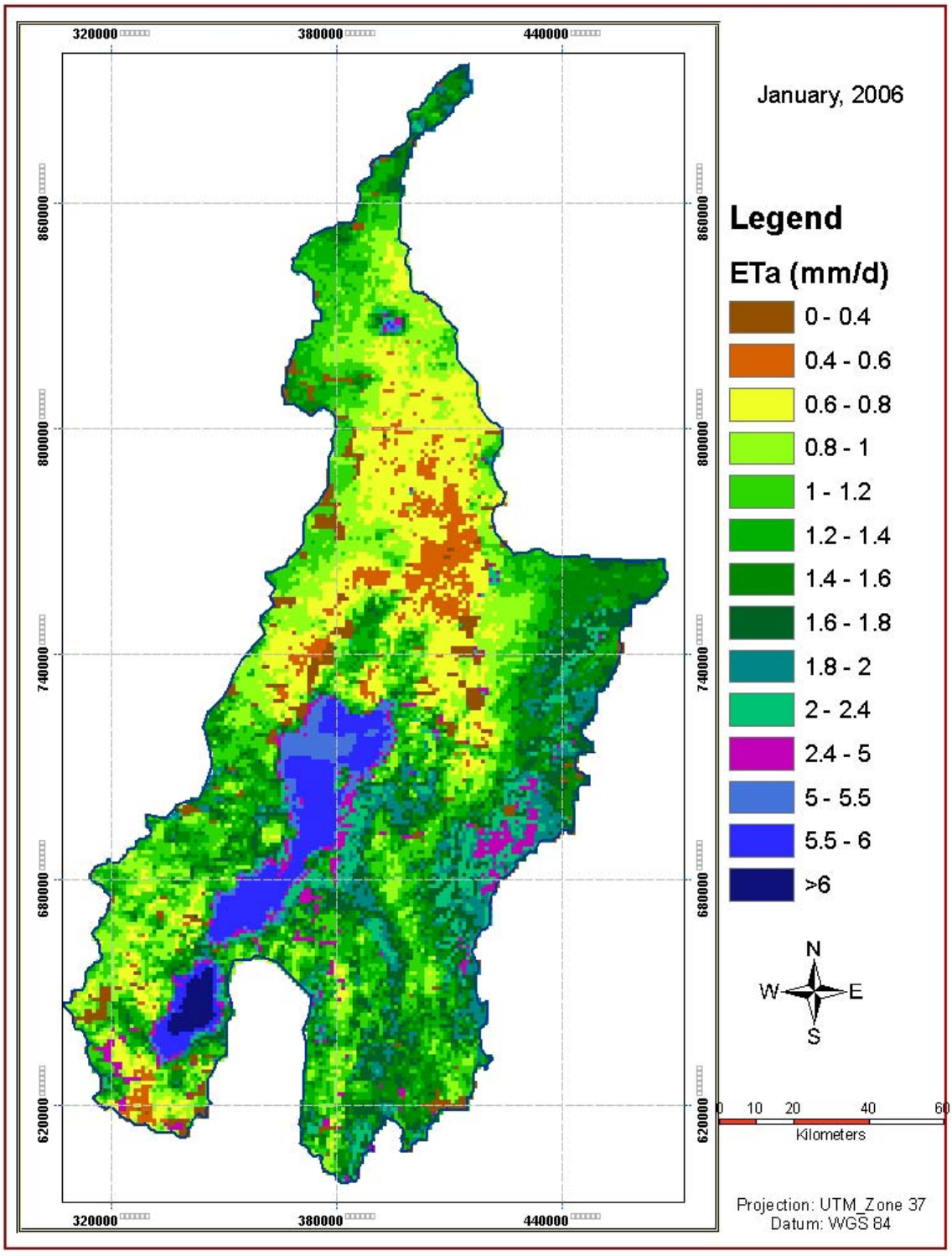

Figure 5.17 Map of daily evapotranspiration in the study area, 30 January, 2006.

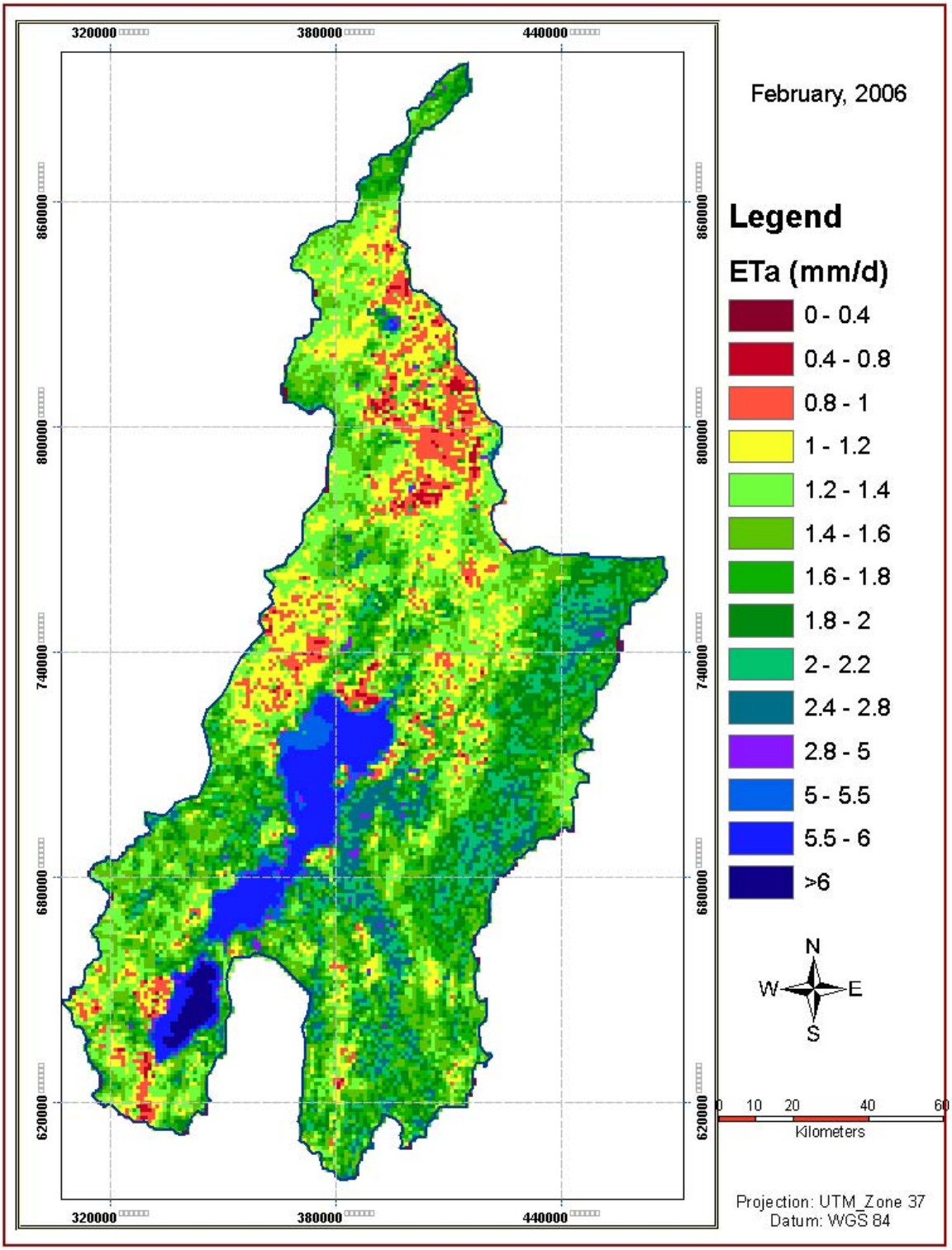

Figure 5.18 Map of daily evapotranspiration in the study area, 02 February, 2006.

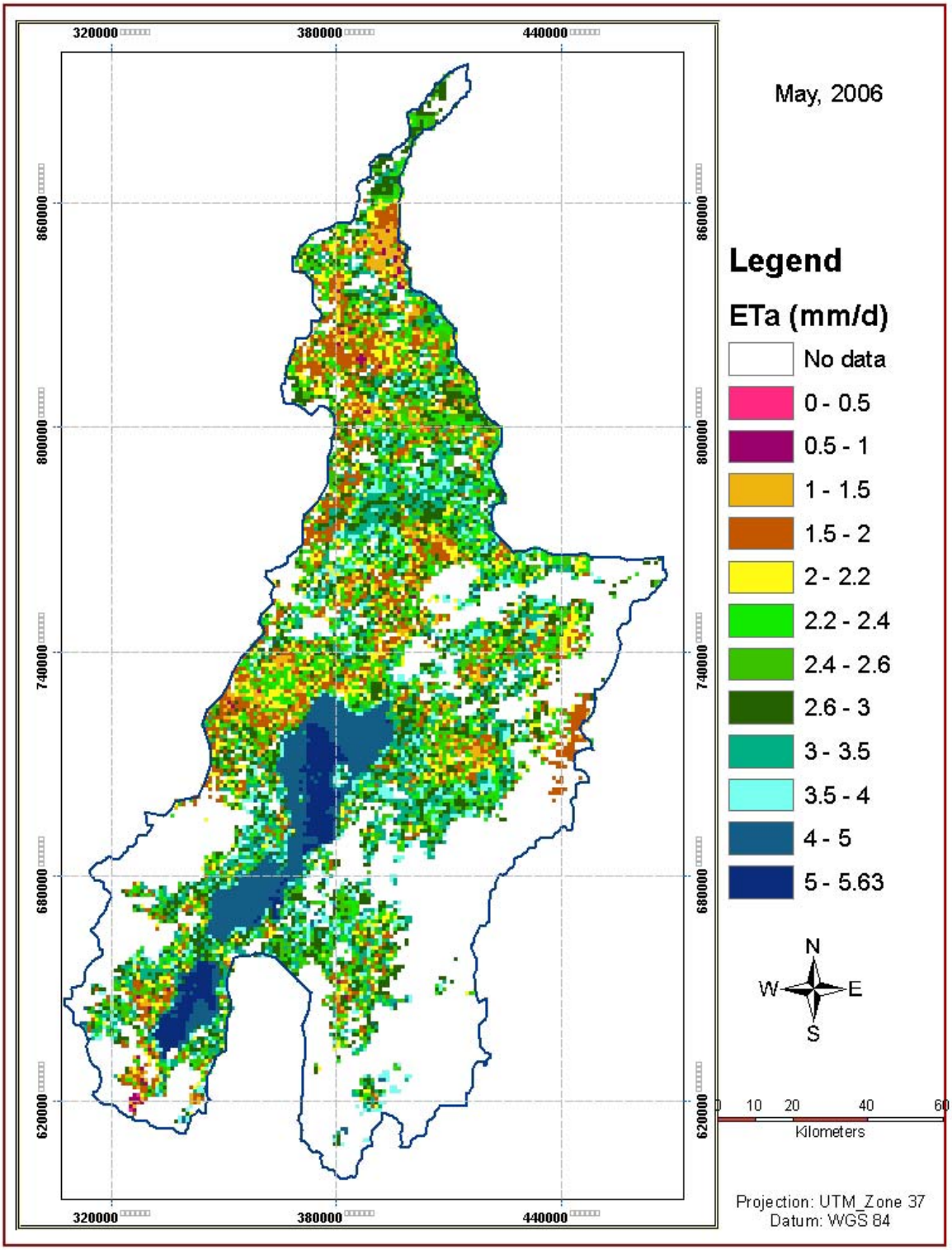

Figure 5.19 Map of daily evapotranspiration in the study area, 01 May, 2006.

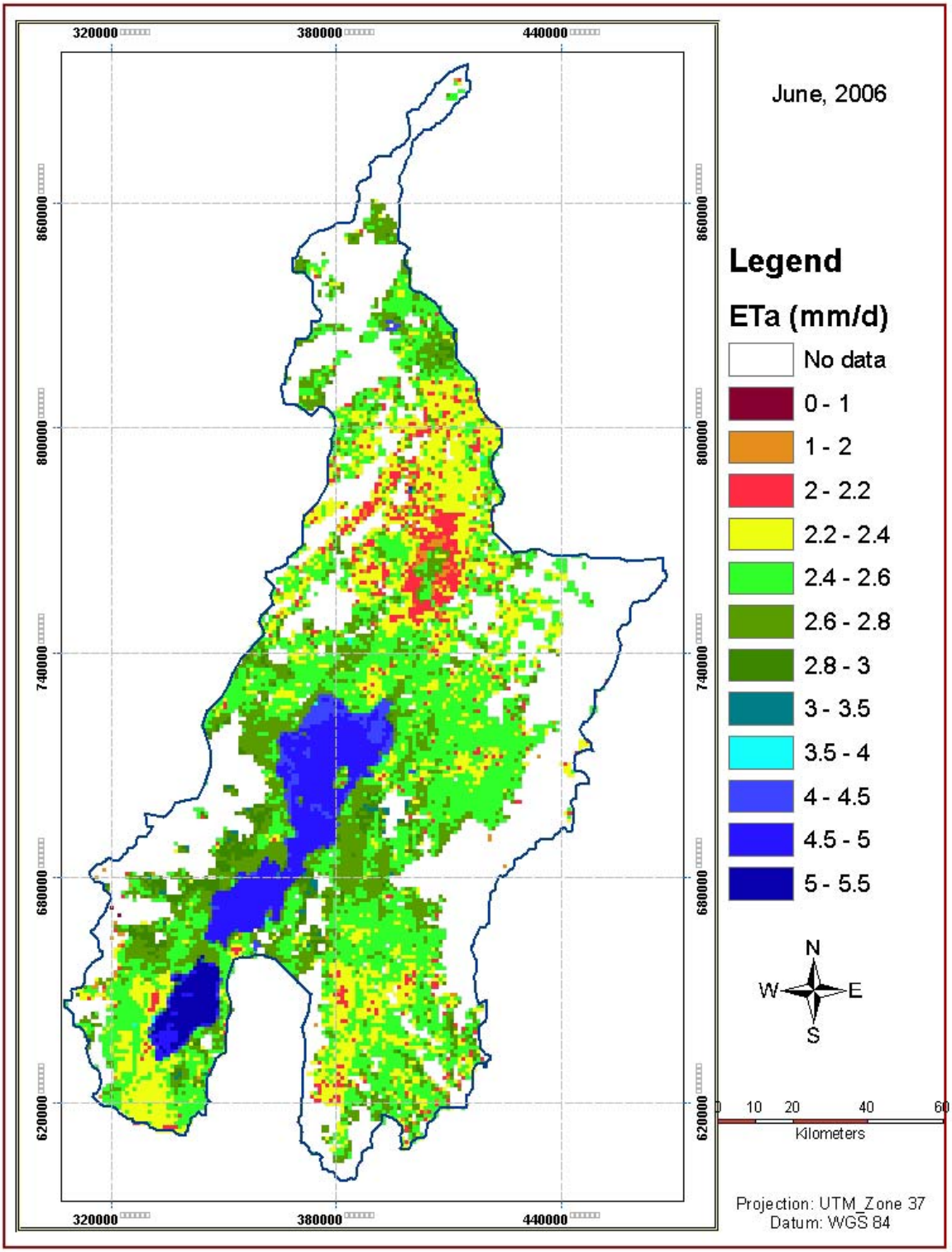

Figure 5.20 Map of daily evapotranspiration in the study area, 18 June, 2006.

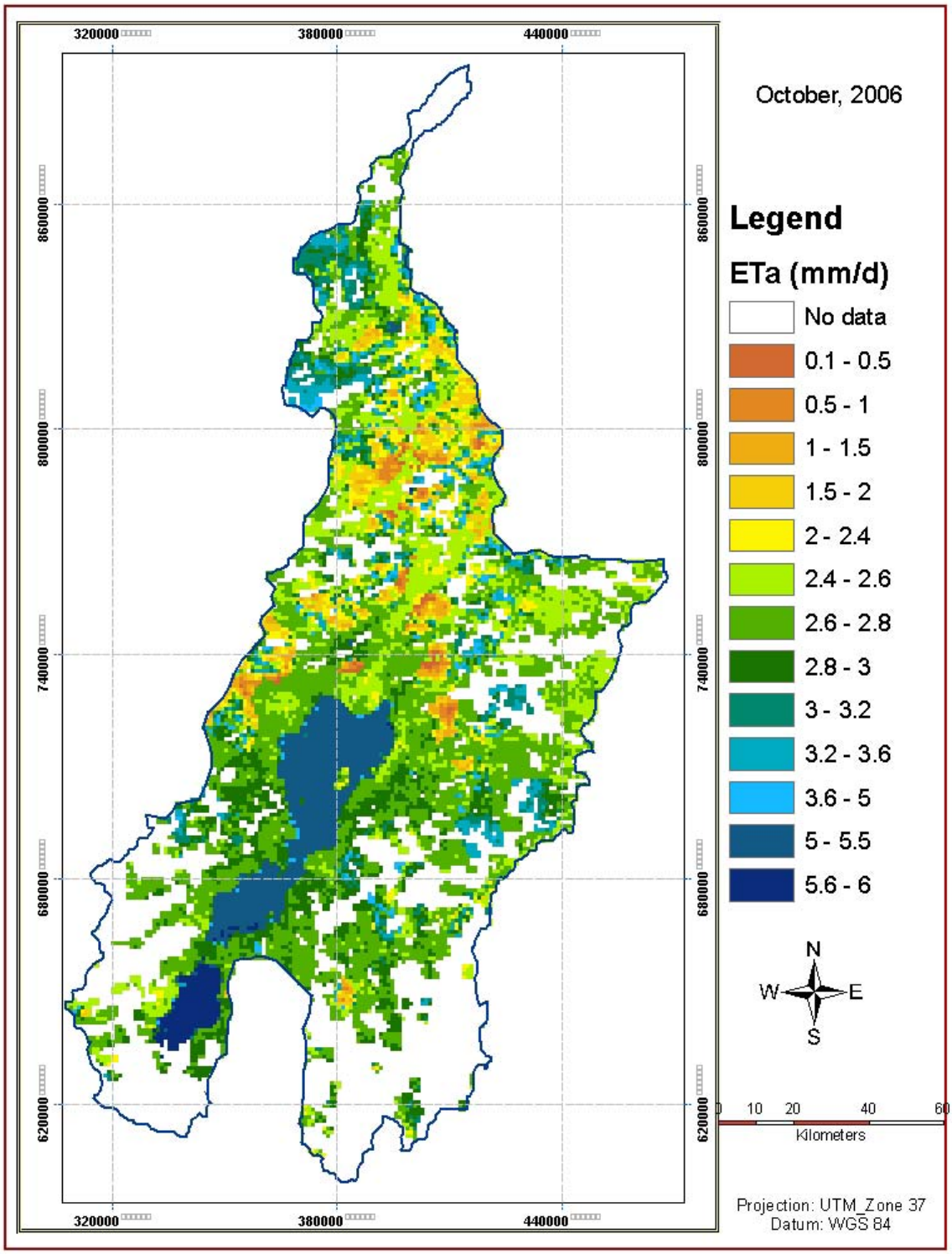

Figure 5.21 Map of daily evapotranspiration in the study area, 31 October, 2006.

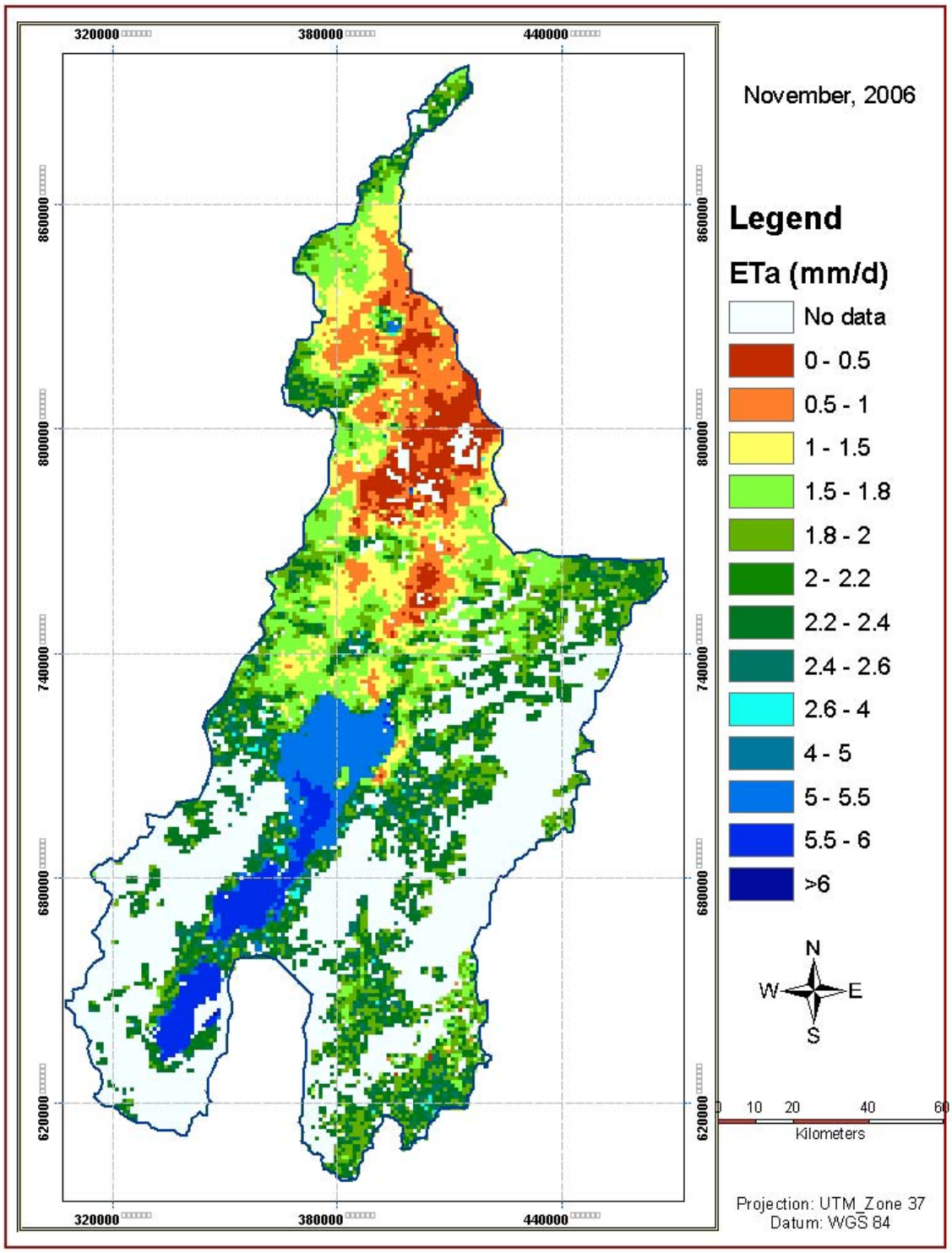

Figure 5.22 Map of daily evapotranspiration in the study area, 30 November, 2006.

6 Validation of SEBAL model for estimating Evapotranspiration rate in the study area

Many attempts have been made to evaluate the performance of SEBAL model based daily evaporation estimate against actual measurements of evaporation rate from different region with varying hydrological and metrological characteristics (Example, Bastiaanssen et al. 1988b and reference therein). The results generally show the usefulness of the method particularly in areas where detailed metrological records are lacking.
In this study, SEBAL results are compared with actual ETa estimated from water balance model to assess the plausibility of the results.

6.1 Monthly water balance

A monthly water balance has been computed for Bilate and Gidabo sub-basins, having different metrological characteristics so as to assess the plausibility of SEBAL model results. The sub-basins belong to different physiographic region, where most part of Bilate sub-basin lies in the rift floor, while Gidabo is in the highland and escarpment.

For a watershed where surface and ground water divides coincides, the water balance can be estimated by the following equation:

$$P = ET_a + Ro \pm \Delta S \qquad 6\text{-}1$$

Where P is precipitation, ETa is actual evapotranspiration and ΔS is change in storage. On a monthly basis, the difference between total monthly rainfall and runoff equals loss: change in storage plus evaporation (Shaw, 1994). In the months that potential evapotranspiration exceeds loss, the overall loss is due to evapotranspiration, whereas when PET is less than loss, there is extra loss from storage. This situation for a given catchment can be assessed by plotting monthly precipitation, potential evapotranspiration and loss together (Shaw 1994). Mean monthly rainfall and discharge data were used to compute water balance equation. In the following section how ETa was estimated through water balance equation using measured runoff data is described.

Monthly SEBAL ETa values can be computed from daily values based on the following relation (Allen et al., 2001)

$$\left[\frac{ETa}{PET}\right]_{daily} = \left[\frac{ETa}{PET}\right]_{monthly} \quad (6.2)$$

6.1.1 Bilate sub-basin

The sub-basin has a catchment area of 5518 sq.Km. Hydrological data have been recorded on a gauge posted at Bilate Tena. Figure 6-1 presents monthly water balance condition of the catchment.

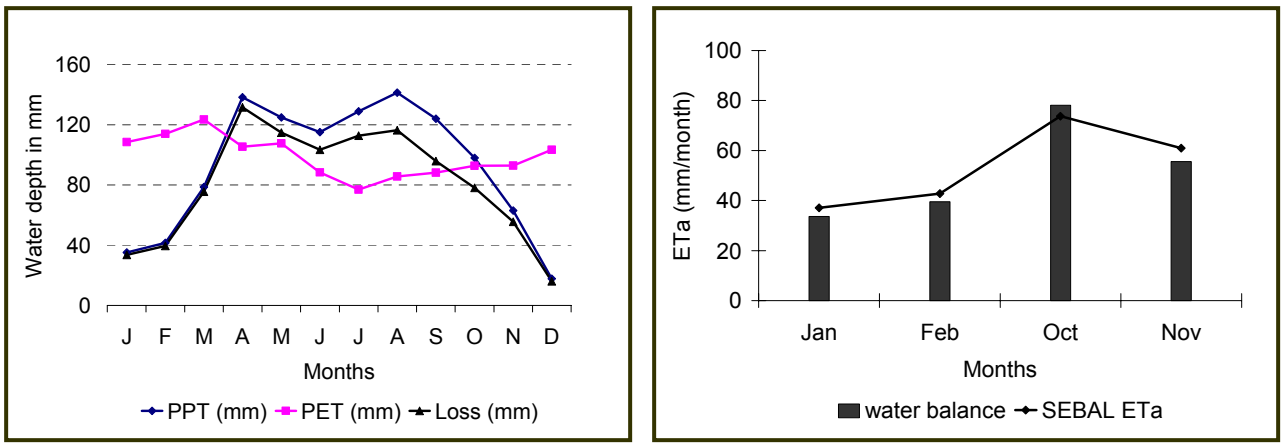

Figure 6.1 a) water balance component b) comparison between SEBAL and water balance ETa

As shown in the figure, in the months of January, February and November the losses are only due to evaporation. Therefore, ETa can be estimated by subtracting monthly measured runoff from monthly total precipitation. The water balance of the sub-basin is shown in Table 6.1.

Table 6.1 water balance of Bilate sub-basin

Month	Pt. (mm)	Measured Runoff(mm)	Water balance ETa	SEBAL ETa (mm)
JAN.	35.13	1.50	33.6	37.1
FEB.	41.52	2.00	39.5	42.8
OCT.	98	19.9	78.1	73.7
NOV.	62.9	7.70	55.6	61.0

Water balance ETa values in January, February and November are 90.5%, 92.3% and 91.2% of SEBAL results, which are about 10% below (fig 6.1b). Where as in October SEBAL ETa is about 94.6% of water balance ETa i.e water balance ETa is about 5% above. The deviation may be due to the water balance over simplification in the study area where recharge is highly controlled by structures (fracture systems). In general it is possible to say ETa is reasonably modeled by SEBAL.

6.1.2 Gidabo water balance

The streams of Gedabo catchment start from Wondo highland. The drainage area up-stream of gauging station at Aposto is 646 km^2. The mean monthly discharge values at this station are given in App. 6.2.

In the months January, February and November where potential evapotranspiration exceeds water loss (fig. 6-2), monthly runoff can be found by subtracting actual evapotranspiration from monthly rainfall total and the values are shown in table 6.2. But in the months of May, June and October potential evapotranspiration is less than loss. Therefore loss (rainfall-runoff) is equal to actual evapotranspiration plus change in storage.

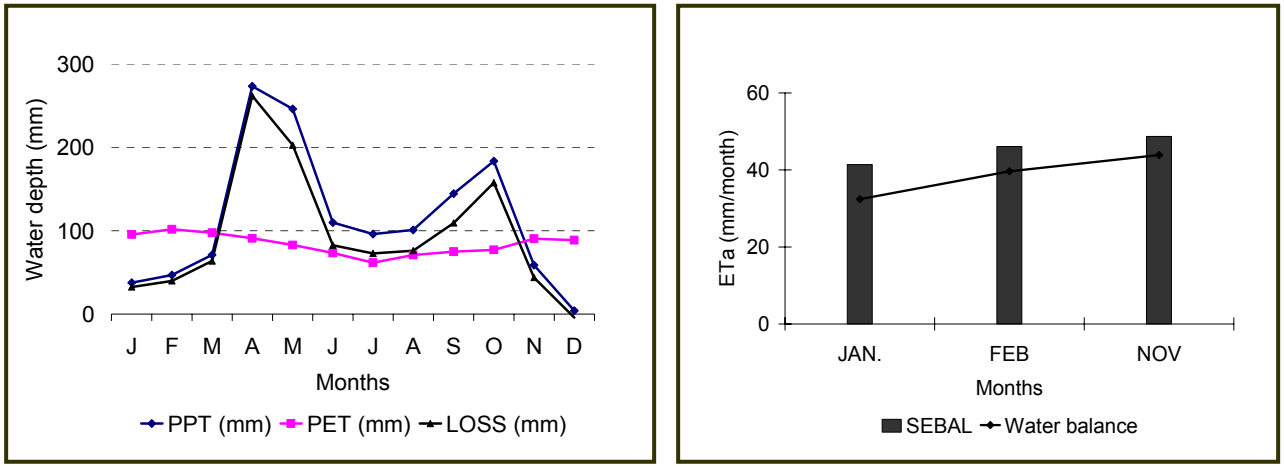

Figure 6.2 a) water balance components b) comparison between SEBAL and water balance ETa.

Table 6.2 Water balance of Gidabo sub-basin.

Month	Pt. (mm)	Measured Runoff mm)	Water balance ETa	SEBAL ETa (mm)
JAN.	37.6	5.23	32.4	41.4
FEB.	46.8	7.15	39.65	46.1
NOV.	58.6	14.70	43.9	48.7

As shown in table 6.2 and Figure 6.2 SEBAL ETa is 21%, 14% and 10% higher than water balance ETa in January, February and November, respectively. The difference between SEBAL and water balance ETa became high in precipitation low months. The agreement between SEBAL modeled and water balance ETa would become reasonable in wet season. Higher difference in the dry seasons may be due to the diversion in weir and irrigation practice which are not well represented in water balance model that resulted in moisture availability for evaporation during dry seasons. Besides comparison between image and other evapotranspiration is complicated due to difference in spatial and temporal averaging. Water balance ETa determined based on measurement record point values where as image record parameters integrated over a much large area.

6.2 Thornthwaite soil Water-balance Model

Thornthwaite water-balance model computes actual evapotranspiration over basin from monthly values of water input (precipitation), P, and potential evapotranspiration, PET (Thornthwaite and Mather, 1955). PET was obtained using combined or Penmen formula (App 6.3). Soil water field capacity was determined by overlapping soil and land use/cover map. The value for each soil and land use overlap was assigned (app. 6.4) and converted to raster. Mean value of the raster which is 135 mm was used as soil water field capacity.

This model determines actual evapotranspiration from monthly precipitation and PET using the formula below.

$$ET_a = PET \quad \text{If P>PET} \tag{6.3}$$

$$ET_a = P + S_{m-1} - S_m \quad \text{If P<PET} \tag{6.4}$$

Where S_m is soil moisture at the end of month m (m=1,2,3…..,12), which is given by:

$$S_m = S_{\max} \quad \text{If P>PET} \tag{6.5}$$

$$S_m = S_{m-1} \exp\left[-\frac{PET - P}{S_{\max}}\right] \quad \text{If P<PET} \tag{6.6}$$

Using Thornthwaite and Mather (1955) water balance model, actual evapotranspiration of the basin was computed and value for Bilate sub-basin is presented in table 6.3.

The soil water balance estimate surface runoff and soil recharge using the following equation;

$$P = ET_a + R_g + Ro \pm \Delta S \quad \text{In (mm)} \qquad 6\text{-}7$$

Where P = precipitation, ETa = actual evapotranspiration, R_g= recharge, Ro= surface runoff and ΔS= change in soil moisture.

The result revealed that actual evapotranspiration was equal to potential evapotranspiration during wet months (P>PE) between April and October. At the end of the dry season, in April, precipitation began to replenish the soil moisture i.e soil moisture recharge occurred. This process continued until the soil became at field capacity, up to June. At the end of June the soil is within 30.6 mm of being at its field capacity. Therefore, only 30.6 millimeters of the 52 mm available in July is put in the soil and the remainder runs off as surplus (Table 6.3). This continued until October and surplus runoff increase stream discharge during the period between July and October (fig. 6.4).

Table 6.3 Thornthwaite type water balance for the Bilate sub-basin.

	Jan.	Feb	Mar	Apr	May	Jun	Jul	Aug	Sep	Oct	Nov	Dec
P	35.13	41.52	78.6	138.2	124.8	115	128.9	141.3	124	98	62.9	17.7
PE	108.4	114	123.5	105.4	93.6	82.3	76.9	85.7	88.2	90.7	92.9	105.4
P-PE	-73.3	-72.5	-44.9	32.8	31.2	32.7	52	55.6	35.8	7.3	-30	-87.7
S	32.8	19.2	13.8	46.6	77.8	110.5	135	135	135	135	108	56.5
ΔS	-23.7	-13.6	-5.4	32.8	31.5	32.7	24.5	0.0	0.0	0.0	-27	-51.5
ETa	58.7	55.1	84	105.4	93.6	82.3	76.9	85.7	88.2	90.7	89.9	69.2
Sup.	0	0	0	0	0	0	27.5	55.6	35.8	7.3	0	0
R_g	0	0	0	32.8	31.2	32.7	0	0	0	0	0	0

The comparison between Thornthwaite water balance and SEBAL results show SEBAL simulate actual evapotranspiration as 37%, 22%, 17%, 18% and 32% below water balance results in January, February, May, June & October and November, respectively (table 6.4). Simplification that exist in the model that describes recharge and channel loss may be the cause of discrepancies between soil water balance ETa and SEBAL ETa in the study area where recharge is highly influenced by fracture system and when there is no well developed soil. This lead to overestimation of ETa by Thornthwaite water balance model.

Table 6.4 Mean SEBAL and soil water balance ETa

	JAN	FEB	MAY	JUN	OCT	NOV
SEBAL	41.4	42.8	77	65.7	73	58.6
Water bal	58.7	55.1	93.6	82.3	90.7	89.7

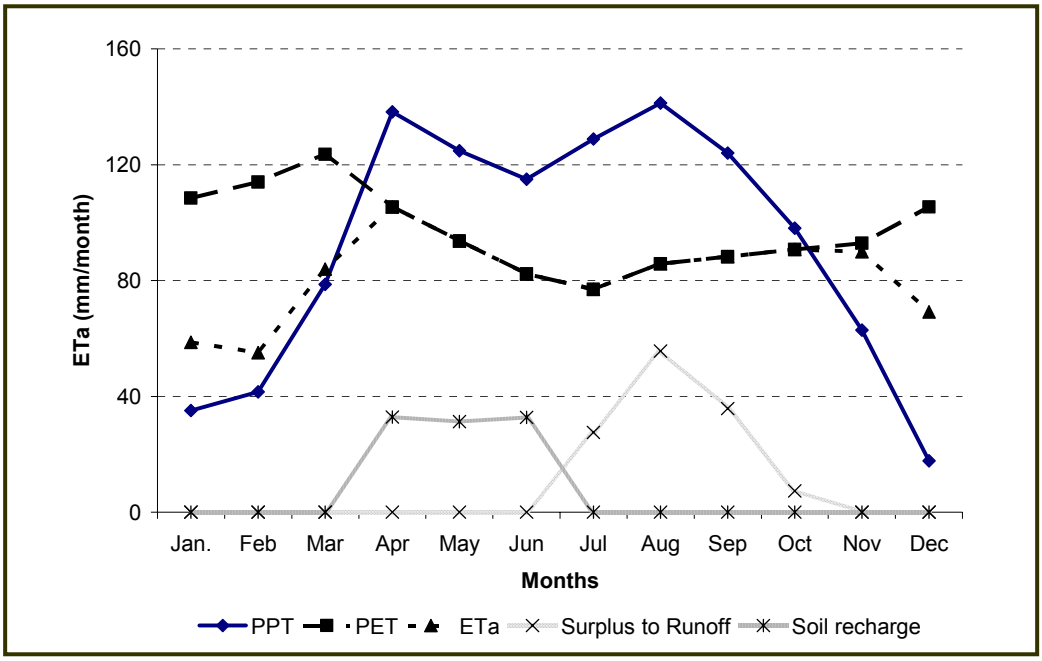

Figure 6.3. Soil water balance components of Bilate sub-basin.

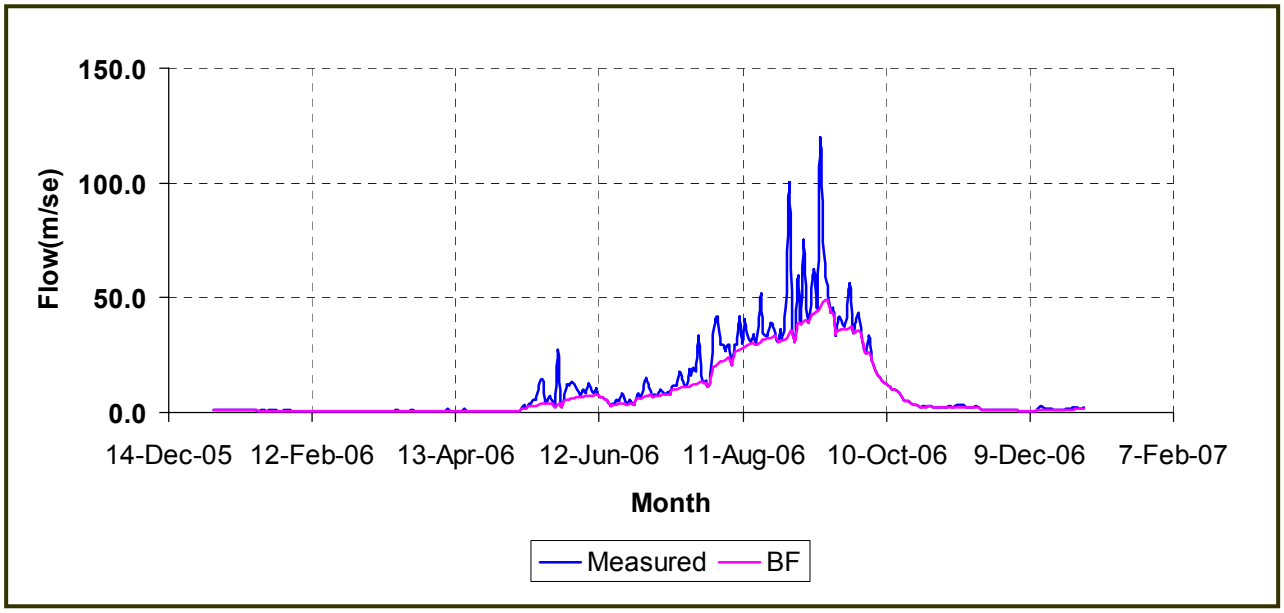

Figure 6.4. Stream hydrograph of Bilate river at Bilate Tena.

7 Conclusion

The main objective of this study is to use SEBAL model for assessment, evaluation and analysis of spatial and temporal distribution of daily actual evapotranspiration of lake Abaya-Chamo basin with an area of 18,500 km2. A total of six daily actual evapotranspiration maps for the year 2006 have been created using SEBAL algorithm and MODIS images. Estimated evaporation rate were validated by ETa estimated from river discharge measurement and obtained from soil water balance models of selected sub-basins. The result showed fairly good agreement between ETa from river discharge measurements. But significant difference exists between ETa from soil water balance and SEBAL model.

Actual evapotranspiration showed high spatial variability in the dry winter and spring days. spatial variability in summer and autumn day's was low. The high spatial variability in the ETa was mainly linked to high spatial variability in rainfall distribution and associated soil moisture saturation. An increase of precipitation in autumn (May) and summer (June) resulted in recharge of soil water across the entire basin, there by reducing the spatial variability in ETa.

The following conclusion can be drawn from the study:

- The analysis of actual evapotranspiration from land surface and lake water estimated by remote sensing method revealed large spatial and temporal variability in the area. The spatial variability of the ETa during different season closely followed the variability in soil moisture (wetness and dryness) and land use characteristics.

- Evaporative fraction (parameter determines energy partioning) in the land surface, exhibits similar regional distribution patterns as evaporation rate in the basin. For dry seasons, the average evaporative fraction did not exceed 0.4, highlighting the dominance of sensible heat flux across the basin, and the corresponding rise in observed surface temperatures where as in wet season the EF reached a maximum value of 0.78.

- The spatially distributed SEBAL ETa can be used to set water budgets for hydrological modeling, to support water planning, to estimate aquifer depletion and to support ground water modeling.

The result of this study generally demonstrates that SEBAL could be used to provide information on evaporative loss and moisture condition of a given

watershed/catchment/basin. It can be considered as operational and feasible methods to predict actual ET and improve water management and modeling processes in the study area. But should be tested with results of field measurements in different environments. The integration of remote sensing techniques and distributed hydrological modeling can produce better results. Evaporation loss and moisture condition derived from SEBAL model can be important data input for distributed hydrological modeling and to improve their performance. Therefore hydrological modeling using SEBAL result helps to assess effects of land use/cover changes on ground water recharge and runoff in the study area.

References

Allen, R. G., Pruitt, W. O., and Jensen, M. E., 1991. Environmental requirements of Lysimeter.Proc., Lysimeters for evapotranspiration and environmental measurements, ASCE, New York, 170-181.

Allen, R. G., Pereira, L. S., Raes, D., and Smith, M., 1998. Crop evapotranspiration, guidelines for computing crop water requirement. *FAO Irregation and Drainage paper 56*, Food and Agriculture Organization of the United Nation (FAO), Rome.

Arnold, J. G., R. Srinivasan, R. S. Muttiah, and J. R. Williams., 1998. Large area hydrologic modeling and assessment part I: Model development. J. American Water Resour. Assoc. 34(1), 73-89.

Bastiaanssen W.G.M, Menenti M, Feddes RA, Holtslag AA., 1998a. A remote sensing surface energy balance algorithm for land (SEBAL). *Int Journal of hydrology, 212-213.*

Bastiaanssen W.G.M, Pelgrum H, Wang J, Ma Y, Moreno JF, Roerink GJ, Van der Wal T., 1998b. A remote sensing surface energy balance algorithm for land (SEBAL). II Validation, *Int. Journal of Hydrology, 213-229.*

Bastiaanssen W.G.M., 2000. SEBAL-based sensible and latent heat fluxes in the irrigated Gediz Basin, Turkey, *Journal of Hydrology*, 229, 87-100.

Bastiaanssen W.G.M. et al., 2005. SEBAL for spatially distributed ET under actual management and growing conditions, *ASCE J. of Irrigation and Drainage Engineering* 131(1), 85-93.

Carlson, T. N., W. J. Capehart, R. R. Gillies., 1995. A new look at the simplified method for remote sensing of evapotranspiration. Rem. Sens. Environ. 54, 161-167.

Chow V.T., Maidment, D.R., and Mays, L. W., 1988. Applied Hydrology, McGraw-Hill, USA.

Dagnachew, L., Vallet-Coulomb, C., Gasse, F., 2003. Hydrological response of a catchment to climate and land use changes in Tropical Africa: case study South Central Ethiopia. *Journal of Hydrology*, 275, 67-85.

Daniel G., 1977. Aspect of Climate and Water Budget in Ethiopia, Tech. memo., AAU press.

De Bruin, H. A. R., 1987. From Penman to Makkink. In: Hooghart, J. C. (eds.), Proc. and info: TNO committee on hydrological research, vol. 39. Gravenhage, The Netherlands, p. 5-31.

Elizabet K., Zenabu G.M., Ahlgren, I., 1994. The Ethiopian Rift Valley Lakes: Chemical characteristics of Salinity-Alkalinity Series. Hydrobiolofica 288: 1-12. Kluver Academic Publishers, Belgium.

Ethiopia Mapping Authority (EMA)., 1984. National Atlas of Ethiopia, 1st ed., EMA, Addis Ababa.

FAO (Food and Agricultural Organization)., 1996. Soil and Terrain database of East Africa. Version 1.0033, October 1996. FAO, Rome.

Farah, H. O., and Bastiaanssen, W. G. M., 2001. Spatial variation of surface parameters and related evaporation in the lake Naivasha Basin estimated from remote sensing measurements. *Hydrol. Process.,* 15(9), 1585-1607.

Friedle, M.A. and F.W. Davis, 1994. Source of variation in radiometric surface temperature over a tallgrass praire. Rem. Sens. Environ. 48, 1-17.

Gorte, B. G. H., 2000. Land use and catchment characteristics. In: Schultz, G. A., and Engman, E. T. (eds.). Remote Sensing in Hydrology and Water Management, Springer, Berlin, 134-156.

Gurney, R. J. and D. K. Hall., 1983. Satellite derived surface energy balance estimates in the Alaskan sub-artic. J. Clim. Appl. Meteorol. 22 115-125.

Halcrow, sir Williams and Partners Ltd., 1992. Reconnaissance Master Plan for the Development the natural Resources of the Rift Valley Lakes Basin, Volume 3, ETH/88/001, FAO.

Huette, A. R., 1988. Soil-adjusted vegetation index (SAVI). Remote sensing of Environment. 25, 89-105.

Kite, G. W., and Droogers, P., 2000. Comparing evapotranspiration estimates from satellites, hydrological models and field data. *J. Hydrol*., 229(1-2), 3-18.

Kustas, W.P., L.E. Hipps and K.S. Humes., 1995. Calculation of basin-scale surface fluxes by combining remotely sensed data and atmospheric properties in a semi-arid landscape. *Boundary layer Meterorol*. 75, 105-124.

Kustas, W. P and J. M. Norman., 1996. Use of remote sensing for evapotranspiration monitoring over land surface. In : A. Rango and J. C. Ritchie (eds.). Special issue: remote sensing applications to hydrology. *Hydrological Science J*. 41(4), 495-516.

Liang, S., 2001. Narrow band to broadband conversion of land surface albedo I: Algorithm. *Remote sensing of Environments*. 76(2), 213-238.

Liang, S., J. S. Chad, et al., 2003. Narrowband to broadband conversion of land surface albedo II: Validation. Remote sensing of Environments. 84, 25-41.

Lillesand, T. M., and Kiefer, R. W., 1987. Remote sensing and image interpretation. New York: John Wiley and Son.

Maathuis, H. P., 2006. DEM based Hydro-Processing. Introduction to the tools developed, Version 1, ITC.

Maidment, D. R., 1993. Handbook of Hydrology, McGraw-Hill, USA.

Makin, M. J., Kingham, T. J., Waddams, A. E., Birchall, C. J. and Tamene Tefera., 1975. Development Prospects in the Southern rift Valley Ethiopia. Land Resources Division, Minist. Overseas Dev. No. 21.

Mendoza, M., Bocco, G., Bravo, M., 2002. Spatial prediction in hydrology: status and implication in the estimation of hydrological processes for applied research. *Progress in Physical Geography*. 26(3), 319-338.

Menenti, M., 2000. Evaporation. In: Schultz, G. A., and Engman, E. T. (eds.). Remote Sensing in Hydrology and Water Management, Springer, Berlin, 157-188.

Meneti, M., 1984. Physical aspects and determination of evapotranspiration in deserts applying remote sensing techniques. Inst. Land Water Manag. Res., Wageningen, The Netherlands. 202 pp.

Mohamed, Y., Bastiaanssen, W. G. M., and Savenije, H. H. G., 2004. Spatial variability of evaporation and moisture storage in the swamps of the upper Nile studied by remote sensing techniques. *J. Hydrol.,* 277, 116-124.

Moran, M. S. and Jackson, R. D., 1991. Assessing the spatial distribution of evapotranspiration using remotely sensed inputs. *J. Envirnm. Qual*. 20 725-737.

Morse, A., Tasumi, M., Allen R.G., Kramber, W.J., 2000. Application of the SEBAL Methodology for Estimating Consumptive Use of Water and Streamflow Depletion in the Bear River Basin of Idaho through Remote sensing, Final Report. Idaho Department of Water resource and University of Idaho, Idaho, 107pp.

Najjar, R.G. 1999. The water balance of the Susquehanna River Basin and its response to climate change. *Journal of hydrology*. 219, 7-19

Neilson, R.P., 1995. A model for predicting continental scale vegetation distribution and water balance. *Ecological Application*. 5(2), 362-385.

Nemani, R.R. and S.W. Running., 1989. Estimation of regional surface resistance to evapotranspiration from NDVI and thermal-IR AVHRR data. *J. Appl. Meteorol*. 28(4), 276-284.

Penman, H. L., 1956. Estimating evapotranspiration. Transaction of the American Geophysical Union. 37(1) 43-50.

Penman, H. L., 1947. Natural evaporation from open water, bare soil and grass. Proc. Royal Society of London, Series A. *Mathematical and Physical science,* London.

Seleshi. B. Awulachew., 2001. Investigation of water resources Aimed at Multi-Objective Development with Respect to Limited Data Situation: The Case of Abaya-Chamo Basin, Ethiopia. Ph.D thesis, Unpublished report, Institute fur Wasserbau und Technische Hydromechanik.

Sabins, F. F., 1997. Remote sensing principles and interpretation. New York: W. H. Freeman and Company.

Salomonson, V. V., 1983. Water resource assessment. In: Colwell, J., (eds.). Manual of remote sensing. Bethesda MD: *American society of photogrammetery and remote sensing.*

Shaw, E. M., 1994. Hydrology in practice. Chapman and Hall.

Schultz, G. A., and Engman, E. T., 2000. Remote Sensing in Hydrology and Water Management, Springer, Berlin, 1-14.

Tenalem, A., 1998. The hydrgeolgical system of the Lake District basin, Central Main Ethiopian Rift. International Institute for Aerospace Survey and Earth Science. Ph.d thesis. 259 pp.

Timmermans, W. J., Gieske, A. S., Kustas, W. P., Arneth, A., and Parodi, G. N., 2003. Determination of water and heat fluxes with MODIS imagery-Maun, Botswana. *Proc., Int. Symp.* SPIE USE V 16, 5232-55, SPIE, Bellingham, Wash.

Tucker, C. J., 1979. Red and Photographic Infrared Linear Combinations for Monitoring Vegetation, *Remote Sensing of Environments,* 8, 127-150.

Thorhnwaite, C. and Matter, J., 1955. The water balance, publication in climatology. Centeron NJ: Drexel Institute of Technology.

Twine, T.E., 2000. Correcting eddy covariance flux underestimate over grassland. Agric. Forest Meteorol. 103, 279-300.

Van de Griend, A. A., and M. Owe., 1992. On the relationship between thermal emissivity and the Normalized Difference Vegetation Index for natural surfaces. *Int. J. Remote Sens.,* 14, 1119-1131.

Van den Kroonenberg, A., 2003. Surface flux estimates over an over an olive yard: SEBAL Method applied to NOAA-KLM and Landsat-7. MSc thesis, Wageningen Uni., Dept. of Metrology.

Wang, J., Y., Menenti, M., Bastiaanssen, W. G M., and Mitsuta, Y., 1995. The scaling up of land surface processes over a heterogeneous landscape with satellite observation. *J. Meteorol. Soc. Jpn.,* 73(6), 1235-1244.

Appendix 1.1 Soil map of the study area.

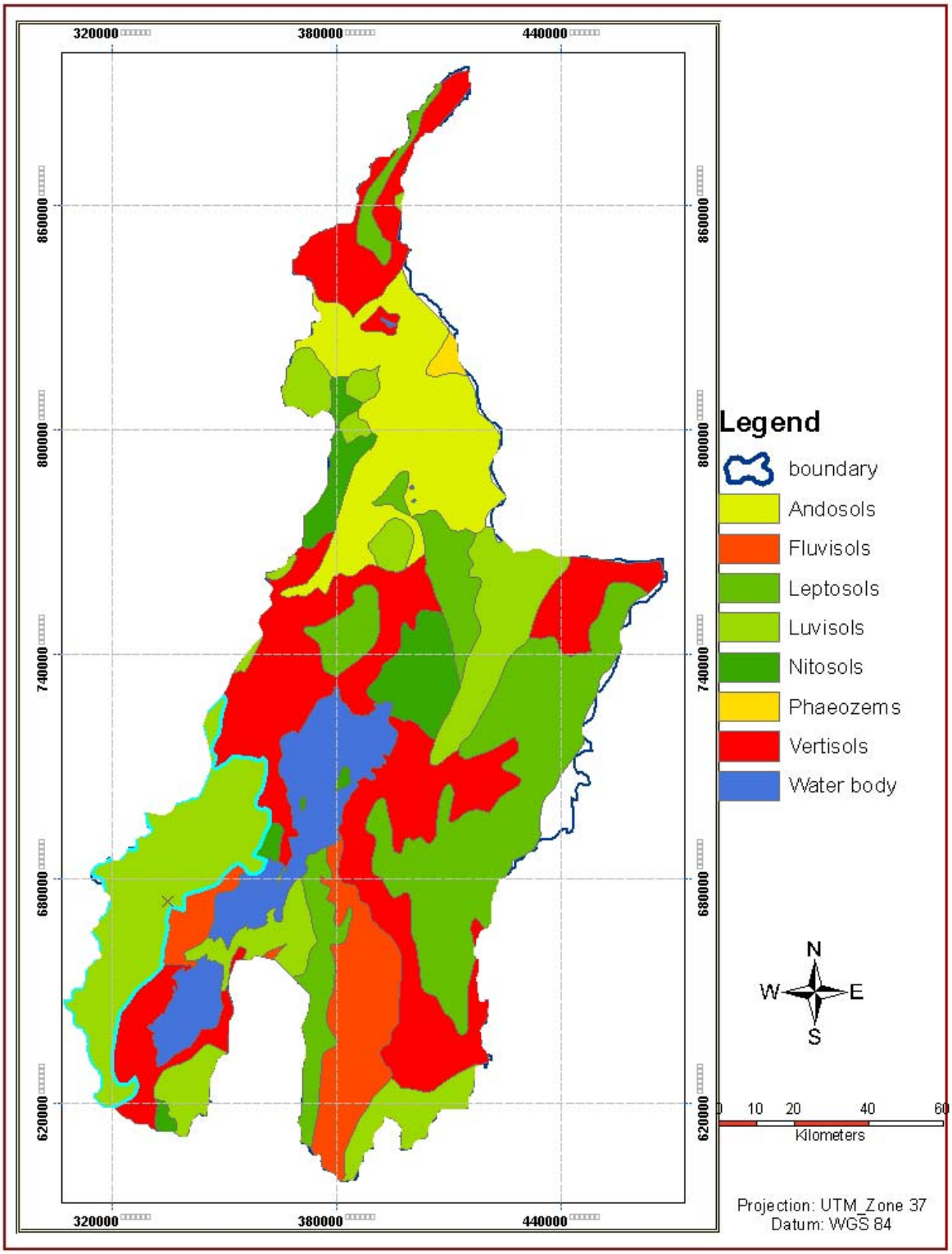

Appendix.3.1 MODIS spectral and spatial characteristics in visible and thermal bands.

Portion of EMR	Band No.	Wavelength range	Spatial resolution
Visible	1	620 – 670 nm	250 m
	2	841 – 876 nm	250 m
	3	459 – 479 nm	500 m
	4	545 – 565 nm	500 m
	5	1230 – 1250 nm	500 m
	6	1628 – 1652 nm	500 m
	7	2105 – 2155 nm	500 m
Thermal infrared	31	10.780 – 11.280 μm	1000 m
	32	11.770 – 12.270 μm	1000 m

Appendix. 3.2. Date of acquisition in 2006

Acquisition date	**Data or Products**
January 01	Surface reflectance, temperature and emissivity
February 02	Surface reflectance, temperature and emissivity
May 01	Surface reflectance, temperature and emissivity
June 18	Surface reflectance, temperature and emissivity
October 31	Surface reflectance, temperature and emissivity
November 30	Surface reflectance, temperature and emissivity

Appendix-3.3. Shows the standard MODIS land products available.

Code	**MODIS product**
MOD09	Surface reflectance
MOD11	Land surface Temperature/Emissivity
MOD12	Land Cover/Change
MOD13	Vegetation Indices
MOD14	Thermal Anomalies/Fire
MOD15	Leaf Area Index/FPAR
MOD17	Primary Production
MOD43	BRDF/Albedo
MOD44	Vegetation Continuous Field

Appendix 3.4. Metrological stations in the study area.

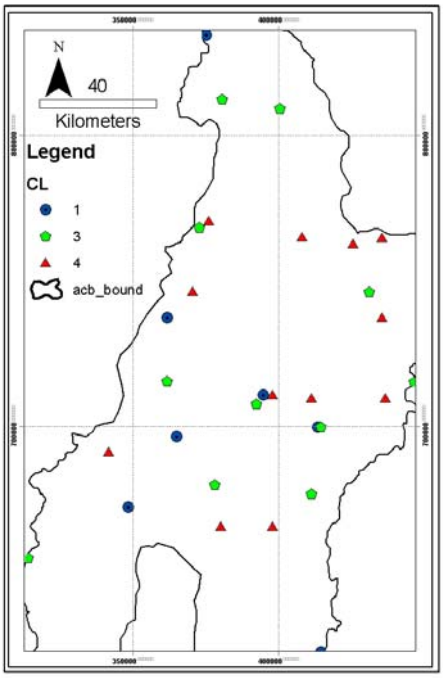

STATION	ALT	LAT	LONG
Alaba Kulito	1750	7.32	38.1
Amaro Kele	1400	6.15	37.9
Angacha	2100	7.35	37.92
Arba Minch	1290	6.08	37.63
Billate	1300	6.43	38.05
Dilla	2400	6.33	38.22
Fisha Genet	2000	6.12	38.2
Gase Chere		7.08	37.9
Gerese	2300	5.92	37.32
Hagere Mariam	1900	5.63	38.23
Hagere Selam	2840	6.47	38.52
Hosana	2200	7.55	37.87
Mirab Abaya	1280	6.3	37.78
Wajifo	1240	6.47	37.75
Yirga Chefe	1925	6.33	38.23

Appendix 3.5. Mean monthly sunshine hour from stations in the study area.

	J	F	M	A	M	J	J	A	S	O	N	D
A/Minch	9.5	9.7	8.3	8.1	6.8	6.5	4.4	6.2	6.1	7.3	9.2	10.2
Bilate	8.9	9.6	8.1	8.1	6.4	7.0	4.9	6.8	6.3	7.8	9.0	10.3
Dila	6.7	7.5	7.4	7.1	4.3	4.2	3.4	4.5	4.7	4.6	7.7	9.1
Hossana	8.2	9.9	8.0	6.9	6.2	5.8	4.2	4.9	6.1	8.7	9.3	10.6

Appendix 3.6. Mean monthly wind speed from stations in the study area.

	J	F	M	A	M	J	J	A	S	O	N	D
A/Minch	0.9	0.7	0.8	0.8	0.6	0.8	0.9	1.0	0.8	0.6	0.5	0.5
Bilate	1.4	1.4	1.0	0.9	0.6	1.0	1.1	0.9	0.7	0.7	1.0	1.7
Dila	0.6	0.7	0.7	0.7	0.4	0.4	0.5	0.5	0.4	0.4	0.4	0.5
Hossana	1.1	1.5	1.3	1.3	1.0	1.2	1.3	1.2	1.1	1.1	1.3	1.2

Appendix 3.7. Mean monthly temperature from stations in the study area.

STATION	JAN	FEB	MAR	APR	MAY	JUN	JUL	AUG	SEP	OCT	NOV	DEC
Alaba Kulito	21.15	22.5	22.7	22.15	20.75	20.3	19.5	18.85	20.55	20.3	19.85	19.7
Amaro Kele	23.6	25.1	23.9	23.05	21.25	20.7	19.5	20.9	21.05	21.75	21.85	21.9
Angacha	19.1	19.6	17.7	17.55	17.7	17.55	17.5	17	16.75	18.55	19.2	19.35
Arba Minch	24.35	26.05	26.25	25.2	22.65	23.2	22.75	24.1	23.55	23.75	23.1	22.35
Billate	24.4	25.5	25.45	25.05	22.8	22.45	21.75	22.55	22.1	22.75	22.45	22.65
Dilla	20.45	21.65	22.45	22	20.45	20	19.7	20.35	20.25	20.1	19.7	18.4
Fisha Genet	18.85	19.93	19.45	19.65	17.45	16.55	16.35	16.75	17.25	17.1	17.8	18.6
Gase Chere	18.65	18.45	18.55	18.45	17.85	17.05	16.5	16.5	16.8	17.25	16.4	17
Gerese	17.75	19.15	19.9	18.25	17.1	17.2	16.15	15.7	15.75	16.05	16.55	15.55
Hagere Mariam	18.6	19.6	19.3	19.1	17.35	16.05	15.15	15.7	16.45	16.15	15.85	16.5
Hagere Selam	13.1	14	14.5	14.5	13.6	12.45	11.6	10.65	11.6	12.9	12.35	12.3
Hosana	16.75	18.75	18.75	18.4	17.05	16.35	15.65	16.3	16.4	16.5	16.6	16
Mirab Abaya	24.85	26.1	26.1	25.6	23.25	23.5	22.95	23.95	24.1	23.85	24.15	23.5
Wajifo	22.45	22.7	22.7	23.4	21	23.7	21.85	22.75	22.55	23.45	24.35	24.7
Yirga Chefe	17.8	19.15	19.15	20.45	19.2		17.1	17.4	17.65	17.6	18.05	18.1

Appendix 3.8. Mean monthly relative humidity from station in the study area.

	J	F	M	A	M	J	J	A	S	O	N	D
Bilate	52	56.7	62.6	72.6	73.6	72.3	75.7	71.2	71.8	70.1	63	54
A/Minch	50	48.4	51.2	65.7	70	65	64.3	60	60.5	66	60	54
Dila	62.4	58	62.3	74.1	78.3	77	78.2	77.1	79.9	78.2	73.5	68.3

Appendix 3.9. Mean monthly rainfall surface generated from station measurement in 2006.

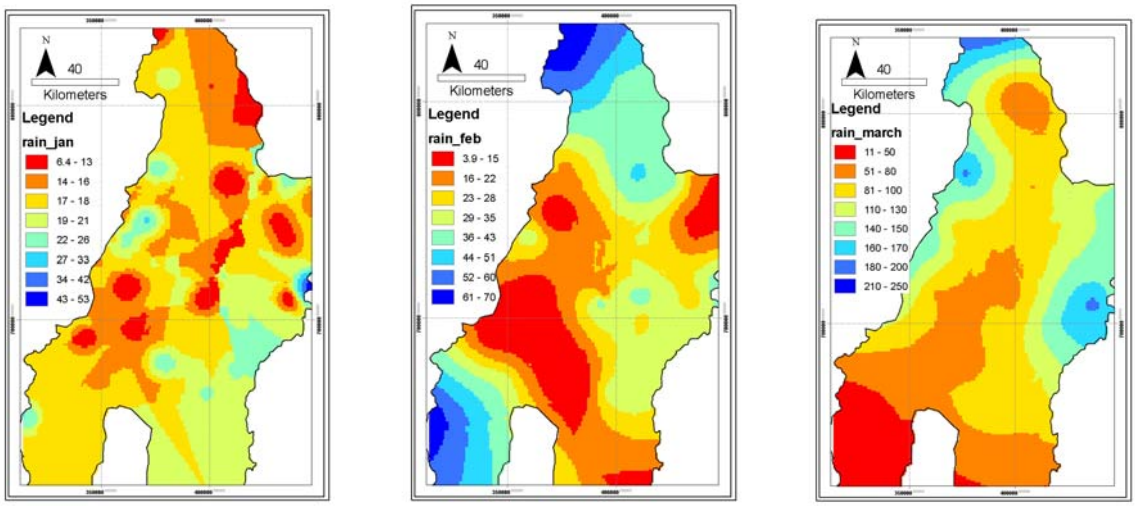

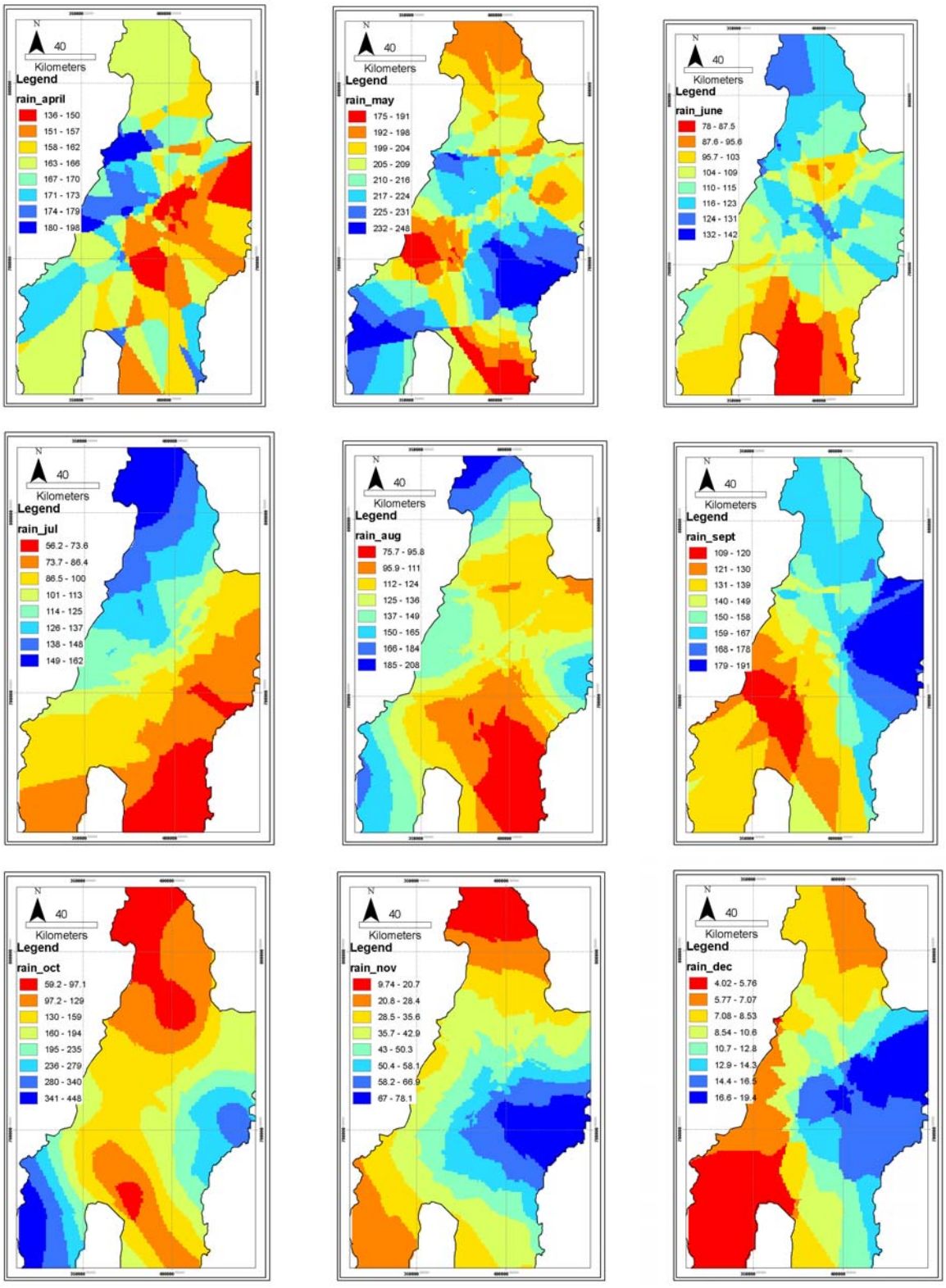
N
40
Kilometers
Legend
rain_april
136 - 150
151 - 157
158 - 162
163 - 166
167 - 170
171 - 173
174 - 179
180 - 198
N
40
Kilometers
Legend
rain_may
175 - 191
192 - 198
199 - 204
205 - 209
210 - 216
217 - 224
225 - 231
232 - 248
N
40
Kilometers
Legend
rain_june
78 - 87.5
87.6 - 95.6
95.7 - 103
104 - 109
110 - 115
116 - 123
124 - 131
132 - 142
N
40
Kilometers
Legend
rain_jul
56.2 - 73.6
73.7 - 86.4
86.5 - 100
101 - 113
114 - 125
126 - 137
138 - 148
149 - 162
N
40
Kilometers
Legend
rain_aug
75.7 - 95.8
95.9 - 111
112 - 124
125 - 136
137 - 149
150 - 165
166 - 184
185 - 208
N
40
Kilometers
Legend
rain_sept
109 - 120
121 - 130
131 - 139
140 - 149
150 - 158
159 - 167
168 - 178
179 - 191
N
40
Kilometers
Legend
rain_oct
59.2 - 97.1
97.2 - 129
130 - 159
160 - 194
195 - 235
236 - 279
280 - 340
341 - 448
N
40
Kilometers
Legend
rain_nov
9.74 - 20.7
20.8 - 28.4
28.5 - 35.6
35.7 - 42.9
43 - 50.3
50.4 - 58.1
58.2 - 66.9
67 - 78.1
N
40
Kilometers
Legend
rain_dec
4.02 - 5.76
5.77 - 7.07
7.08 - 8.53
8.54 - 10.6
10.7 - 12.8
12.9 - 14.3
14.4 - 16.5
16.6 - 19.4

Appendix 4.1. The broad band albedo derived from MODIS products acquired on individual dates of January 2006 to December 2006: a) 01 January b) 02 February c) 01 May d) 18 June e) 31 October and f) 30 November.

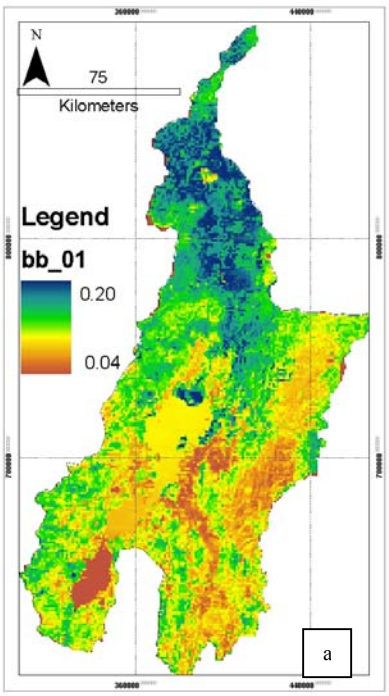

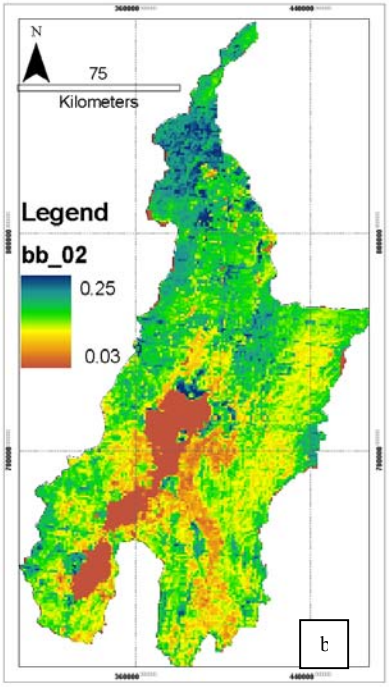

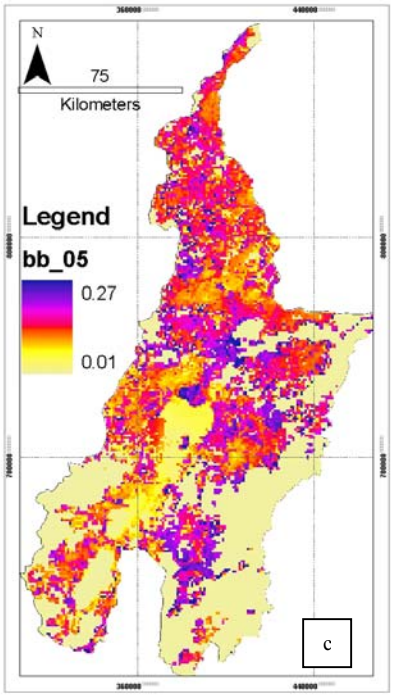

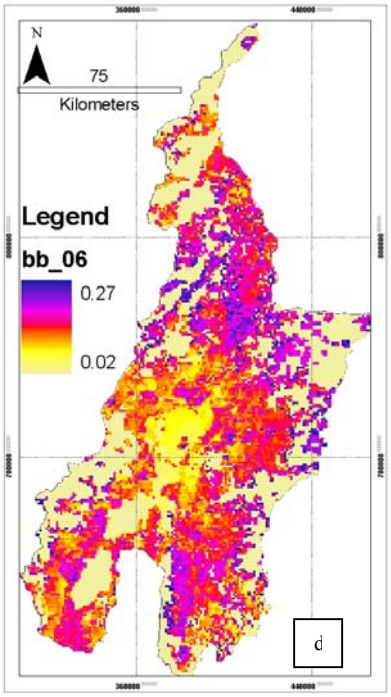

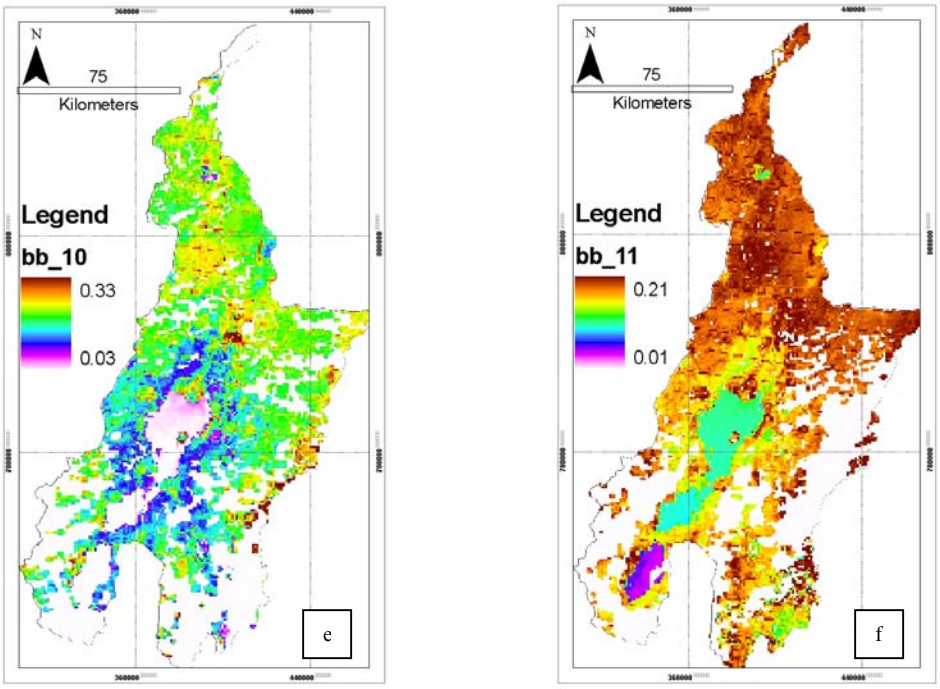

Appendix 4.2. NDVI derived from MODIS products acquired on individual dates of January 2006 to December 2006: a) 01 January b) 02 February c) 01 May d) 18 June e) 31 October and f) 30 November.

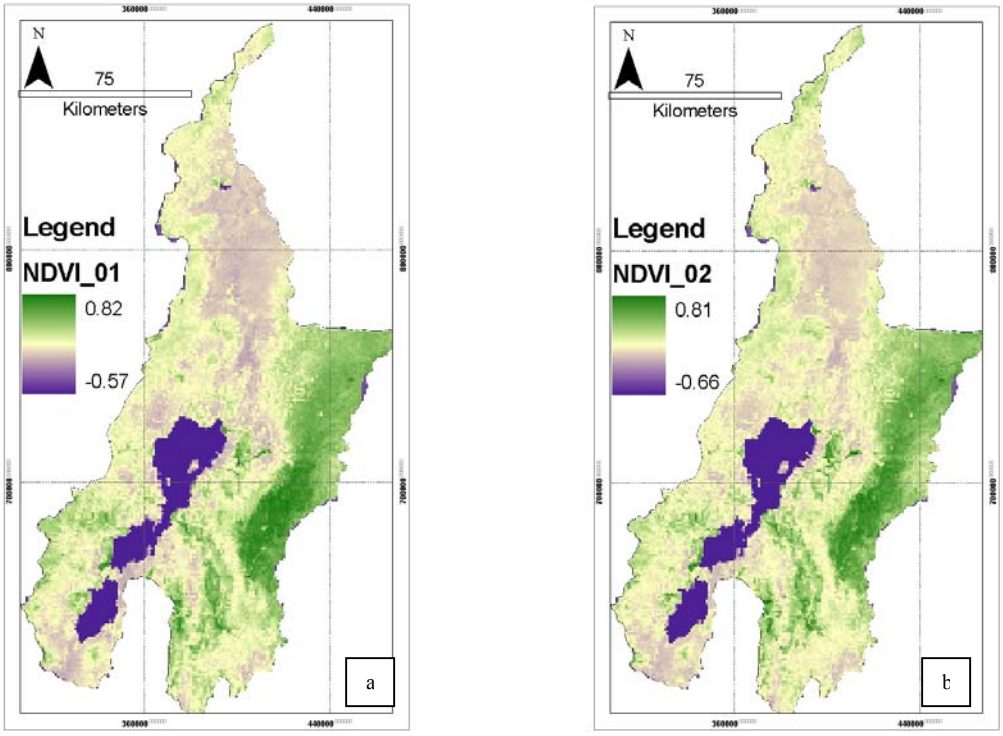

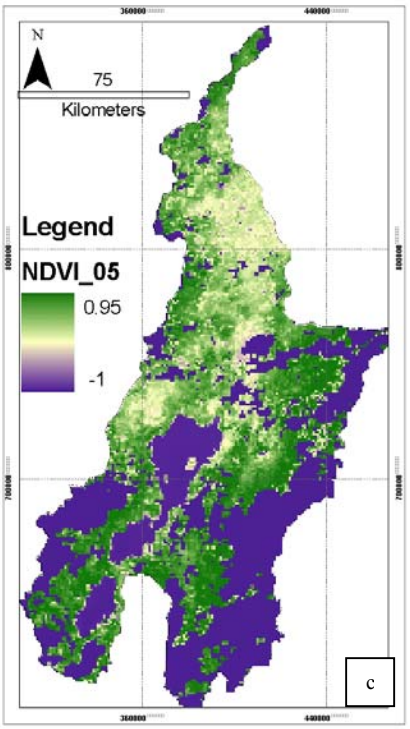
N
75
Kilometers
Legend
NDVI_05
0.95
-1
c

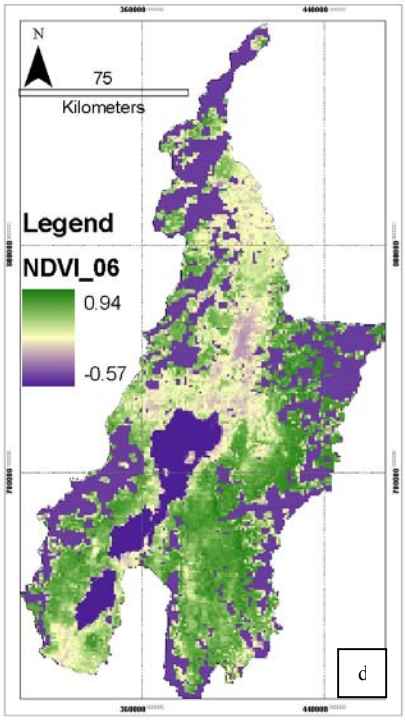
N
75
Kilometers
Legend
NDVI_06
0.94
-0.57
d

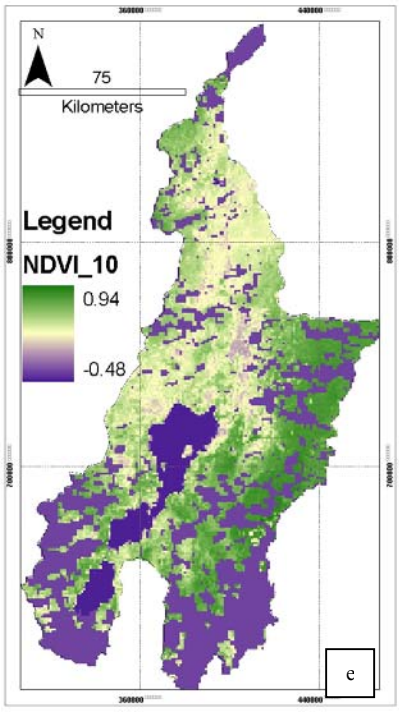
N
75
Kilometers
Legend
NDVI_10
0.94
-0.48
e

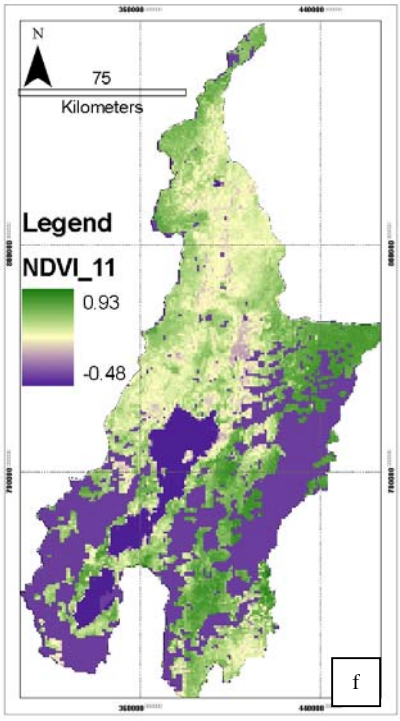
N
75
Kilometers
Legend
NDVI_11
0.93
-0.48
f

Appendix 4.3. Land surface temperature derived from MODIS products acquired on individual dates of January 2006 to December 2006: a) 01 January b) 02 February c) 01 May d) 18 June e) 31 October and f) 30 November.

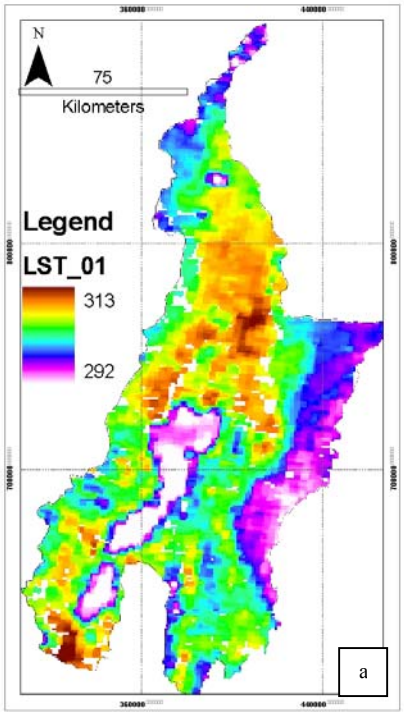

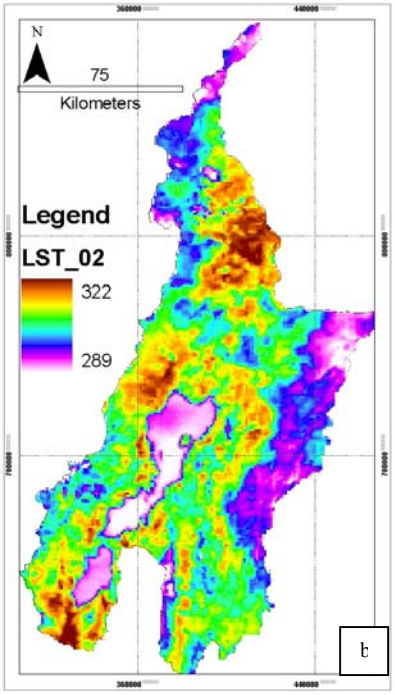

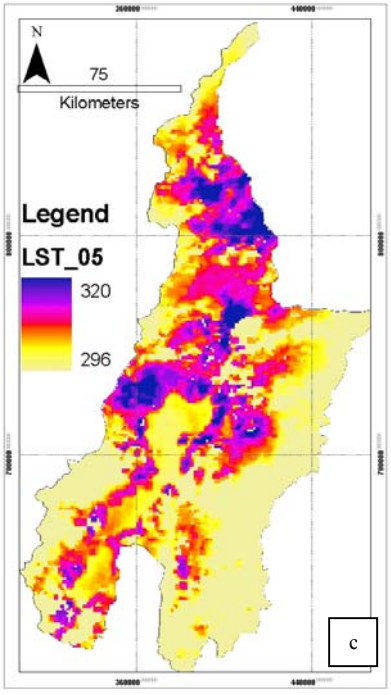

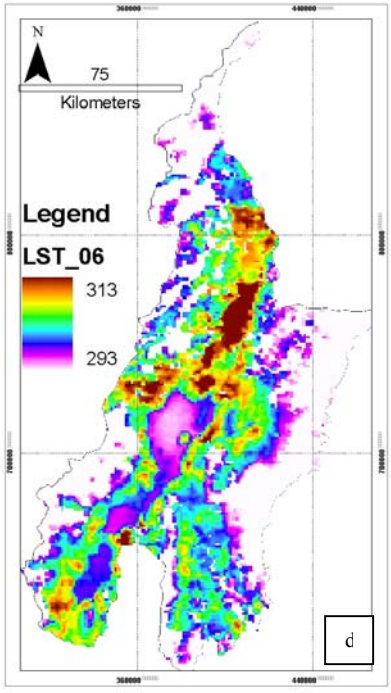

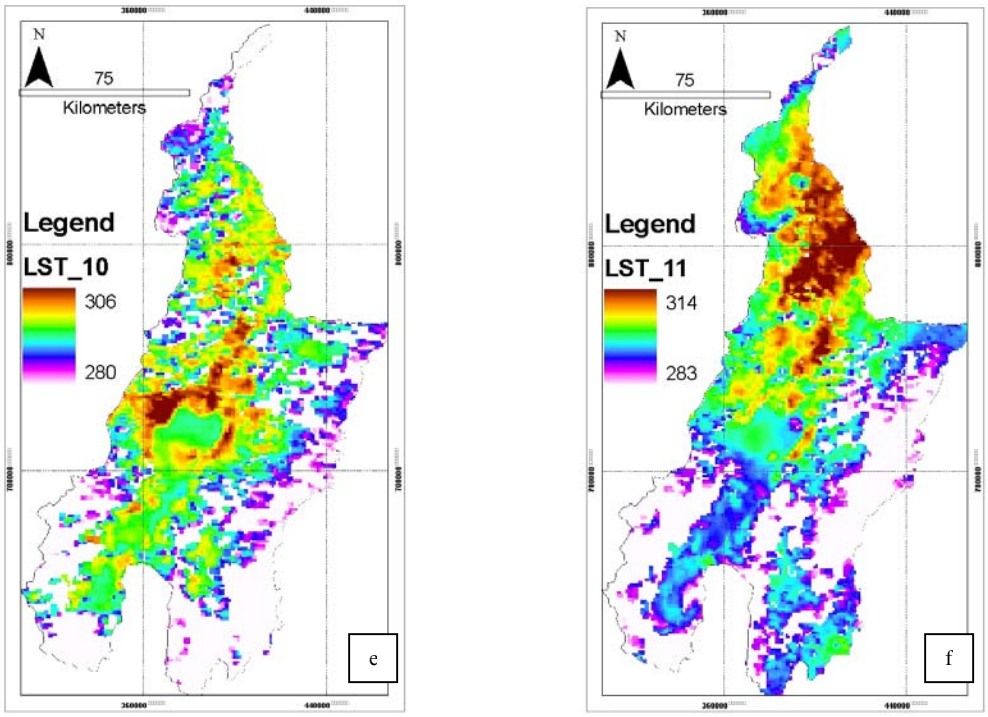

Appendix 4.4. Evaporative fraction derived from MODIS products acquired on individual dates of January 2006 to December 2006: a) 01 January b) 02 February c) 30 May d) 18 June e) 31 October and f) 30 November.

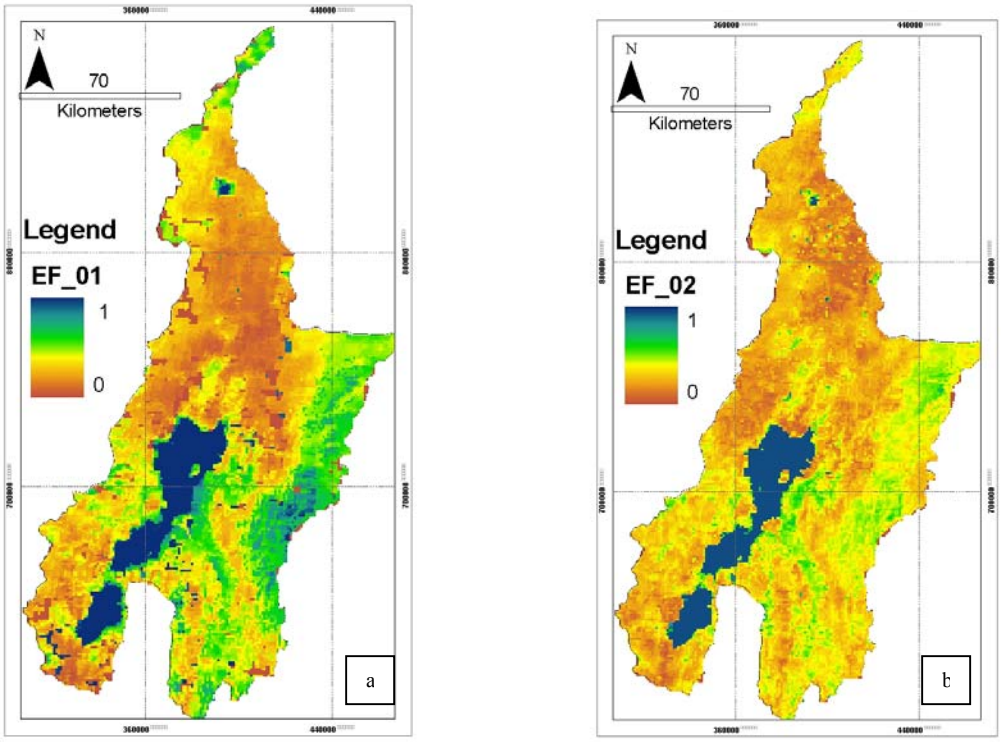

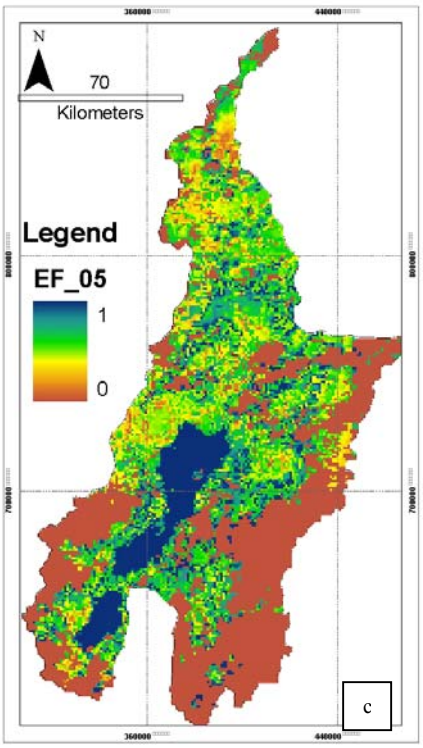
N
70
Kilometers
Legend
EF_05
1
0
c

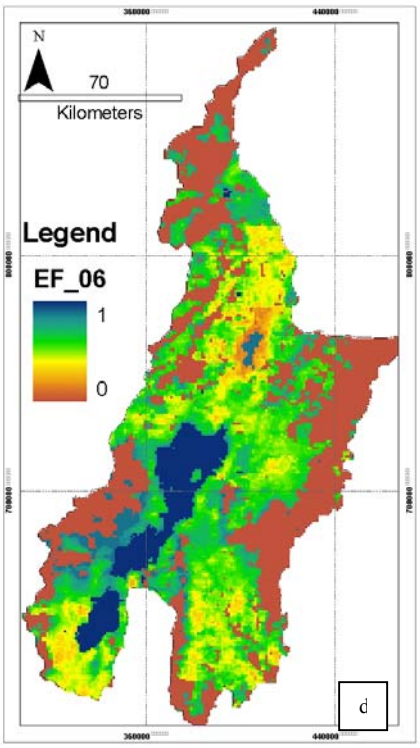
N
70
Kilometers
Legend
EF_06
1
0
d

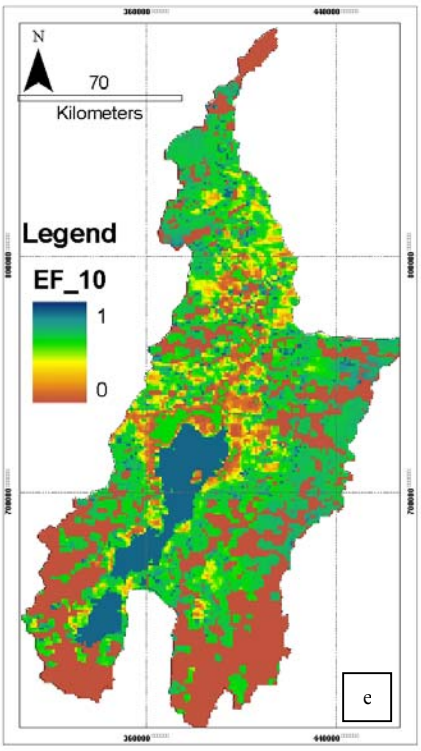
N
70
Kilometers
Legend
EF_10
1
0
e

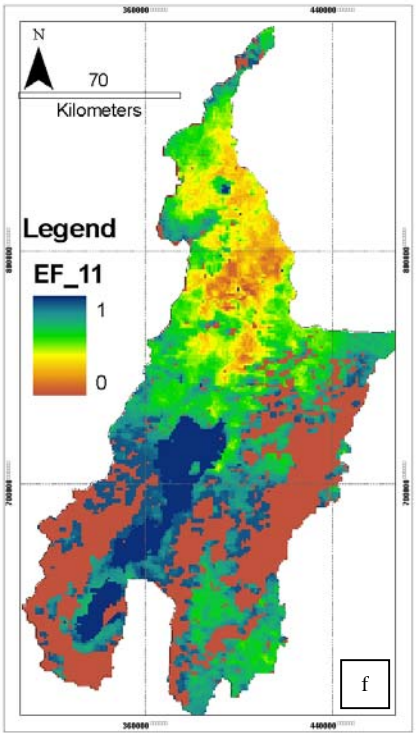
N
70
Kilometers
Legend
EF_11
1
0
f

Appendix 6.1. Potential evapotranspiration estimation.

Modified Penman or combination Method

Combination or modified Penman formula (MAFF, 1967) is used to compute reference/potential evapotranspiration from metrological data such as temperature, sunshine hour, wind speed and relative humidity obtained from five class I metrological station in the area. The method explicitly incorporates both physiological and aerodynamic parameters. The basic equation is:

$$PET = \frac{(\Delta/\gamma)H_T + E_{at}}{(\Delta/\gamma)+1}$$

Where PET = Potential Evapotranspiration, $\Delta =$ the slope of the curve of saturated vapor pressure plotted against temperature, $\gamma =$ hygrometric constant (0.27mmHg/^{0}F) and H_T is available heat which is expressed as:

$$H_T = R_I(1-r) - R_0$$

R_I and R_0 are incoming and out going radiation, respectively determined from sunshine hour, temperature and humidity.

R_I (1-r) = 0.78R_a*f_a (n/N) where f_a (n/N) = 0.16 + 0.62n/N and R_a = the solar radiation (fixed by latitude and season)

$R_0 = \sigma Ta^4$ (0.47 - 0.075$\sqrt{e_d}$(0.17 + 0.83n/N) where σTa^4 is the theoretical black body radiation at T_a and e_a = the saturated vapor pressure at air temperature, T_a.

E_{at} is rate of evapotranspiration which is given by:

$$E_{at} = 0.35\left(0.5 + u_2/100\right)(e_a - e_d)$$

Where u_2 is wind speed, e_a = the saturated vapor pressure at air temperature, T_a and e_a - e_d = the saturation deficit. The mean monthly temperature, sunshine hour record, relative humidity and wind speed were first interpolated to raster maps and PET was estimated using the above equations.

Appendix 6.2. Soil available water capacity in the study area.

name	lulc_class	rooting_de	Av_wat_cap	Av_wt_cap_
Luvisols	Agriculture	0.50	150.00	200.00
Vertisols	Agriculture	0.20	150.00	200.00
Leptosols	Agriculture	0.75	75.00	75.00
Fluvisols	Agriculture	1.00	200.00	200.00
Nitosols	Agriculture	1.00	200.00	200.00
Alisols	Agriculture and Forest	0.75	75.00	75.00
Luvisols	Agriculture and Forest	0.50	150.00	200.00
Leptosols	Agriculture and Forest	0.75	75.00	75.00
Luvisols	Agriculture and Forest	0.50	150.00	200.00
Nitosols	Agriculture and Grassland	1.00	200.00	200.00
Vertisols	Agriculture and Grassland	0.50	150.00	200.00
Andosols	Agriculture and Grassland	0.75	75.00	75.00
Vertisols	Agriculture and Grassland	0.50	150.00	200.00
Fluvisols	Agriculture and Swamp vegetation	1.00	200.00	200.00
Vertisols	Agriculture, Grassland and Woodland	0.50	150.00	200.00
Phaeozems	Agriculture, Grassland and Woodland	0.75	75.00	75.00
Leptosols	Bushland	1.00	100.00	100.00
Luvisols	Bushland agriculture	0.67	200.00	200.00
Nitosols	Bushland and Agriculture	1.25	250.00	250.00
Leptosols	Bushland and Bareland	1.00	100.00	100.00
Vertisols	Bushland and Grassland	0.67	200.00	200.00
Luvisols	Bushland and Grassland	0.67	200.00	200.00
Fluvisols	Bushland and Grassland	1.25	250.00	250.00
Luvisols	Bushland and Grassland	0.67	200.00	200.00
Nitosols	Bushland and Grassland	1.25	250.00	250.00
Leptosols	Bushland and Grassland	1.00	100.00	100.00
Andosols	Bushland dense	1.00	100.00	100.00
Leptosols	Bushland, Agriculture and Grassland	1.00	100.00	100.00
Vertisols	Bushland, Agriculture and Grassland	0.67	200.00	200.00
Leptosols	Bushland, Agriculture and Grassland	1.00	100.00	100.00
Luvisols	Forest and agriculture	1.17	350.00	350.00
Vertisols	Grassland	0.67	200.00	200.00
Fluvisols	Grassland	0.67	200.00	200.00
Vertisols	Grassland and Swamp vegetation	0.67	200.00	200.00
Leptosols	Grassland and Woodland	1.00	100.00	100.00
Vertisols	Grassland and Woodland	0.67	200.00	200.00
Luvisols	Swamp vegetation	0.67	200.00	200.00